ISBN 978-82-326-3984-7 (printed ver.)
ISBN 978-82-326-3985-4 (electronic ver.)
ISSN 1503-8181

Doctoral theses at NTNU, 2019:194

Erlend Løklingholm Engevik

Design and Operation Investigations for Large Converter-Fed Synchronous Machines in Hydropower Applications

Erlend Løklingholm Engevik

Doctoral thesis

Doctoral theses at NTNU, 2019:194

NTNU
Norwegian University of Science and Technology
Thesis for the Degree of
Philosophiae Doctor
Faculty of Information Technology and Electrical Engineering
Department of Electric Power Engineering

NTNU
Norwegian University of Science and Technology

NTNU
Norwegian University of Science and Technology

Erlend Løklingholm Engevik

Design and Operation Investigations for Large Converter-Fed Synchronous Machines in Hydropower Applications

Thesis for the Degree of Philosophiae Doctor

Trondheim, June 2019

Norwegian University of Science and Technology
Faculty of Information Technology and Electrical Engineering
Department of Electric Power Engineering

NTNU
Norwegian University of
Science and Technology

NTNU
Norwegian University of Science and Technology

Thesis for the Degree of Philosophiae Doctor

Faculty of Information Technology and Electrical Engineering
Department of Electric Power Engineering

ISBN 978-82-326-3984-7 (printed ver.)
ISBN 978-82-326-3985-4 (electronic ver.)
ISSN 1503-8181

Doctoral theses at NTNU, 2019:194

Printed by NTNU Grafisk senter

Acknowledgements

The research presented in this PhD thesis has been supported by the Norwegian Hydropower Centre (NVKS) and the Norwegian Research Centre for Hydropower Technology (HydroCen).

I would like to thank my supervisor, Professor Arne Nysveen, for his guidance, support and encouragement throughout this PhD project. I really could not have asked for a better supervisor. Thank you Arne!

Thank you to my co-supervisor, Professor Robert Nilssen, for your support. I appreciate all the interesting discussions and conversations that we have had on a wide range of topics.

Thank you to Professor Urban Lundin at Uppsala University. I am so grateful that I was allowed to come visit and perform the experimental work for my thesis. I would also like to thank PhD Candidate Fredrik Evestedt at Uppsala University for helping me prepare the experimental work I conducted in Uppsala.

Thank you to Mostafa Valavi and Astrid Røkke for being helpful and supportive. Your input and our discussions helped improve the quality of this thesis. I would also like to thank Trond Toftevaag. I have learnt a great deal about electrical machines and on teaching students during the time I have spent working for you as an assistant.

I wish to thank all my colleagues at the Department of Electric Power Engineering, and my friends and my family for your support throughout the four years that I have worked on this PhD project. Thank you for being there for the good times, the great times, the okay times and the challenging times. Your support helped me to finish this PhD thesis, and for that I am grateful.

Erlend L. Engevik, Trondheim 2019

Abstract

The work presented in this thesis deals with design and operation investigations for large converter-fed synchronous machines in hydropower applications.

It is shown that the optimal rated frequency that gives the lowest total cost is reached between 40 Hz and 50 Hz. Increasing the value of the synchronous reactance from 1.2 p.u. to 2.0 p.u. reduces the total cost of the generator.

The reduction in cost can help offset parts of the cost of the converter that are associated with having a converter-fed synchronous hydrogenerator in pumped-storage plants. This, in turn, can make variable-speed pumped storage plants more cost-competitive versus traditional fixed-speed solutions.

The effect of converter operation on AC copper loss in large hydrogenerators is investigated. Current harmonics produced by the converters increase the AC copper losses in traditionally designed stator windings. These additional losses could cause intolerable heating and probably destroy the windings.

If a generator is going to be built for converter operation using a two-level or a three-level topology, it is found that the strand thickness would have to be reduced. If this is not possible, a filter between the converter and the generator must be used.

Including damperbars in a converter-fed synchronous hydropower generator increases the AC copper losses in the stator. In addition to this, the losses in the damperbars themselves increase substantially. It is advised against using damperbars, if possible, when two- or three-level converter topologies are used.

Experimental work is been presented for a generator test setup. Losses have been measured at different levels of magnetization and at different rotational speeds. Mechanical losses and core losses are estimated from measurements. Experimental results have been used to verify the loss calculations used in this thesis.

Contents

List of Symbols

β	Stator winding short pitch ratio	
δ_{0e}	Equivalent airgap length	(m)
δ_0	Airgap length	(m)
δ_{max}	Maximum airgap length	(m)
γ_{cu}	Copper mass density	(kg/m^3)
γ_{Fe}	Iron mass density	(kg/m^3)
$\mathbf{R}$	Residual nonlinearity	
μ_0	Permeability of free space	$4 \cdot \pi \cdot 10^{-7}$ (H/m)
ν	Harmonic number	
ν_f	Fixed-point coefficient	
ω	Rotational speed	(rad/s)
ρ	Conductor resistivity	
σ	Material conductivity	
σ_c	Conductor conductivity	
τ_p	Pole pitch	(m)
τ_r	Damperbar slot pitch	(m)
τ_u	Stator slot pitch	(m)

MMF	Magnetomotive force	(ampere-turns)
ξ	Reduced conductor height	
A	Armature loading	(A/cm)
a	Number of parallel circuits	
A_f	Cross section of one field winding turn	(m^2)
A_p	Pole surface area	(m^2)
A_B	Damperbar cross section	(m^2)
$A_{cu,s}$	Stator winding copper cross section	(m^2)
b_D	Damperbar slot opening	(m)
b_t	Width of stator tooth	(mm)
b_u	Width of stator slot	(mm)
B_δ	Peak airgap flux density	(T)
b_{c0}	Width of copper strand	(mm)
b_{cuf}	Width of field winding	(m)
B_d	Stator tooth flux density	(T)
B_m	Peak magnetic flux density	(T)
b_{pc}	Width of pole core	(m)
B_r	Radial flux density	(T)
b_{sh}	Damper winding slot opening	(m)
B_t	Tangential flux density	(T)
B_{yr}	Flux density in the rotor ring	(T)
B_{ys}	Flux density in stator yoke	(T)
C	Output coefficient	
C_B	Ratio of damperbar resistivity to the resisitivity of copper	
C_{cons}	Cost of constant losses	(€/kW)

C_{cu}	Cost of copper	(€/kg)
C_{lam}	Cost of stator iron	(€/kg)
C_{ld}	Cost of load dependent losses	(€/kW)
C_{steel}	Cost of rotor iron	(€/kg)
C_{tot}	Total cost	(€)
D	Airgap diameter	(m)
d	Lamination thickness	(m)
D_o	Stator outer diameter	(m)
d_B	Damperbar diameter	(m)
f	Frequency of harmonic	(Hz)
f_0	Frequency used to obtain loss data	(Hz)
F_a	MMF of the armature winding	(ampere-turns)
F_2	Second order radial force density component	(N/m^2)
F_δ	MMF over the airgap	(ampere-turns)
F_{mp}	MMF over the pole core	(ampere-turns)
F_{mry}	MMF over the rotor ring	(ampere-turns)
F_{msy}	MMF over the stator yoke	(ampere-turns)
F_{mtot}	Total MMF, no-load	(ampere-turns)
F_{mt}	MMF over stator teeth	(ampere-turns)
f_{PWM}	Carrier frequency	(Hz)
f_{rr}	Radial force density produced by radial flux density	(N/m^2)
f_{rt}	Radial force density produced by tangential flux density	(N/m^2)
f_r	Radial force density	(N/m^2)
f_s	Synchronous frequency	(Hz)
GD^2	Flywheel effect	(tm^2)

H	Inertia constant	(s)
H_p	Magnetic field intensity in the pole core	(A/m)
H_t	Magnetic field intensity in the stator tooth	(A/m)
h_t	Height of stator tooth	(m)
H_y	Magnetic field intensity in the stator yoke or rotor ring	(A/m)
h_{c0}	Stator strand thickness	(mm)
h_{cuf}	Height of field winding turn	(mm)
h_{cus}	Height of Roebel bar strand	(mm)
H_{irr}	Irreversible component of hysteresis loop	(A/m)
h_{pc}	Height of pole core	(m)
h_{ps}	Height of pole shoe	(m)
h_s	Height of stator slot	(m)
h_{yr}	Thickness of rotor ring	(m)
h_{ys}	Stator yoke thickness	(m)
I_c	Stator bar current	(A)
I_f	Field current	(A)
I_s	Stator phase current, rms	(A)
k_1	Stator yoke loss correction factor	
k_2	Stator teeth loss correction factor	
k_{Cr}	Carter's coefficient due to slotting in the pole shoes	
k_{Cs}	Carter's coefficient due to stator slotting	
k_c	Eddy current loss coefficient	
k_C	Carter's coefficient	
k_{d1}	Airgap reduction coefficient due to the salient pole shape	
k_d	Winding distribution factor	

k_e	Excess loss coefficient	
k_{Fe}	The stacking factor of the iron core	
k_h	Hysteresis loss coefficient	
k_p	Winding pitching factor	
$k_{R,u/l}$	AC resistance factor, upper (u) and lower (l) layer	
k_v	Coefficient for the calculation of mechanical losses	
k_w	Total winding factor	
L	Axial length	(m)
L_δ	Airgap leakage inductance	(H)
L_ϕ	Copper length of one phase winding	(m)
L_σ	Total leakage inductance	(H)
L_{av}	Average winding length	(m)
L_{av}	Mean length of stator winding	(m)
L_B	Length of each damperbar	(m)
L_d	Tooth tip leakage inductance	(H)
L_{ew}	End-winding length	(m)
L_{fmd}	Mean length of field winding	(m)
L_{Load}	Load inductance	(H)
L_n	Iron length when ventilation ducts are excluded	(m)
L_{sq}	Leakage inductance due to skewing	(H)
L_u	Stator slot leakage inductance	(H)
L_w	End-winding leakage inductance	(H)
m	Number of phases in the stator winding	
m_{cu}	Weight of copper	(kg)
m_{iron}	Weight of iron	(kg)

m_{ts}	Weight of the stator teeth	(kg)
m_{ys}	Weight of the stator yoke	(kg)
n	Rotational speed	(rpm)
n_f	Number of turns per pole	
N_p	Number of poles	
n_R	Runaway speed	(rpm)
n_s	Rated, synchronous speed	(rpm)
N_B	Number of damperbars per pole	
n_{str}	Number of strands per stator slot	
n_v	Number of cooling ducts	
p	Number of pole pairs	
P_{10}	Specific iron loss at 1 T, 50 Hz	(W/kg)
P_{cons}	Constant losses	(kW)
$P_{cu,dc/ac}$	Stator copper loss, DC and AC	(kW)
P_c	Classic eddy current losses	(W)
P_e	Excess losses	(W)
P_h	Hysteresis losses	(W)
P_{input}	Input power	(kW)
P_{iron}	Iron losses	(kW)
P_{ld}	Load dependent losses	(kW)
P_{mech}	Mechanical losses	(kW)
P_{ps}	Pole surface losses	(kW)
P_{teeth}	Stator teeth losses	(kW)
P_{yoke}	Stator yoke losses	(kW)
q	Slots per pole and phase	

Q_s	Number of stator slots	
$R_{dc/ac}$	DC and AC resistance	(Ω)
R_{end}	Stator end-winding resistance	(Ω)
$R_{interbar}$	Resistance of end connection between two damperbars	(Ω)
$R_{interpole}$	Resistance of damper winding end connection between two poles	(Ω)
R_{Load}	Load resistance	(Ω)
R_{Phase}	Stator winding phase resistance	(Ω)
S_N	Rated apparent power	(kVA)
T	Torque	(Nm)
t_2	Damperbar pitch	(m)
T_M	Mechanical starting time	(s)
T_{ph}	Number of turns in series per phase	
T_p	Time period for the hysteresis loop	(s)
T_w	Time constant of the waterway	(s)
U_n	Stator line voltage, rms	(kV)
v_t	Rotor tip speed	(m/s)
W_w	Stator winding coil span	
X''_d	Subtransient reactance	(p.u.)
X'_d	Transient reactance	(p.u.)
X_{ad}	Armature reaction reactance	(p.u.)
X_d	Synchronous reactance	(p.u.)
X_l	Leakage reactance	(p.u.)
Z_b	Base impedance	(Ω)
z_a	Number of parallel strands	
z_t	Number of strands in one conductor	

Chapter 1

Introduction

This chapter presents the main motivation for introducing variable speed operation in hydropower applications with a focus on pumped storage plants. The impacts of variable speed operation on plant efficiency, the ability to control the active power in both turbine and pumping mode, and on reducing the wear and tear on the turbine runner, are discussed. The main variable speed technologies available today are discussed and the rationale for choosing the converter-fed synchronous machine option is presented.

1.1 Reasons for variable speed operation

The majority of hydropower plants in Norway were built in the period 1950-1980 [1]. In Sweden, most hydropower installations are from the 1950s and 60s [2]. Installed hydropower capacity in Sweden is 16.2 GW [2]. For Norway, the installed capacity is 30 GW [3]. Many of these plants have reached the age where they need to be upgraded and refurbished. New market requirements, new design philosophies and improved materials are forcing the owners of hydropower plants to reconsider the ways in which their installations are constructed.

The power system is experiencing that an increasing share of the electric power production is derived from intermittent power sources like wind and solar. Increased pressure is put on controllable power sources like hydropower to deal with fluctuations in the output of electric power. Fluctuations in the demand and supply of electric power in the grid require power plants that can be run with more flexibility in order to maintain balanced operation.

Most hydropower plants in operation today are installed with fixed-speed synchronous generators that are governed by a 50 Hz or 60 Hz grid frequency. The

speed of rotation is set by the optimal speed of the hydraulic machine. Hydropower plants with Francis turbines and reversible pump-turbines have a runner with fixed geometry [4]. Hydraulic efficiency is high at the design operating point, but drops when operation is changed from this point at fixed speed [4].

If the hydraulic machine is allowed to run at adjustable speed, the efficiency at part load can be increased [5]. Variable speed operation at part load is also beneficial for extending the lifetime of the turbine [6]. In pumping mode, adjustable speed operation leads to less cavitation, instabilities and vibration [4].

Flexible operation of hydropower plants with multiple starts and stops each day and operation outside the design best point has been shown to increase fatigue damage and reduce the lifetime of the turbine runner significantly [7].

Multiple starts, stops and operation at low load have been proven to be harmful for the runner [7]. Introducing variable speed operation is likely to reduce the number of starts and stops necessary per day and reduce the fatigue damage. Variable speed operation is also beneficial for reducing the tear on the runner in part load operation.

One of the main applications for adjustable speed generators is pumped storage hydropower plants. Such plants depend on the ability to change power production within short time periods. Pumped storage hydropower plants are the most important large-scale solution for balancing the supply and demand for power in the grid today.

Other applications where variable speed operation is applicable are large hydropower plants in remote areas that are coupled to the grid by a HVDC connection [8, 9]. Hydropower plants that experience a substantial variation in head during operation have, in addition, been shown to benefit from variable speed operation [10].

Variable speed operation can be used in a similar manner for run-of-river plants where the discharge shows large variations throughout the year in order to increase the overall efficiency. Using conventional, fixed-speed generators, several units are often installed to handle the variation in discharge, e.g. one large unit to handle rated conditions and one or several smaller units for production when the discharge is low.

By introducing variable speed operation, the number of units can be reduced since a larger discharge variation can be handled by one unit operating at variable speed. The main benefits of enabling variable speed operation can be summarized as:

- The ability to control active power in pumping mode
- Improved efficiency at part load
- Improved efficiency with large discharge variations
- Fewer units needed to handle large variations in discharge
- Improved efficiency with large variation in head
- Reduction in the number of starts and stops, yielding less runner fatigue damage

1.1.1 Improved power balancing

In turbine operation, the active power can be controlled by adjusting the opening of the guide vanes of the turbine. In pumping mode, it is not possible to control the active power during fixed-speed operation to the same extent due to the fixed geometry of the runner [4].

The pumping power is known to be proportional to the speed of rotation to the power of three [4]. This means that a machine that is designed to operate at $\pm$ 10% of the rated speed gives a power range of $\pm$ 25-30%. The ability to adjust the power of the machine by changing the speed of rotation makes it possible to achieve a greater balancing of power to fluctuating demand and supply situations in the grid [11].

Fig 1.1 presents the pumping mode operation of a pumped-storage plant with four units rated 100 MW each. The black curve indicates the need for balancing power in the system. Red represents fixed speed operation. During fixed speed operation, each unit can only pump 100 MW or nothing. It can be seen in Fig. 1.1 that the red area is not able to cover the need for balancing power most of the time. Several units have to be started and stopped several times, leading to a reduction in the lifetime of the plant.

It is decided to upgrade the power plant to enable variable speed operation where each unit is allowed to operate between 70 MW and 100 MW. The possible operation range is indicated in light blue. It can be seen that the ability to provide the required balancing power is substantially improved by introducing variable speed operation. With variable speed operation the pumped storage plant is able to pump most of the required balancing power in the system, as shown with the dark blue and red areas under the curve for balancing power in Fig. 1.1.

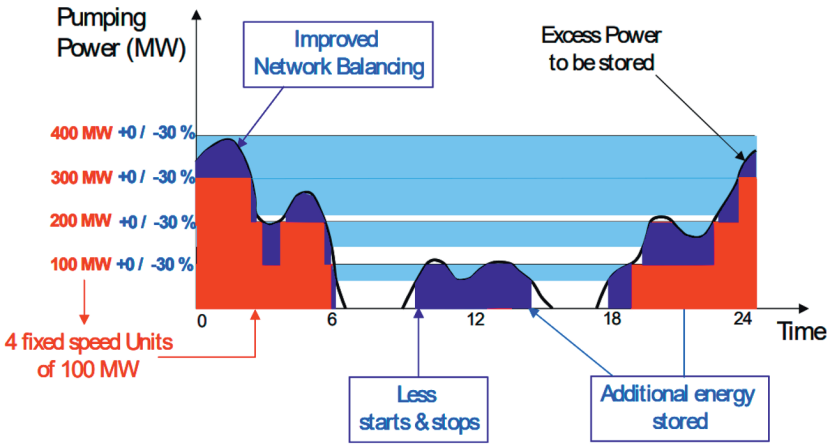

Figure 1.1: Improved balancing capability with variable speed operation [11].

1.1.2 Improved efficiency

The hydraulic efficiency of the runner can be increased by variable speed operation at operating conditions outside of the best point that the turbine is designed for. Figure 1.2 shows the efficiency curve hill diagram of a pump-turbine operating in turbine mode [4], where D_r is the runner diameter, H is the head and Q is the discharge. Initially the turbine is operated at its best point (b.e.p). Then the operational head is reduced to 60% of its initial value and the efficiency drops to 80% at point A. In order to increase the efficiency, the rotational speed is reduced to 88% of the rated speed, increasing the efficiency to 83%. By reducing the discharge the operator is able to increase the efficiency to 84% at operating point C. A further reduction in discharge allows the efficiency to increase to 86% at operating point D.

The efficiency curve for fixed speed operation is designed so that the efficiency is highest at the best point that the turbine is designed for. If the operation point is moved away from the best point, the efficiency drops. Fig. 1.3 shows the efficiency curve for a typical hydropower unit. The area shaded in blue is the efficiency range for fixed speed operation, while the area shaded in green is the efficiency range for variable speed operation.

It can be seen that the turbine efficiency is higher for variable speed operation than for fixed speed operation, but that the efficiency gain is smallest at the best point of rated power and head. It was shown in [8] that the hydraulic efficiency would be 3-10 percentage points higher for variable speed than for conventional operation.

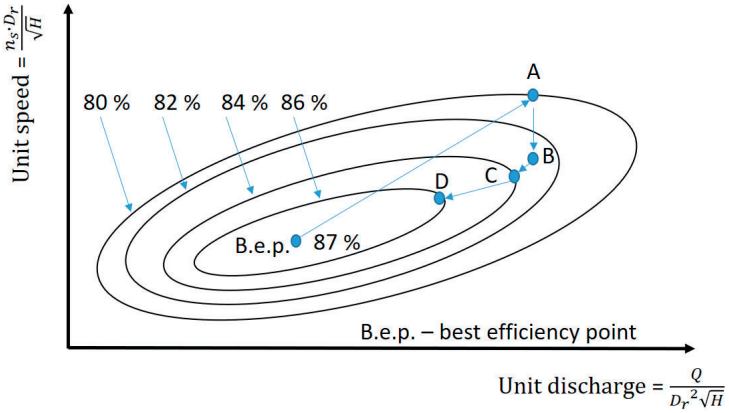

Figure 1.2: Turbine mode hill diagram for variable speed operation [4].

As can be seen from Fig. 1.3, the efficiency gain is largest at low power outputs and low head. There is some additional efficiency gain at operation above rated power and rated head, but the main benefits of variable speed operation are achieved at operation below the best point.

In addition to an increased turbine efficiency in part load, the efficiency of large synchronous machines operated with loads lower than the rated output power has been found to increase with variable speed operation [8]. At partial loading, down to 40% of rated power, the efficiency of the synchronous machine was found to increase by up to one percentage point.

1.2 Generator technologies for variable speed operation

There are two generator technologies that are available for flexible operation at variable speed, i.e. doubly-fed induction machines (DFIM) and converter-fed synchronous machines (CFSM). A schematic presentation of both the CFSM and the DFIM is given in Fig. 1.4.

It can be seen in 1.4 that the CFSM can be equipped with a bypass switch. This allows the generator to be synchronized to the grid in case of converter failure or in situations where the efficiency gain from converter operation is smaller than the power loss from the converter itself.

Using a DFIM in applications where variable speed operation is needed is the most mature solution. DFIMs are regularly used in wind power applications [13] and in pumped storage plants [14] with power ratings up to 400 MVA.

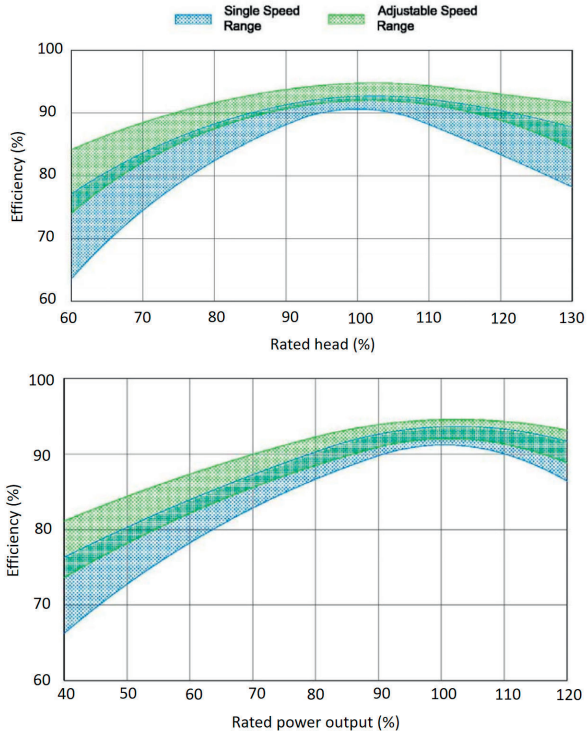

Figure 1.3: Turbine efficiency as function of rated head (top) and rated output for fixed and variable speed operation [12].

CFSMs are, in principle, ordinary synchronous machines that have the stator terminals connected to the grid via a frequency converter. Since the only connection between grid and machine is the converter, it must be able to transmit the rated active power of the synchronous machine. This means that the converter needs to be able to transfer 100% of the rated power of the synchronous machine.

DFIMs are constructed with the three-phase stator windings connected directly to the grid. The rotor is constructed as a three-phase wound rotor connected to the grid via a frequency converter [15]. Converter size depends on both the rated power of the machine and the selected speed range which governs the slip power [15]. It is possible to operate the DFIM as a motor and generator. Typical power ratings of the converter are up to 25% of the rated power of the DFIM.

1.2.1 Choice of generation technology

Until now, the choice of solution for variable speed power generation has been based on the cost of the power electronic converter and the available power rating

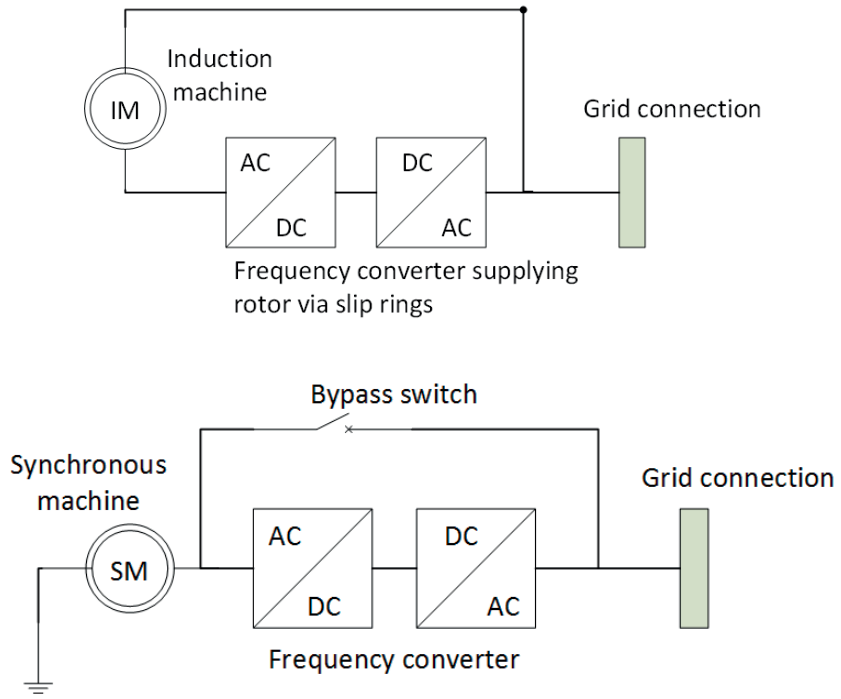

Figure 1.4: Schematic presentation of a doubly-fed induction machine (top) and converter-fed synchronous machine.

for this. Advances in the field of power electronics have steadily reduced the cost and increased the available rating of the converters.

The cost of the converter is one of the main reasons why DFIM solutions have been the preferred option for large variable speed pumped storage plants. Since the power rating of the converter that is needed for the DFIM is only a fraction of the power rating of the converter that is needed for the CFSM, a higher plant power rating is available for the same converter cost.

Globally there are 270 pumped storage plants operating or under construction with a combined, installed capacity of 12 000 MW [16]. 36 of these plants have variable speed operating capabilities. 17 are operational while 19 are under construction or planning. A list of pumped storage plants with variable speed capabilities, compiled from [17], are presented in Table 1.1.

It was claimed in [18] that the CFSM will be cost-competitive up to approximately 70 MW, see Fig. 1.5. For higher power ratings, the cost of the converter would

Table 1.1:
Pumped storage plants with variable speed capabilities [17]

Name	Country	Status	Year	Total capacity
Yagisawa	Japan	Operational	1965	240 MW
Okutataragi	Japan	Operational	1974	1932 MW
Le Cheylas	France	Operational	1979	500 MW
Grimsel 2	Switzerland	Operational	1981*	348 MW
Ohkawachi	Japan	Operational	1993	1280 MW
Kazunogawa	Japan	Operational	1999	1200 MW
Goldisthal	Germany	Operational	2003	1060 MW
Avce	Slovenia	Operational	2010	185 MW
Omarugawa	Japan	Operational	2011	1200 MW
Linth Limmern	Switzerland	Operational	2016	1000 MW
Frades II	Portugal	Operational	2017	780 MW
Nant de Drance	Switzerland	Under constr.	2019	900 MW
Swan Lake North	USA	Planned	2022	393 MW
Fengning 2nd phase	China	Under constr.	2025	1800 MW
Banks Lake	USA	Announced	2025	500 MW
Grimsel 3	Switzerland	Under constr.	2030	660 MW
Red John	United Kingdom	Announced		450 MW

*Variable speed technology installed later.

make the CFSM solution too expensive compared to installing a DFIM.

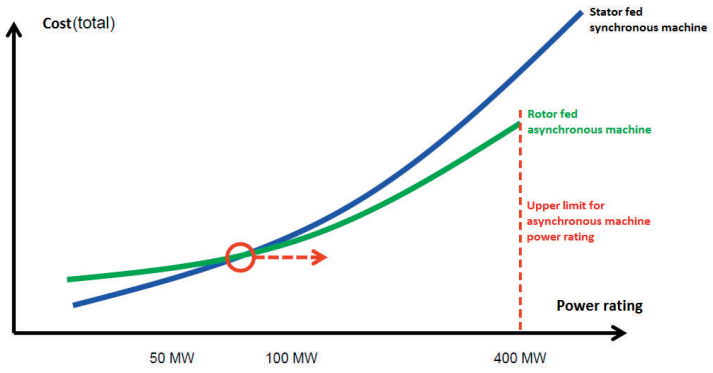

Figure 1.5: Cost comparison of doubly-fed induction machine and converter-fed synchronous machine [18]

Earlier converter-fed synchronous machine installations used a load-commutated inverter (LCI) that acts like a current source to control the generator. This converter topology consists of one converter that rectifies the line currents into a DC-current that is sent through an inductance. On the load-end of the LCI another converter is used to change the current into AC-current at a desired frequency [10].

LCI topologies have a harmonic distortion in the range of 3-10% [19]. This affects the electrical machine by inducing additional losses and oscillating airgap torques in the machine [10]. Machine-side harmonics have to be considered during the design of both the stator and the rotor [20].

In newer converter solutions based on the voltage source converter (VSC) topology, the line-side and load-side converters are separated by a DC-link capacitor instead of an inductance. The VSC acts like a voltage source instead of a current source. This leads to less harmonic distortion. As a result the issues related to the LCI topologies tend to be less severe in VSC topologies.

Recent developments have led to what is today the largest VSC with a rating of 100 MVA delivered by ABB to the Grimsel 2 power plant in Switzerland [21]. The full-rated 100 MVA converter was installed in order to transform one 90 MW fixed speed pumped-storage generator-motor into a variable speed solution. The main reason for this was to achieve better control of the active power both in turbine- and pumping mode. An alternative to installing the 100 MVA converter and connecting it to the existing synchronous machine, was to convert the existing generator into a doubly-fed induction machine.

It seems that the most aggressive lifetime reduction in the winding insulation due to converter operation is the accelerated aging of the stress relief coating in the end winding region, close to the mainwall insulation [22] .

The main ageing mechanisms for winding insulation are thermal and electrical. Which one of these will be the most salient for each generator, depends on several factors that are difficult to control. An insulation system that is rated for a higher voltage level is one option that can be used in order to avoid accelerated degradation of the winding insulation [22].

In high voltage insulation systems, the amplitude of the higher order voltage harmonics produced by the converter are small compared to the amplitude of the fundamental voltage harmonic component [22] . This reduces the risk of inter-turn insulation breakdown or weakening due to partial discharges.

The voltage components with higher frequencies could, in addition, cause higher dielectric losses and additional capacitive currents in the end winding region. These two loss components contribute to raise the winding insulation temperature, and produce local end winding insulation hotspots. These effects contribute to a reduction in the insulation lifetime.

The research on insulation materials in converter-fed hydropower generators with stator bars has not been brought to any conclusion. The joint European research program HydroFlex [23] has started working on these issues. One of the work packages of HydroFlex is dedicated to the topic of "Enhanced generator winding insulation system and performance testing" [23].

A solution for even higher power ratings has been proposed in [24]. The solution is based on the modular multi-level converter concept (MMC). Since the converter is based on modules, it is claimed that converters with power ratings from 50 MVA to 500 MVA can be constructed [24].

There are several drawbacks to using a DFIM instead of synchronous machines with a full-rated converter. The rotor is more complex, see Fig. 1.6, and design limits restrict the speed-variation of the DFIM [25]. It is claimed in [26] that the DFIM wound rotor is up to 30% heavier than a salient pole synchronous rotor. Fig. 1.7 illustrates the size difference between a synchronous machine and an induction machine with the same performance.

An additional argument for choosing a converter-fed synchronous machine instead of a DFIM for the project in Switzerland was that the starting procedure is more complicated for the DFIM than for the synchronous machine. It is also easier to comply with the grid code requirements by using a CFSM than it is when a DFIM solution is chosen [25].

The starting torque of the induction machine is limited by the maximum output voltage of the converter and the insulation of the rotor winding [28]. This requires

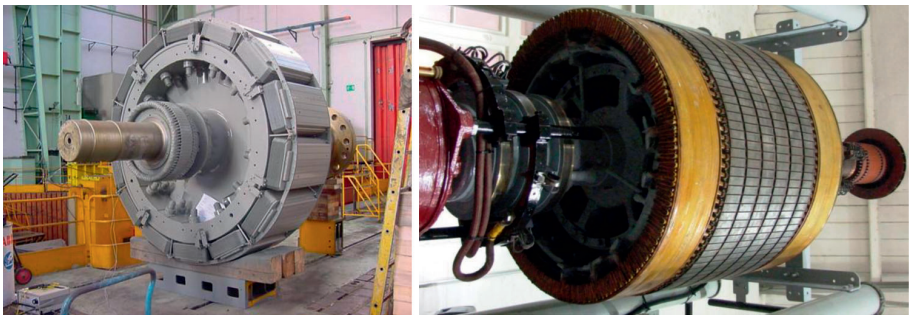

Figure 1.6: Example of rotor construction of synchronous machine (left) and induction machine. Not to scale [18].

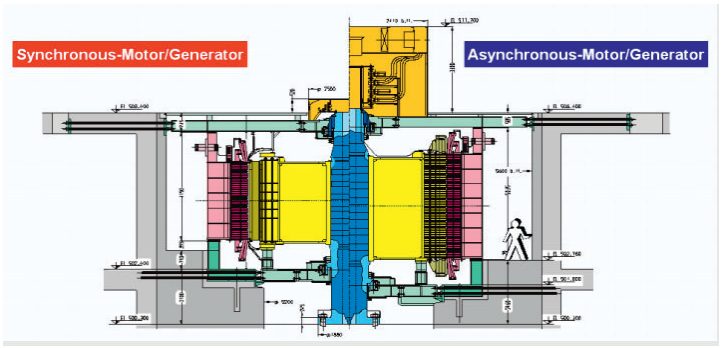

Figure 1.7: Visualization of the size difference between a synchronous machine (left) and an induction machine with the same rating [27].

the DFIM to be started at a flux weakening ratio as high as 1:8. The consequence of this on the starting of DFIMs, is that the starting torque is limited. This leads to time-consuming and costly pump-turbine blow-down before starting [24].

Active power transmitted through the rotor of the DFIM is often limited to between 15% and 25% of the rated power of the machine [24]. Having a rotor with a larger power capacity would require designs with a higher rotor voltage or a higher rotor current.

Rotor voltage is constrained by the maximum voltage level of the frequency converter [29]. A higher voltage level would require more insulation around the rotor winding. The rotor current is usually limited by the ability to cool the rotor. These are some of the reasons why DFSMs are only able to operate at a limited frequency range.

If a CFSM is used, starting is not considered an issue. The speed is controllable

from zero to rated speed, and the machine is able to produce substantial torque from zero speed [24]. As a consequence, the CFSM can start with the pump-turbine in water, saving time and allowing for faster changes from pump to turbine mode.

In the case that an MMC converter is used, however, the converter has limitations in producing torque at low speeds, where additional common mode voltage injection might be needed [24]. The capacitors in the converter buffer power fluctuations of the fundamental and second harmonic frequencies.

When the phase current frequency is reduced, e.g. operating at lower than rated speed, the capacitor voltage ripple magnitude is increased [30]. The voltage ripple becomes infinitely large at zero phase current frequency. Starting the machine from zero rotational speed and frequency is challenging when an MMC is used. If delivering a constant torque over the entire speed range is required, it will likely require a converter that is overrated at the rated operating point [30].

Another benefit of the CFSM solution is that only active power from the synchronous machine is transferred through the converter. This means that the synchronous machine does not need to be able to supply any reactive power to the grid. Consequently, the synchronous machine can be designed for rated operation at unity power factor [24]. This reduces the apparent power rating of the machine, making a smaller, less costly and more compact machine [31].

It has been shown that using a converter-fed synchronous machine instead of a doubly-fed induction machine has many benefits when variable speed operation is required. The main drawback is the cost of the converter which needs to be rated for the full power of the synchronous machine instead of only up to 25% of the power as is the case in the DFIM solution. The following is a list of the main benefits of choosing the CFSM solution:

- Easier and faster starting that does not require dewatering of the turbine
- Larger speed and power variations possible than with DFIM solutions
- The rotor of the DFIM is more complex and expensive

Based on this, the converter-fed synchronous machine topology is chosen for the analysis presented in this thesis.

1.3 Outline of the thesis

The structure of this thesis is given in Fig. 1.8. The main contents of each chapter are explained in brief below. The main body of the thesis is separated into two parallel paths. One focuses on design improvements for converter-fed synchronous hydropower generators, primarily using analytical methods. The other path investigates the effects of converter operation on the generator, focusing on finite element modeling and simulations.

Chapter 2 presents a review of literature related to the design and analysis of large synchronous hydrogenerators. Different research topics that do not appear to be sufficiently answered in the literature are presented.

Chapter 3 presents a framework for how to design and calculate the different parameters for a large hydropower generator. An analytical model is used as the basis for the design process, and an optimization approach that can be coupled with the analytical model is presented.

Chapter 4 presents experimental validation measurements and analysis of losses in hydropower generators. Different core loss models are compared.

Chapter 5 investigates the effect of converter operation on the losses in the generator.

Chapter 6 presents the analysis of low order radial forces in large hydropower generators with fractional slot windings. The influence of winding layout and airgap length on the lowest order radial force component is analyzed.

Chapter 7 deals with the questions of finding the optimal rated frequency at different rotational speeds and what the synchronous reactance value should be when the reactance requirement is relaxed.

Chapter 8 gives a summary of the thesis and presents the main conclusions of this work.

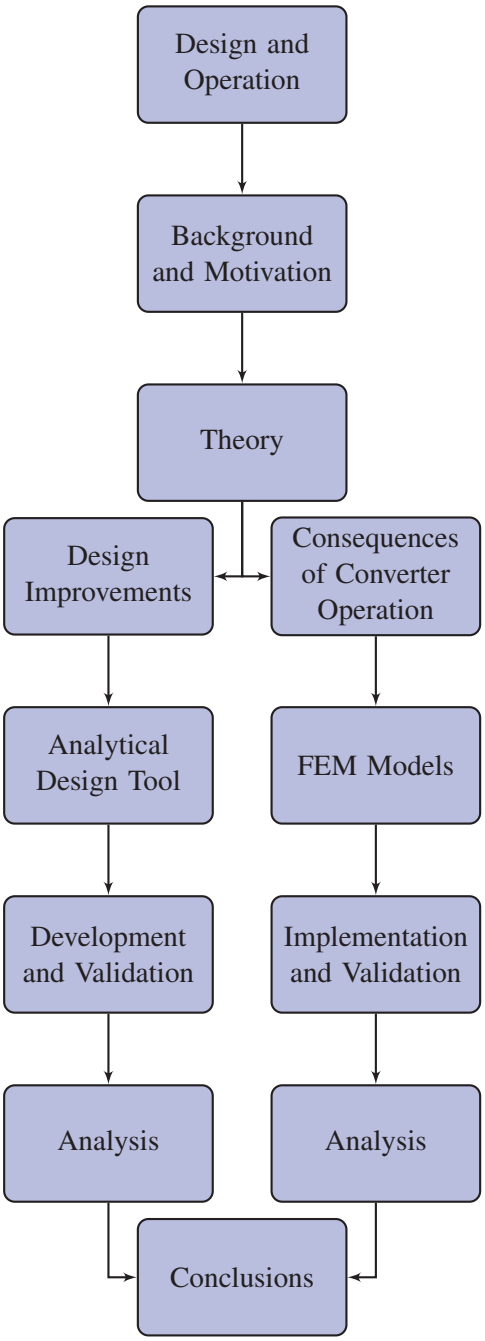

Figure 1.8: Structure of thesis

1.4 List of publications

Conference papers:

- E.L. Engevik, M. Valavi and A. Nysveen, '*Analysis of additional eddy-current copper losses in large converter-fed hydropower generators*', 2018 XXIII International Conference on Electrical Machines (ICEM), Alexandroupoli, Greece, Sep. 2018

  E.L. Engevik came up with the idea for this publication, performed the finite element simulations, and computed all the calculations needed to obtain the results. The conference article was written, including the presentation and discussion of the results, by E.L Engevik.

- E.L. Engevik, M. Valavi and A. Nysveen, '*Influence of winding layout and airgap length on radial forces in large synchronous hydrogenerators*', 2017 20th International Conference on Electrical Machines and Systems (ICEMS), Sydney, Australia, Aug. 2017, pp. 1-6

  E.L. Engevik performed the finite element simulations, and computed all the calculations needed to obtain the results. The conference article was written, including the presentation and discussion of the results, by E.L Engevik.

- E.L. Engevik, T.E. Hestengen, M. Valavi and A. Nysveen, '*Effects of lifting reactance requirements on the optimal design of converter-fed synchronous hydrogenerators*', 2017 IEEE International Electric Machines and Drives Conference (IEMDC), Miami, USA, May 2017, pp. 1-8

  E.L. Engevik performed the optimization for the different designs presented in this paper based on the optimization routine implemented by T.E. Hestengen. All results were computed, analyzed and presented by E.L. Engevik. The paper was written, including the presentation and discussion of the results, by E.L. Engevik.

- E.L. Engevik, M. Valavi and A. Nysveen, '*Efficiency and loss calculations in design of converter-fed synchronous hydrogenerators*', 2016 XXII International Conference on Electrical Machines (ICEM), Lausanne, Switzerland, Sep. 2016, pp. 1636-1642

  E.L. Engevik came up with the idea for this publication, and performed all the calculations for this publication. All results have been analyzed, presented, and discussed by E.L. Engevik. This conference article was, in addition, written by E.L. Engevik.

Conference papers not directly related to the main content of the thesis:

- E.L. Engevik, A. Røkke and R. Nilssen,'*Evaluating Hybrid Optimization Algorithms for Design of a Permanent Magnet Generator*', ACEMP-OPTIM-Electromotion Joint International Conference 2015, Side, Turkey, Sep. 2015, pp. 711-718

1.5 Scientific contributions

The main scientific contributions presented in this thesis are listed in the following:

- Chapter 7: The effect of the choice of rated frequency on the total cost of the generator is investigated. The optimal rated frequency that gives the lowest total cost is reached between 40 Hz and 50 Hz. It is shown that the weight of the generator is reduced when the rated frequency is increased. A higher rated frequency gives a lighter generator with a lower cost for the active materials. The losses in the machine increase when the rated frequency increase, which leads to an increase in the cost of losses.
- Chapter 7: The effect of relaxing the synchronous reactance requirement on the total cost of the generator is investigated. It is concluded that the total cost of the generator is reduced when the value of the synchronous reactance is increased. Increasing the value of the synchronous reactance from 1.2 p.u. to 2.0 p.u. reduces the total cost of the generator.
- Chapter 6: The lowest mode of vibration of three large generators is studied. For all the generators investigated, i.e. a 114-slot/14-pole generator, a 180-slot/14-pole generator and a 432-slot/70-pole generator, the lowest mode of vibration is the second spatial harmonic. It is found that the lowest mode of vibration is primarily produced by the main flux density harmonic component and its adjacent harmonic components.
- Chapter 6: An increase in the synchronous reactance gives a shorter airgap length. This can lead to vibration problems caused by low order radial forces in the airgap. It is found that reducing the airgap leads to a less than proportional increase in the lowest order radial force component. The reason for this is that the reduction in airgap length is causing increased saturation in the generator.
- Chapter 6: It is found that damperbars are able to reduce the lowest order radial force component by 20-40% compared to the case without damperbars. The damperbars are able to reduce the lowest order force component

more efficiently when the airgap length is reduced. The downside of this is that the losses in the damperbars themselves are increased when the airgap length is reduced.

- Chapter 6: It is shown how the amplitude of the largest flux density harmonic adjacent to the main harmonic can be significantly reduced by careful rearrangement of the winding configuration. In cases where low order radial forces cause vibration problems, the problem can be reduced considerably by rearranging the winding configuration. It is demonstrated that the lowest order radial force component can be reduced by more than 60% by rearranging the winding layout.

- Chapter 5: Converter operation is found to increase the stator winding AC copper losses. These additional losses could cause excessive heating and potentially destroy the windings. The results show that a higher carrier frequency leads to an increase in the AC copper losses in the stator winding. Using a three-level converter topology instead of a two-level topology offers significant reductions in the AC copper losses.

- Chapter 5: It is found possible to reduce the AC stator copper losses during converter operation by reducing the strand thickness in the stator winding. When a two-level or a three-level converter is used, it is necessary to reduce the strand thickness compared to traditional designs.

- Chapter 5: It is advised against including damperbars in a converter-fed synchronous hydropower generator. Damperbars lead to an increase in the AC copper losses in the stator. In addition, the losses in the damperbars themselves increase substantially with converter operation. If damperbars are required, a filter between the generator and the converter must be installed.

- Chapter 5: The effect of converter operation on the iron losses is investigated. The results show that an increase in the iron core loss in the range of 10-30% can be expected using traditional two- and three-level converter topologies. The additional losses are smaller for the three-level topology than for the two-level converter. Using a higher carrier frequency reduces the additional core losses.

- Chapter 4: Experimental work is presented for a generator test setup at no-load and with load. Losses are measured at different levels of magnetization and at different rotational speeds. Mechanical losses and core losses are estimated from measurements. Experimental results are used to verify the loss calculations used in this thesis.

- Chapter 4: Stator core losses are predicted using the Bertotti method and the Vector-Preisach model for two hydropower generators, in addition to the generator test setup. The Bertotti method gives a core loss prediction that is close to the reference value for both the large generators, and to the measured losses in the generator test setup. Accurate core loss estimates are achieved with the Bertotti method for different power ratings and design types.

- Chapter 4: The usefulness of the Vector-Preisach model for calculating the hysteresis losses in the iron core of large hydropower generators is investigated. Using the Vector-Preisach model is not found to improve the core loss prediction significantly. The model is found to be more sensitive to saturation than the Bertotti method.

- Chapter 4: Different correction factors for the stator core losses are applied in order to discover which values should be used optimally. The Bertotti method is shown to give more consistent core loss predictions using correction factors than the Vector-Preisach model. It is not conclusive which correction factor gives the best loss prediction, it must be decided on a case-by-case basis.

Chapter 2

Literature review

This chapter presents a review of available literature related to the design and analysis of synchronous hydrogenerators. The topics covered will deal with the optimal design of hydrogenerators, along with the use of finite element simulations in the analysis of hydrogenerators, losses and radial forces. The section on losses covers different core loss models, the analysis of eddy current copper losses, and additional losses due to harmonics produced by converter operation. The analysis of low order radial forces in large generators with fractional-slot windings is also covered. Finally, different research topics that do not appear to be sufficiently answered in the literature are presented.

2.1 Optimal design of hydrogenerators

Optimization algorithms have been used to aid the design of electrical machines for decades. The optimization of electrical machine design is a nonlinear problem with both nonlinear constraints and integer variables. There is a long list of optimization methods, including algorithms that are linear and nonlinear, direct and indirect, with constraints, deterministic, stochastic, and evolutionary, that have been used [32].

Stochastic optimization methods have been used to find the optimal design of large synchronous machines since the late 1960s. In [33, 34], a Monte Carlo simulation approach was used to optimize the design of a large hydrogenerator. More advanced, stochastic methods such as Genetic Algorithms and Particle Swarm Optimization have been used to find the optimal design for large synchronous machines [35].

Traditionally, the number of poles in a hydrogenerator is given by the rotational

speed that is optimal for the turbine of the particular generator. With a converter-fed synchronous hydrogenerator, the number of poles in the generator can be set more freely.

In [36], a parametric sweep was used to investigate the influence of the combination of the pole number and the outer diameter on the optimal design. It was found that for each diameter there is a pole number that minimizes the total cost. For large diameters the optimal pole number was higher than for smaller diameters. Larger diameters in hydrogenerators are usually associated with lower rotational speeds.

Increasing the number of poles increases the output frequency. For radial flux machines the thickness of the stator yoke is proportional to the pole pitch [31]. When yoke thickness is varied as a function of pole pitch, the flux density in the yoke is kept constant and the weight of the machine is reduced. Significant weight reductions can be achieved by increasing the pole number [36].

It is well known that losses increase with frequency. When designing a hydrogenerator, there is a trade-off between keeping the weight of the generator low and keeping the efficiency high. In order to decide what the optimal nominal frequency should be, it would be necessary to perform an optimization where, among other factors, both the weight of active materials and losses are minimized simultaneously. One effective approach to finding the optimal trade-off between these competing objectives is to minimize the total cost of materials and energy losses simultaneously [37].

There are many constraints that the designer must take into account if he or she wants to find the optimal design. There are mechanical limitations, thermal limitations, material limitations and limitations due to grid requirements that all constrains the possible solution space where the optimal design is to be found.

Today, hydrogenerators are designed to be directly grid-connected. They are constrained by the existing grid codes at the sites where they are installed. One of the limiting design constraints given by these grid codes is the stability demand that directly affects the permitted value of the synchronous reactance.

In cases where a converter-fed synchronous hydrogenerator is used, the generator is not synchronously connected to the grid. It is therefore not restricted by the same stability requirements, unless they are supposed to be able to be directly grid-connected in certain situations. Therefore, the requirement on the value of the synchronous reactance may be relaxed in order to reduce the total cost. Subject to synchronous reactance constraints, the length of the airgap is dimensioned to optimize the efficiency by minimizing the magnetizing current [38].

The primary limiting parameter for the synchronous reactance is the airgap length. A low maximum value for the synchronous reactance requires a longer airgap and more ampere-turns in the field winding for the same apparent power [39]. This leads to a higher field current, greater field winding losses, tougher cooling requirements and lower generator efficiency [40]. By relaxing the upper limit for the synchronous reactance, the airgap length is allowed to be reduced.

A negative effect of a reduction in the airgap length is that the pole surface losses increase due to a larger slot width to airgap ratio. In order to keep heating caused by pole surface losses low, the airgap should be kept sufficiently large to keep a moderate slot width to airgap ratio [41].

Unanswered research questions

For converter-fed synchronous hydrogenerators the stability and frequency requirements are no longer governed by the grid operator as the generator is no longer synchronously connected to the grid. The following are two key research questions that arise with the introduction of converter operation of hydropower generators:

- What is the optimal choice of rated frequency for a converter-fed hydropower generator?
- What is the effect of relaxing the requirement on the synchronous reactance on the optimal design of the generator?

2.2 Finite element simulations

Finite element simulations are often used to analyze large hydrogenerators where analytical methods might not be sufficiently accurate. In particular, the induced stator voltage waveform, the value of the different reactances, and losses are normally calculated using finite element simulations. A substantial number of publications deal with aspects related to losses, forces and the distribution of the magnetic field in the generator.

A more detailed review of the use of finite element simulation of losses and radial forces in large hydropower generators is provided in Section 2.3 and Section 2.4 respectively.

2.3 Losses

Copper loss

Converter operation of large hydrogenerators brings additional current and voltage harmonics that may cause problems with excessive losses and vibration [42]. In

copper windings there are both resistive losses due to the DC resistance of the winding cross section and additional AC losses due to skin and proximity effects, also known as eddy current losses. When the penetration depth of the winding cross section becomes significantly larger than the diameter of the strand at the given harmonic frequency, it causes the current to flow along the outer part of the conductor and cause excessive losses.

The eddy current loss in windings increases with the high-frequency harmonics that are produced in converter operation [43]. Several papers have investigated the effect of converter harmonics on the eddy current losses in stator windings of large induction motors in the MW range. In [44] the effect of converter operation on stator winding heating is studied.

The total copper losses in the winding consist of AC and DC losses. DC losses are caused by the equivalent DC resistance and the rms current in the winding. AC losses are the eddy current losses due to skin and proximity effects caused by the different harmonic components in the winding current. Additional AC losses due to converter operation denotes the additional eddy current losses caused by current harmonics that are not present in normal grid operation.

It can be seen in [45] that the AC copper loss during converter operation can be in the range of 40-198% of the DC copper loss. For large hydrogenerators, the heating of the stator winding is often the limiting factor in the design. For such machines, the AC copper loss can be in the range of 10-15% of the DC losses. For the generator presented in [38], the AC loss is as high as 30% of the DC loss.

There are studies presented for the converter operation of large synchronous machines in the power range of up to a few tens of MVA. Until recently two-level and three-level voltage source converters (VSC) have been used for supplying high-power electrical machines at the largest power ratings. These converters produce rich harmonic spectrums in terms of both voltage and current. Operating generators that have been designed for sinusoidal operation with a frequency converter may lead to excessive heating and damage.

No studies have been found that present the effect of converter operation on the stator winding losses of large hydrogenerators with power ratings above 100 MVA. Grimsel 2 is the largest pumped storage plant with a full-rated converter installed [25] at 100 MW. The Grimsel converter has a three-level topology with a filter installed in order to use the existing generator without excessive heating. It is therefore not presented in any analysis of the additional AC losses in Grimsel 2.

In [24] a modular multilevel converter (MMC) is proposed as the future solution for large converter-fed hydrogenerators. An MMC solution has been shown to

drastically reduce amplitude of the harmonic voltages and currents produced by the converter. This allows the use of traditional generator designs without filters. It is shown in [46] that the additional copper losses are relatively high when a two-level topology is used. For a multilevel topology these losses become negligible.

Many publications have been presented on the modeling and prediction of currents and losses in damper windings of large hydrogenerators. It is common practice to use fractional slot windings in large hydrogenerators. These windings produce subharmonics that interact with the damper winding to increase the damperbar losses during normal operation compared to integer slot windings [47].

In [48] an analytical method for calculating damperbar currents and losses is presented. The magnetic field in the airgap is predicted using a permeance model that is used as input for an equivalent circuit model. [49] uses permeance data from stationary finite element simulations together with a rotating field model to predict damperbar losses. Both methods are compared to finite element simulations.

A permeance model is used in [50] to compute the induced damperbar voltages using numerical integration. The results are compared to finite element simulations using an external circuit to represent the damper winding. The main reason for this is that damperbar currents are not normally measured during the comissioning of electrical machines [51]. There are only a few publications comparing simulations to measurements.

[52] modeled the damper winding in a 2D finite element simulation with a coupled external circuit model. The results are compared indirectly in [53] by temperature measurements on the damperbars and a thermal model where the simulated damperbar losses are used as input. The results from direct measurements of damperbar currents in a large hydrogenerator were presented in [54]. The results from [54] were analyzed and compared to simulations in [55].

The same voltage and current harmonics that are produced by converter operation induce additional losses in damperbars. A large synchronous motor with salient poles has been analyzed with sinusoidal and converter-fed operation in [56]. It was found that damperbar losses can increase dramatically with converter operation. For converters in the MW range it is normal to use a low carrier frequency, e.g. 250-450 Hz [57]. It is shown in [57] that additional losses due to converter operation in this machine are greatly reduced when a three-level topology is used instead of a two-level topology. When a multilevel converter is used, the additional losses become small.

Unanswered research questions

Converter operation is most likely going to produce additional losses in the windings of large hydropower generators. Based on what has been reported in the literature for large converter-fed synchronous motors, the following research questions remain unanswered:

- What is the effect of converter operation on the AC losses in the stator and damper windings?
- What can be done to mitigate the possibly adverse effects of converter-operation on the losses in the stator and damper windings?

Core loss

The method of loss separation presented by Bertotti [58] where iron losses are divided into hysteresis- eddy current- and excess losses, has been popular for estimating core losses in electrical machines. There are other, more detailed, models that describe hysteresis behavior mathematically.

Current models for iron loss estimation are often complex, and require detailed material data, measurement data and computational resources [59]. Many of the modern core loss estimation methods are based on more detailed modeling of mathematical hysteresis [60]. These models include the loss surface model, viscosity based magnetodynamic models, and friction like hysteresis models [60].

Examples of the recent core loss models are [59] and [61]. [59] uses measured loss and hysteresis loop data to calculate the instantaneous core losses. Core losses are calculated as a function of flux density and the flux density rate of change, $\frac{dB}{dt}$. The approach presented in [61] uses a generalized dynamic hysteresis model paired with measured hysteresis loop data to include the effects of complex waveforms on the iron core losses.

It is worth noting that these, more recent, core loss models are reported applied on smaller, low power machines. Smaller electrical machines have different iron loss distribution and saturation patterns than synchronous hydropower generators.

The results presented in [62] show that accurate results can be achieved using loss models based on the Bertotti approach. This approach has been shown to be able to provide accurate results for similar values of frequency and flux density to those used to obtain the loss coefficients in the model.

A large synchronous hydrogenerator was analyzed using finite element simulations where core losses were estimated using the Bertotti model in [63]. The iron loss

prediction was compared to loss measurements acquired using the no-load test. The simulated loss estimate was found to be in agreement with the measurements.

In [64] different loss models based on the traditional Steinmetz equation were found to give similar loss predictions for the same hydrogenerator. The core loss analysis for this generator was further extended in [38] to cover the influence of magnetic material, changes in excitation current and different airgap lengths. It was found that core losses could vary up to 25% based on the selected material data in the machine. It was also shown that it can be difficult to set the correct airgap length and excitation current in the simulations as the real data do not always correspond to the design data of the generator.

It is well known that simulated core loss is often smaller than the measured core losses in no-load. Seventy hydrogenerators were studied in [65]. The study found that, on average, the estimated yoke losses would have to be multiplied by 1.55 in order to correspond with the measured losses.

Similarly, based on simulations and measurements of the total core loss in 46 generators rated for 5-20 MVA, the measured losses were found to be 1.71 times higher than the predicted losses [66].

Additional losses not taken into account by core loss prediction methods causing the underestimation of core losses include rotational field effects [67], non-sinusoidal waveform, punching, stresses and burrs [68].

The effects of punching the lamination sheets into the right shape alter the magnetization properties of the laminations close to the cutting edges. This has been shown to increase the iron losses, typically by around 4%, but not more than 10%, for large hydrogenerators [69]. The increase in losses due to punching depends on the affected surface area relative to the total surface area.

The effects of manufacturing and assembly of the core laminations are difficult to accurately estimate. It would require thorough knowledge of the entire manufacturing and assembly process for each generator to achieve this.

There are few comprehensive studies available that focus on the typical situation occuring in stator cores of large hydrogenerators. In [70], data from 12 existing 50 Hz synchronous hydrogenerators ranging from 26 to 500 MVA are used to predict stator core losses from 2D finite element simulation. These predictions are compared to core losses measured at no-load. The results show that the methods consistently estimate from 50-70% of the no-load core loss in each generator.

A considerable amount of work has been put into modeling the additional core losses due to rotational fields. By modifying the core loss models used in [70] to

incorporate rotational losses, a better estimation of the core losses was achieved.

In [71] it was found that, in the hydrogenerator studied, over 60% of the stator had a rotating flux. It is shown in [72] that generators that are more saturated experience fields that are more rotational. This means that saturation will increase losses due both to higher levels of flux density and an increase in the rotational loss component. Design features that affect the distribution of rotational fields, and losses, are yoke thickness and airgap length.

It is found in [71] that machines with overdimensioned yokes and small airgaps experience more rotational flux and, as a consequence, more rotational losses. Reducing the thickness of the yoke seems to reduce the amount of rotational flux. If the yoke thickness becomes too thin, it is expected to lead to saturation that will increase the rotational losses.

In [70] several modifications to the existing methods were used to incorporate the effects of the rotational fields. First, the loss expressions were multiplied with expressions for the aspect ratio, i.e. the ratio between the maximum flux density amplitude of the minor axis component to the maximum amplitude of the major axis. In addition to this, the losses were multiplied by a correction factor estimating the difference between the value for rotational and alternating losses.

The factor for the aspect ratio is not that difficult to obtain. It is more challenging to correct for the difference in alternating and rotating losses. For the study in [70], due to lack of rotational loss data, typical values given in literature were used. Using these factors, the core loss estimation was improved from approximately 50% of measured losses up to around 70% of the measured losses. It is assumed that real loss data would help improve the loss prediction given by the model.

It has been seen that it is possible to improve the existing models to incorporate different effects like rotational losses. This requires a great deal of available material data that is often not provided by the manufacturers. It is possible to use parameter values and data given in literature that may fit to some materials and some cases. This, however, may not give significantly better loss predictions than the classical methods with correction factors that incorporate all these effects and that are based on empirical data from existing machines.

In order to overcome the problems related to traditional core loss methods like the Bertotti model, more detailed approaches to modeling hysteresis have been employed. These methods include scalar and vector versions of the Preisach hysteresis model, which attempts to describe the physical hysteresis process mathematically.

A Vector-Preisach model was used for 2D finite element analysis in [73] to compute core losses. The model was incorporated in the simulations using a fixed-point iteration technique. Core loss predictions were shown to agree with measured results under non-saturated conditions.

The loss property of the Vector-Preisach model can be sensitive to implementation [74], especially for circular magnetic fields and in saturation. A solution is proposed in [74] to correct the angle between the H-field and the B-field. This solution helped to remove the irreversible process that can persist at saturation.

Hysteresis loops can be accurately measured up to approximately 1.6 T. In finite element simulation programs it is required that the BH-curve is continuously approximated for flux densities up to and beyond 2 T. Inclusion of hysteresis can easily lead to divergence [75]. Bicubic spline algorithms were proposed in [75] as a solution to this issue, which seems suitable for improving the modeling of the hysteresis loop.

It was found that, for larger salient pole synchronous machines, the effect of using a single-value BH-curve instead of the full Preisach hysteresis model overestimated the losses by less than 2.5% in all operating points [76]. These results indicate that it is not necessarily guaranteed to achieve better results with more detailed core loss models.

Skin effect have a damping effect on the flux harmonics that induce eddy current losses in the laminations. In larger converter-fed machines with larger airgaps, the rotor core losses are typically smaller than the stator core losses [57]. It was found in [76] that excluding skin effect from the magnetic field solution has little impact on the total stator core losses in multi MW machines where the stator core losses are dominant.

Rotor core losses are dominated by eddy current losses induced by higher order flux harmonics [76]. In converter-fed machines where the rotor core losses are either large compared to the total stator and rotor core losses, or where rotor core losses are to be estimated accurately, the effect of skin effect cannot be neglected. Neglecting the skin effect in such cases can overestimate the losses with up to 20% [76].

Iron losses are known to increase in converter operation. It was shown in [46] that using a two-level converter increased the iron loss by 27%. Using a three-level converter reduced the additional iron loss to 6%. The amount of additional iron loss during converter operation is both dependent on converter topology and carrier frequency. For large synchronous machines, the increase in stator core losses with converter operation has been shown to be smaller than the increase in damperbar

loss when compared to sinusoidal operation [56].

For large machines, a typical carrier frequency is in the range of 250 Hz to 450 Hz. In [57] a two-level converter was found to increase the core losses by 42% using 250 as the carrier frequency. With a 450 Hz carrier frequency the additional core loss was 33%. Using a three-level converter topology reduced the additional core losses significantly. Adding even more voltage levels by using a five-level topology made the additional losses insignificant [57].

In addition to core losses in the stator and pole shoe and damper bar losses, there are core losses in the end region of the generator. These losses can be separated into end-stack losses due to the flux in no-load operation, clamping plate losses due to no-load flux and end-region losses due to flux from the armature winding MMF. These losses are difficult to estimate analytically, but several semi-empirical equations exist that are based on curve-fitting of experimental measurements on similar existing machines.

In [32] an approximate expression for the end stack losses is given based on estimating the average flux density in the end region based on geometry and a value for specific loss per kg in the end region. Similarly, [65] gives an analytical estimation of the losses of the clamping plate losses in no-load. Comprehensive modeling and analysis of the end region core losses are beyond the scope of this thesis, as detailed 3D finite element simulations would be needed to achieve this [77].

Unanswered research questions

Several aspects regarding the topic of core loss prediction in large hydropower generators remain without sufficient answers or solutions. Based on the literature presented in this section, the following research questions arise:

- Do the existing models for iron losses at 50 Hz give reasonable loss predictions at lower frequencies and rotational speeds?
- Will more detailed core loss models give better, more reliable loss predictions than the loss separation approach?
- How well does the use of correction factors predict the actual losses with different methods?
- How large will the additional iron losses in the stator large hydrogenerators be during converter operation?

2.4 Radial forces with fractional-slot windings

Hydrogenerators are normally salient pole synchronous generators with a relatively low speed of rotation and a high number of poles. Several advantages of fractional-slot windings over integer-slot windings are given in [78], including greater freedom of choice when selecting the number of slots, several alternatives for short-pitching and that it is easier to achieve lower harmonic distortion (i.e. reduced fifth, seventh and higher order harmonics) [79].

Fractional-slot windings produce subharmonic field waves, which are field waves with wavelengths larger than the wavelength of the main harmonic. These subharmonics can cause unwanted parasitic effects [79] like additional losses and problematic radial forces.

When considering potential electromagnetic causes for vibrations in rotating electrical machines, it is primarily radial forces with low harmonic orders that can be problematic. The amplitude of deformation is inversely proportional to m^4 [80], where m is the harmonic order. The radial force component of harmonic order m produces vibrations of mode m. Vibration in the machine is primarily given by the lowest mode of vibration [81]. The lowest mode of vibration is equal to the GCD of Q_s and $2p$ is known to be equal to the number of times the winding pattern repeats itself along the periphery of the airgap.

In the design stage of large hydrogenerators with fractional-slot windings, the chosen combination of stator slots and poles will determine the lowest mode of vibration [81]. If the initial slot/pole-combination results in radial forces with a low harmonic order, the number of slots can be changed to increase the order of the lowest radial force harmonic. If the lowest harmonic order of the radial forces is increased, the risk for having vibration problems is reduced.

Fig. 2.1 illustrates how the radial force component of orders 2 and 4 acts on the stator respectively. For $m = 2$ the force wave spans half the stator periphery, while the force component of $m = 4$ spans only one quarter of the stator periphery.

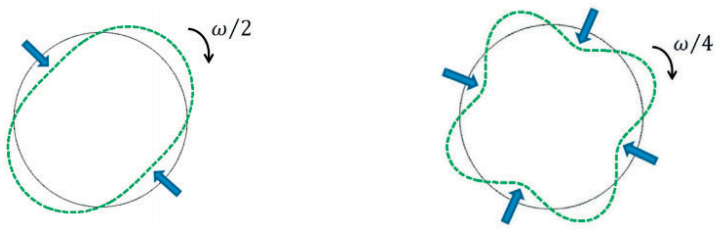

Figure 2.1: Stator deformations for $m = 2$ (left) and $m = 4$, illustration from [82].

The amplitude of the deformation in that stator caused by the radial force harmonic components can be calculated using (2.1) presented in [80].

$$Y_{ms} = \frac{12RR_y^3 f_{rm}}{Eh_{ys}^3(m^2-1)^2} \tag{2.1}$$

where Y_{ms} is the amplitude of the deformation caused by the radial force component of order m with amplitude f_{rm}. R denotes the stator bore radius, R_y is the average radius of the stator yoke, h_{ys} is the stator yoke thickness and E is the elasticity coefficient of Young's modulus.

Fig. 2.2 and Fig. 2.3 were made by the author of this work from data presented in [38,48,50,54,65,69,71,72,79,80,83–95]. The figures contain data from 41 large 50 Hz and 60 Hz hydropower generators presented in the given references. The rotational speeds of the generators are in the range of 75 rpm to 750 rpm and the generators are rated for 2.25-500 MVA. The average power rating of the generators is 125.7 MVA.

Fig. 2.2 shows a relationship between slots per pole and phase (q) and rotational speed. It can be seen that the number of slots per pole and phase tends to increase with rotational speed. Higher rotational speed reduces the number of poles needed to produce 50 Hz or 60 Hz output voltage. It is also found that there seems to be less variation in q in slow rotation run of river generators with rotational speeds below 200 rpm. q seems to vary more at higher rotational speeds.

It should be noted that Fig. 2.2 shows that there is a large variation in the number of slots per pole and phase (q) at all rotational speeds. The variation in q is larger at higher rotational speeds.

Similar to the relationship between q and rotational speed, the relationship between the lowest mode of vibration and rotational speed for the same hydropower generators are presented in Fig. 2.3. The lowest mode of vibration seems to go down when the speed of rotation is increased. Faster rotating machines tend to have smaller diameters and thicker stator yokes than slower rotating machines with a higher pole number.

Generators with lower rotational speeds have, based on Fig. 2.3, a larger variation in the order of the lowest mode of vibration than generators with higher rotational speeds. In addition, the upper value for the lowest mode of vibration is higher for the generators with lower rotational speeds. This shows that the winding layout for slower rotating generators tends to repeat itself more times around the stator bore than the layout of generators with higher roational speeds.

Based on (2.1) it is observed that although the lowest order of vibration m tends to go up when the rotational speed is reduced, the larger diameter and thinner stator yoke work to increase the stator deformation. In conclusion it can be said that the lowest order vibration problem might not be smaller for slower rotating generators than for faster rotating generators, although the lowest mode of vibration tends to be higher for slower rotating generators.

Low-speed generators are more susceptible to experiencing vibration problems than high-speed generators at the same amplitude of the lowest order radial force component [80]. The amplitude of deformation is increased when the diameter of the generator is increased, and when the thickness of the stator yoke is reduced. Both are the case for low-speed generators since they have a high number of poles.

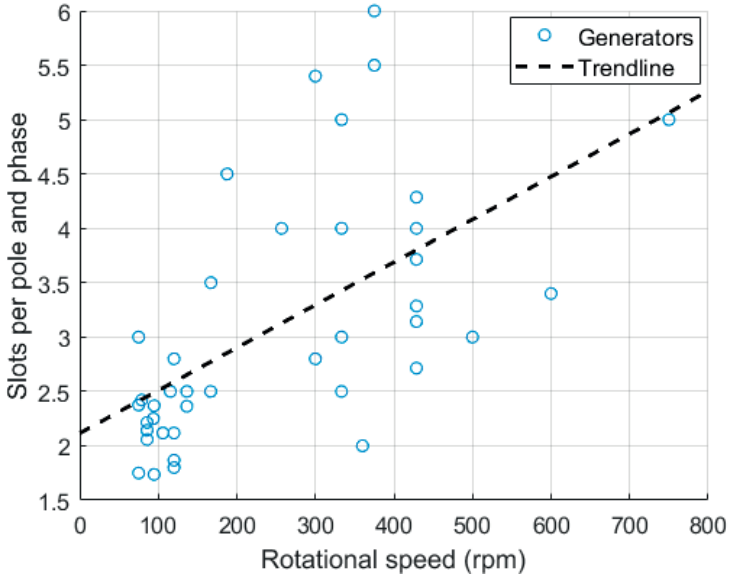

Figure 2.2: Slots per pole and phase in large hydrogenerators, compiled from published literature.

Spatial harmonics of the airgap flux density in two large hydrogenerators with fractional slot windings are studied using time-stepping finite element simulations [80]. One of these generators was studied during converter operation in [42]. Low order force harmonics were found to be unaffected by converter harmonics.

The order of the lowest-order spatial flux density harmonic is equal to the greatest common divisor (GCD) of Q_s and p. Several analytical methods have been used for predicting and analyzing the harmonic content in the airgap of large hydro-

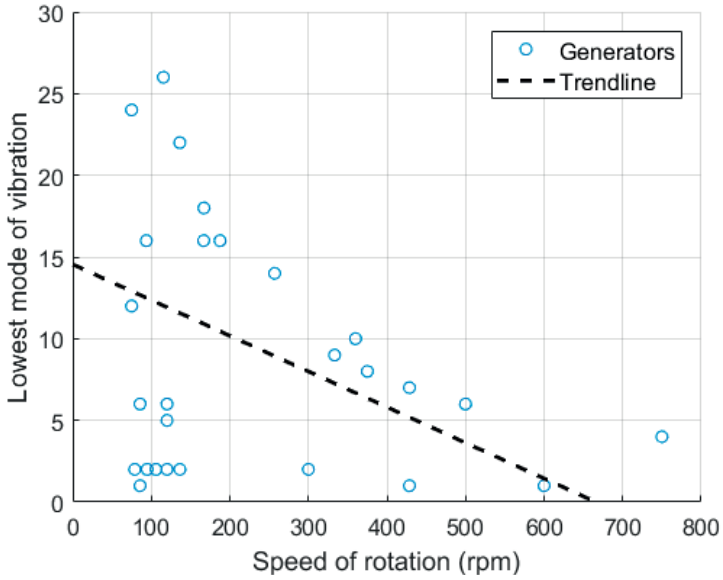

Figure 2.3: Lowest mode of vibration in large hydrogenerators, compiled from published literature.

generators. Often the MMF harmonics are calculated analytically based on the winding layout [94]. The airgap flux density harmonics are then calculated using airgap permeance formulations, where the influence of the permeance of the rest of the generator is assumed negligible [29, 79].

As a consequence of neglecting the reluctance of the non-airgap parts of the generator, it is claimed in [87] that a reduction in the airgap length will give a proportional increase in the main flux density component that interacts to produce most of the lowest order radial force component. Similar studies, where the airgap length is reduced, have not been found for large, salient pole synchronous hydrogenerators.

It is also possible to use the winding factor of the different MMF harmonics [96] to predict the amplitude of the flux density harmonics. These are all simplified methods, and therefore it is impossible to determine whether the amplitudes of the different flux density harmonics are calculated correctly. In order to do this, finite element simulations are needed. The amplitude of the flux density harmonics needs to be calculated correctly if the amplitude of the lowest order radial force component is to be calculated.

The induced electric field in damperbars produces currents in the damper winding, which contribute to weakening the original magnetic field in the airgap [79]. It was

claimed that the damper winding is able to substantially reduce the amplitude of the flux density harmonics that contribute the most to the lowest order radial force component [29]. This claim was based on an analytical winding factor expression for the damper winding that was presented in [79].

In existing, large hydropower generators with fractional-slot windings there are three main methods to reduce vibration problems. First, either the stator side or the rotor side can be remade to reduce the vibration problem.

The stator construction can be modified to change the eigenfrequency, or the number of stator slots can be modified to make the winding into an integer-slot winding. Neither of these options are normally considered to be optimal as they are costly and may lead to other issues related to harmonics and losses.

The last main option is to change the existing winding configuration.

The last option is usually the best and least expensive choice if the generator is already built. An analytical design method for analyzing radial forces in large hydrogenerators, including the effect of damperbars, was presented in [79]. In [97] the effect of changing the winding layout on the level of harmonic distortion and losses is investigated.

It has been shown in [87] that retrofitting a synchronous generator into a doubly-fed induction generator can cause vibration problems. One of the reasons for the vibration problem found in [87] was that the airgap length was reduced. The solution that was chosen was to rearrange the winding configuration. In order to find the optimal winding configuration, the analytical framework presented in [79] for calculating armature MMF was combined with an algorithm [87].

Similarly, in [94], a large hydrogenerator was experiencing low order vibration problems. Different winding layouts were evaluated analytically and compared to the existing winding configuration. By changing the winding pattern, it was possible to reduce the radial force component that caused vibrations considerably.

Unanswered research questions

Some of the research questions on low order radial forces in large hydropower generators with fractional-slot windings that have not been sufficiently addressed in literature are:

- How does a reduced airgap length influence the lowest order radial force component in hydropower generators with a fractional-slot winding?
- What is the effect of damper windings on the lowest order radial force com-

ponent, and how does this change when the airgap length is reduced?

- Are there any efficient methods available to the winding designer that can help mitigate possible vibration problems caused by low order radial forces?

2.5 Summary of research questions

Based on the literature reviewed in this chapter, a list of research questions that do not appear to have been sufficiently answered has been presented in this chapter. The relevant research questions have been presented at the end of each section in the literature review. The unanswered research topics can be grouped into optimal generator design, core loss modeling, additional losses due to converter operation, and radial airgap forces that can cause vibration problems.

Chapter 3

Design and calculation of hydropower generators

This chapter presents a framework for how to size a hydropower generator and calculate the different parameters of the generator. An analytical calculation approach is used as the basis for the design process, and an optimization method that can be used with the analytical design procedure is presented. This chapter covers how to find the main dimensions of the generator, how to dimension the required magnetization, and how to calculate the reactances. A winding layout procedure for fractional-slot windings is presented. Finally, the specifications of the generators used as case studies are given.

3.1 Design process and analytical design method

When designing synchronous hydropower generators, the goal for the designer is to find a set of input variable values that optimize the generator's performance and minimize the total cost of the generator while staying within the given design constraints. To achieve this it is necessary to be able to calculate the electrical, magnetic, thermal and mechanical performance of the generator accurately.

This chapter presents a framework for how to size a hydropower generator and calculate the different parameters for the electromangetic analysis of the generator. An analytical calculation approach that includes optimization algorithms, is used as the basis for the design process. The calculation approach has been implemented in a MATLAB script through the work of several Master's theses at the Department of Electric Power Engineering at the Norwegian University of Science and Technology (NTNU) [90, 98].

The geometric parts of a typical, large hydropower generator are given in Fig. 3.1 and a 3D illustration is presented in Fig. 3.2. The rotor of the generator consists of the rotor yoke/ring, the rotor pole and the magnetizing field winding. The stator consists of the stator yoke, the stator teeth, and the stator winding that is distributed in the stator slots. The geometry of the generator is set by a parameterized list of input variables that allows the designer to design the generator according to the requirements and specifications given.

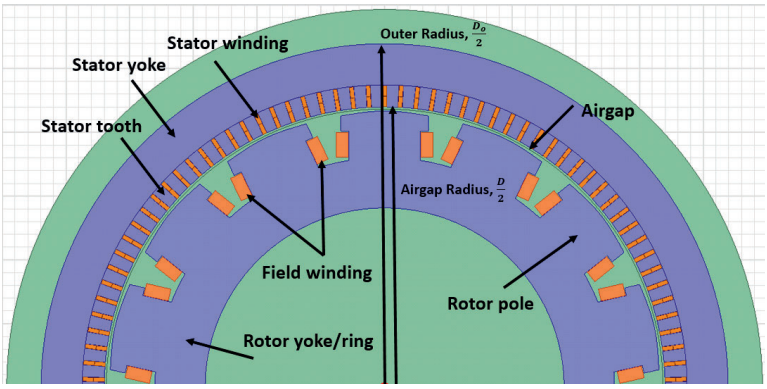

Figure 3.1: Drawing of generator geometry of a typical, large hydropower generator.

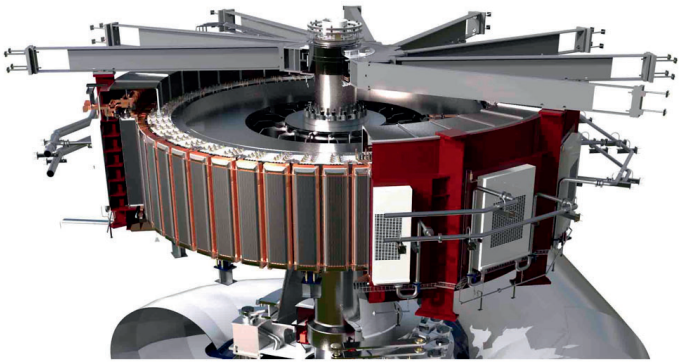

Figure 3.2: Visualization of hydropower generator from GE [99].

The axial design of the generator is illustrated in Fig. 3.3. Large hydropower generators are usually air-cooled. The cooling air typically enters the airgap at both ends of the generator and is sent out through radial ventilation ducts that are distributed along the axial length of the stator. This can be seen in Fig. 3.3, where an actual stator construction with the stator windings installed is shown.

The ventilation ducts are also seen.

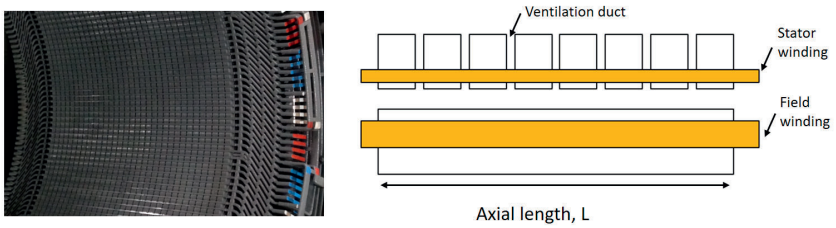

Figure 3.3: Axial design of the generator.

The design process of large synchronous hydrogenerators is restricted by a set of specifications that governs the main dimensions and performance [100]. Design data are primarily:

- Rated power S_N (in MVA)
- Power factor requirement due to grid code
- Rated frequency f_s, rotational speed n_s and runaway speed n_R
- Minimum moment of inertia (given by inertia constant H)
- Per unit synchronous and transient reactances

In addition, there are additional requirements like temperature rise limits for the cooling system and the hydraulic load from the turbine. The temperatures in the different parts of the generator are usually calculated based on thermal equivalent circuit models where the different losses are used as the input heat sources [**?**]. As the literature on how to analytically design salient pole synchronous machines is extensive, only some key parts of the design process relevant for the analysis in this work are presented in detail.

The traditional design process for large hydropower generators can be summarized in Fig. 3.4. First, based on the design specifications, the designer will make an initial design proposal. This first draft is then used to calculate all important parameters in order to check if the proposed generator design is able to meet all operational requirements. If the design does not satisfy all requirements, revisions are made and the calculations are performed on the new design. This procedure is repeated until a final, optimized design that yields the lowest total cost and minimum losses, while satisfying all requirements and constraints, is found.

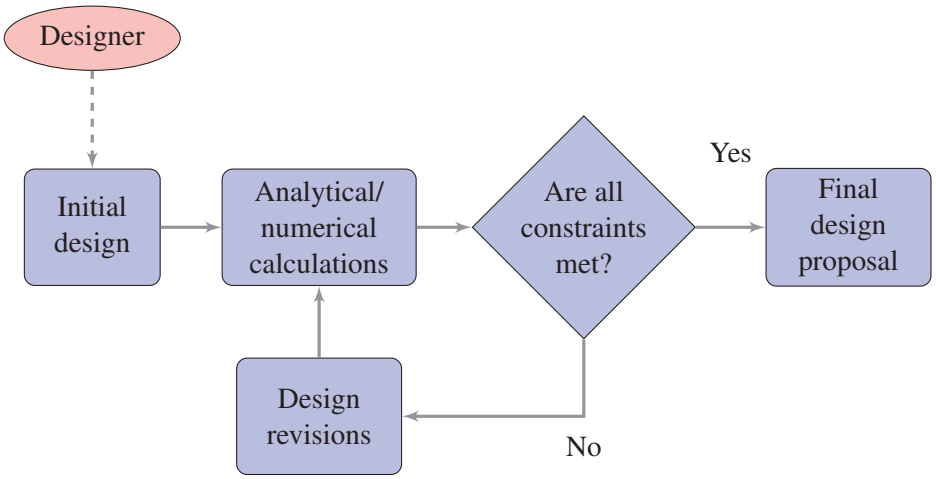

Figure 3.4: Traditional design process.

3.1.1 Main dimensions

The output coefficient C, given by (3.1), is a measure of the power density of the generator, as it relates the main dimensions of the machine to the rated power. Typical values of the output coefficient C for large, air-cooled hydropower generators are between 6 and 8 [101].

Different manufacturers have different empirical formulas for C based on existing generator design practice. A lower output coefficient would indicate that the utilization of the materials in the generator is lower, meaning that the material cost could be reduced by increasing the magnetic and electric loading.

$$C = \frac{S_N}{D^2 L n_s} \tag{3.1}$$

The output coefficient is often set based on empirical data from similar generators. Fig. 3.5 and an empirical expression for the output coefficient (3.2) were created by the author of this work from data presented in [38, 48, 50, 65, 79, 80, 86–88, 90–92, 94]. The figure contains data from 22 large 50 Hz and 60 Hz hydropower generators presented in the given references. The rotational speeds of the generators are in the range of 75 rpm to 750 rpm and the generators are rated for 11-389 MVA. The average power rating of the generators is 125.5 MVA.

This empirical relationship between power rating and output coefficient given in (3.2) is useful as a starting point for the design process in order to estimate the main dimensions of the generator.

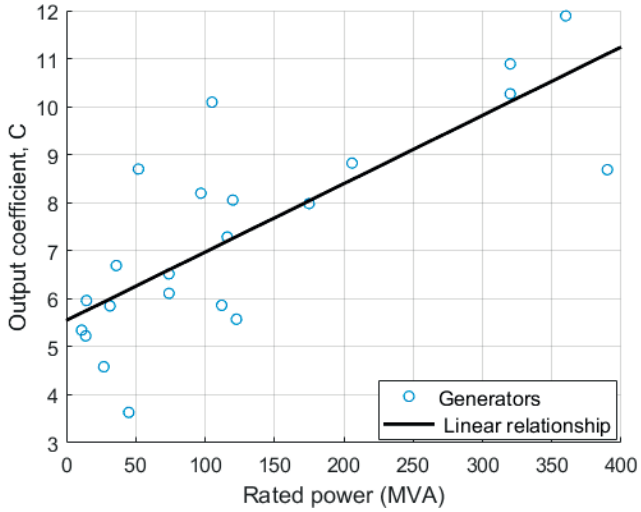

Figure 3.5: Output coefficients for existing generators as a function of rated power, compiled from the published literature.

$$C = 0.0142 \cdot S_N(\text{MVA}) + 5.48 \tag{3.2}$$

The output coefficient is used to determine the stator bore volume D^2L needed to supply the rated output power. There are many combinations of D and L that will give the same volume, and the following paragraphs will present an approach to find the minimum accepted value for D and L that will satisfy the requirement on the moment of inertia for the generator. When D and L are estimated, an initial design can be calculated and used as the starting point of the design process outlined in Fig. 3.4.

In order to set the length and diameter, the expressions for the inertia requirement of the generator are used. Required inertia is governed by the inertia constant H, given by what is needed from the turbine. H can be expressed using (3.3) given in [102].

$$H = \frac{1}{2}\left(\frac{\pi}{60}\right)^2 \cdot \frac{GD^2 n_s^2}{\text{kVA}} \tag{3.3}$$

When the power rating in kVA, the rotational speed and the required inertia constant H are known, the required flywheel effect of the generator (in tm^2) is calculated with (3.3). The flywheel effect is four times the moment of inertia of the

rotor. G is the weight of the rotating mass. The calculated flywheel effect of the generator, GD^2, is used as input in (3.4) that will, when used together with (3.1), give the initial values for the axial length of the generator L and the stator bore D.

$$GD^2 = k \cdot D^4 L \tag{3.4}$$

In (3.4) k is a function of rating, speed and design approach. Normally $k = 2.6 - 2.8$ for generators with high rotational speeds and $k = (0.45 - 0.5) \cdot n_R^{0.25}$ for low-speed generators [100], where n_R is the runaway speed given in rpm.

$$\begin{aligned} D &= \sqrt{\frac{GD^2 C n_s}{S_N k}} \\ L &= \frac{S_N}{D^2 C n_s} \end{aligned} \tag{3.5}$$

When D and L are found using (3.5), D must be checked to see if the mechanical forces at runway speed will be within the acceptable limits. For salient pole wound field winding machines, the maximum tip speed $v_t = \frac{\pi D n}{60}$, where n is the rotational speed, is limited to 150 m/s by the material normally used in the rotor [32].

For hydropower generators with Francis turbines the maximum runaway speed, n_R, is in the range of $1.7n_s$ to $2.0n_s$ [103]. The maximum airgap diameter D_{max} is found with (3.6). If the calculated diameter is larger than the maximum allowed value, the diameter would have to be reduced to the maximum value or less. The axial length of the machine, L, would have to be increased to maintain the same $D^2 L$.

$$D_{max} = \frac{v_t \cdot 60}{\pi \cdot n_R} \tag{3.6}$$

The maximum tip speed limits how large D can be. At higher rotational speeds, the maximum tip speed is reached at lower values for D, meaning that high-speed hydropower generators tend to have smaller diameters and longer axial lengths, see Fig. 3.6. For run-of-river plants, the number of poles is high and the diameter D is larger. This gives a typical design for low-speed hydropower generators with short axial lengths and large diameters, see Fig. 3.7.

The rated power of a salient pole synchronous generator can be expressed by (3.7), where k_w is the winding factor. For large hydropower generators, the stator rms

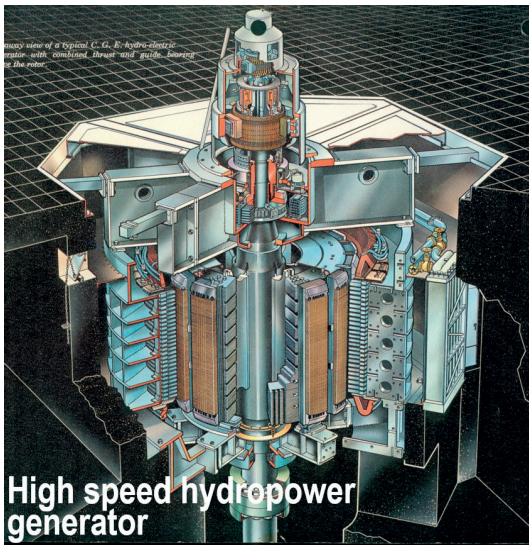

Figure 3.6: High-speed hydropower generator [104].

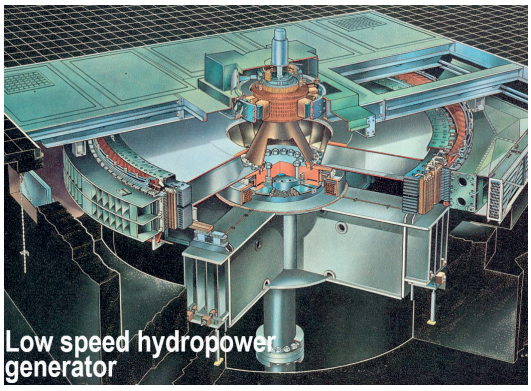

Figure 3.7: Low-speed hydropower generator [104].

line voltage U_n is usually set as one of the design parameters that is not predefined in the design data in order to give freedom to the designer in choosing current loading A, the design of the stator winding and the stator rms phase current I_s. The rated stator voltage can vary from 5 kV to 15 kV, and in some cases hydropower generators can be designed with voltage levels as high as 21 kV.

Combined with (3.1) the output coefficient can be reformulated as (3.8). Now we see that the output coefficient is a function of the electric loading A and the magnetic loading of the machine represented by the airgap flux density B_δ.

$$S_N = \sqrt{3}U_n I_s = \frac{\pi^2}{\sqrt{2}} k_w A B_\delta D^2 L n_s \tag{3.7}$$

$$C = \frac{\pi^2}{\sqrt{2}} k_w A B_\delta \tag{3.8}$$

For a fixed rotational speed and apparent power, an increase in A or B_δ leads to a reduction in the required airgap volume D^2L. The magnetic loading B_δ is limited by the saturation level in the available core material. In the core materials used today, the airgap flux density B_δ is limited to approximately 1.1 T [100]. Normally, large salient pole generators are operated with an airgap flux density of 0.85-1.05 T [78].

For a given airgap volume D^2L and a magnetic loading limited by the maximum B_δ, the required electric loading, A, that gives the estimated output coefficient C is given by (3.9) for the two-layer widing. A is defined as the number of ampere-turns per meter along the airgap periphery. It is defined by the number of stator slots Q_s, the stator current I_s and the stator bore D as:

$$A = \frac{2 I_s Q_s}{\pi D} \tag{3.9}$$

The permitted current loading A and the stator winding current density is limited by the efficiency of the cooling system, the maximum winding temperature rise given by the insulation type that is used, and the synchronous reactance requirement for the given generator. The number of stator slots Q_s is chosen when the winding layout is designed and is limited by several factors, including reactance requirements, as will be further discussed in Sections 3.1.3 and 3.1.4.

Finally, after the current loading A, stator current density and the design of the stator winding, i.e. number of strands, number of parallel paths and number of slots Q_s, is set the stator current I_s is calculated.

It should be noted that the output coefficient C that was found using (3.2), and the calculated values for D and L should be considered starting points for the design. For instance, if A or B_δ are increased it is possible to either decrease the other value or reduce the airgap volume as long as all design constraints are met.

Normally, N_p is given by the rated frequency f_s and the rotational speed n_s given by the turbine. For converter-fed machines, f is not set, meaning that N_p can be varied freely. Increasing N_p reduces the rotor and stator yoke thickness given by (3.10). The value of iron stacking factor, k_{Fe}, is typically between 0.9 and 0.97 [78]. B_y is the design flux density that is desired to have in the yoke.

$$h_y = \frac{B_\delta}{2B_y}\frac{\pi D}{k_{Fe}N_p} \tag{3.10}$$

If the air-gap diameter is kept constant and the pole number is increased, the pole pitch will decrease. By keeping the flux density constant, both the yoke thickness and the core weight are reduced. The outer diameter, D_o, is simply found by using (3.11), where h_s is the height of the stator slots.

$$D_o = D + 2(h_s + h_{ys}) \tag{3.11}$$

3.1.2 Field winding

The field winding must be able to, in no-load, produce enough ampere-turns to sustain the total required magnetomotive force (MMF), F_{mtot}, see (3.12), between a pair of poles. As is illustrated in Fig. 3.8, the total MMF can be separated into the MMF over the airgap, F_δ, the stator teeth, F_{mt}, the stator yoke, F_{msy}, the pole core, F_{mp}, and the rotor ring, F_{mry}. The method for calculating the required MMF in the generator is only presented in brief in order to provide an overview of the procedure.

$$F_{mtot} = F_\delta + F_{mt} + F_{mp} + \frac{1}{2}\left[F_{msy} + F_{mry}\right] \tag{3.12}$$

The MMF over the stator teeth is calculated using Ampère's law along the length of the tooth h_t, see (3.13). More details on how to estimate the MMF can be found in [78].

$$F_{mt} = \int_0^{h_t} H_t \cdot dl \tag{3.13}$$

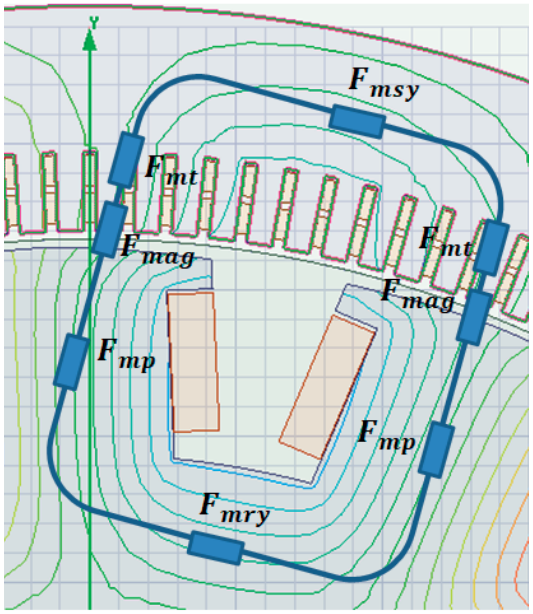

Figure 3.8: Drops in magnetomotive force in the generator.

The MMF over the pole core is calculated similarly using (3.14), where h_{pc} is the height of the pole core, $H_{p,max}$ is the maximum magnetic field intensity and $H_{p,max}$ is the minimum magnetic field intensity.

$$F_{mp} = \int_0^{h_{pc}} H_p \cdot dl = \frac{H_{p,max} + H_{p,min}}{2} \cdot h_{pc} \tag{3.14}$$

The MMF over the airgap is calculated using (3.15), and is determined by the required flux density B_δ, Carter's coefficient for the airgap k_C and the equivalent airgap length δ_{0e}.

$$F_\delta = \frac{B_\delta}{\mu_0} \cdot k_C \delta_{0e} \tag{3.15}$$

The shape of the pole shoe in a salient pole generator is chosen to provide a more sinusoidal flux density by not having a uniform airgap length. As a consequence of this, the equivalent airgap length δ_{0e} can be expressed with (3.16) from [105] where δ_{max} is the maximum airgap length.

$$\delta_{0e} = \delta_0 \cdot \left[1 + \frac{1}{3}\left(\frac{\delta_{max}}{\delta_0} - 1\right)\right] \tag{3.16}$$

Carter's coefficient k_C makes the effective airgap of the machine longer and is given by (3.17), primarily due to slotting in the stator, k_{Cs}, and slotting in the pole shoes to make space for the damperbars, k_{Cr}.

$$k_C = k_{Cs} \cdot k_{Cr} \tag{3.17}$$

Carter's coefficient for slotting in the stator is given by (3.18), where τ_u is the slot pitch and b_u is the stator slot opening.

$$k_{Cs} = \frac{\tau_u}{\tau_u - \frac{b_u/\delta_0}{5+b_u/\delta_0} b_u} \tag{3.18}$$

Carter's coefficient for slotting in the rotor is given by (3.19), b_D is the slot opening for the damperbars and τ_r is damperbar slot pitch.

$$k_{Cr} = \frac{\tau_r}{\tau_r - \frac{b_D/\delta_0}{5+b_D/\delta_0} b_D} \tag{3.19}$$

The MMF over the stator and rotor yokes are found by taking the line integral of the magnetic field H in the yoke from one pole to the next, as given by (3.20). For more details, see [78].

$$F_{msy/ry} = \int H_y \cdot dl \tag{3.20}$$

When the total required MMF is known, it is used to calculate the needed ampere-turns $n_f I_f$ produced by the field winding in no-load, see (3.21).

$$n_f I_f = U_{mtot} \tag{3.21}$$

When the generator is loaded, the field current must be increased to compensate for the effect of the armature reaction. The total magnetization needed for rated load is found through calculating E_f, which, on a per unit basis, tells us how much the magnetization must increase from no-load operation to rated load. The first step to find E_f is to calculate the load angle δ, by using (3.22). All values are

given in per unit in (3.22), (3.24) and (3.25). The approach presented here is based on a generator supplying an inductive load. The procedure is similar for other load situations, and more details can be found in [78]. A phasor diagram illustrating the approach for calculating the required magnetization at rated load is given in Fig. 3.9.

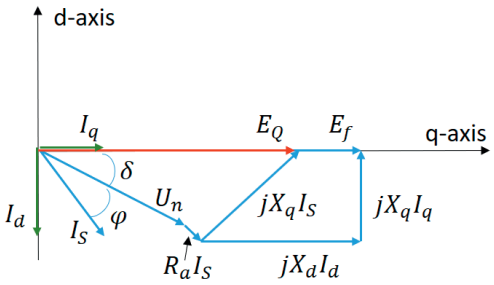

Figure 3.9: Phasor diagram for the generator at rated load.

The details for calculating the stator resistance R_a are provided in Section 3.2.5, while the calculation of the different reactances is explained in Section 3.1.4 .

$$E_Q = U_n + (R_a + jX_q)I_s = |E_Q|\angle\delta \tag{3.22}$$

The current angle α of the stator current I_s is found as the sum of δ and the power factor angle φ, see (3.23). Once α is found, the d-axis current component can be calculated using (3.24).

$$\alpha = \delta + \varphi \tag{3.23}$$

$$I_d = -I_s \sin(\alpha) \tag{3.24}$$

Finally, E_f can be calculated using (3.25) and be used to calculate the total magnetization needed at rated load for the generator with (3.26).

$$E_f = U_n + R_aI_s + jX_qI_s + j(X_d + X_q)I_d = E_Q + j(X_d - X_q)I_d \tag{3.25}$$

$$n_fI_f = F_{mtot} \cdot |E_f| \ \text{(rated load)} \tag{3.26}$$

The number of turns, n_f, and current, I_f, in the field winding is chosen based on available space and the cooling capacity of the machine. Details on how to calculate the number of turns in the field winding and how to design the pole and pole shoe in the rotor can be found in [32, 78].

3.1.3 Stator winding

Synchronous hydropower generators are generally designed with fractional-slot windings. In Fig. 3.10 the stator of a large hydropower generator during the assembly phase can be seen. The stator winding has been installed. The winding layout can be seen, as the different phases are distinguished by the colors, red, white and blue.

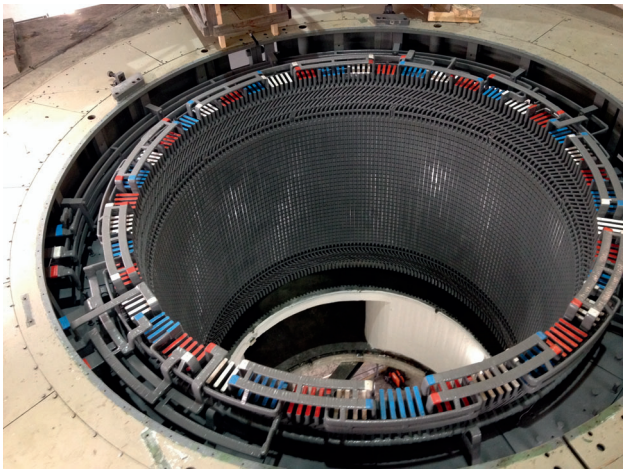

Figure 3.10: Stator of hydrogenerator during assembly phase. Private photo.

When the current loading of the stator A has been estimated, the stator current I_s, the number of stator slots Q_s and the terminal voltage U_n must be decided upon.

In general, fractional-slot windings are windings where the number of stator slots (Q_s) divided by the number of phases (m) and rotor poles (N_p) gives a fractional number (q) (see (3.27)).

$$q = \frac{Q_s}{m \cdot N_p} = \frac{z}{d} = b + c/d \tag{3.27}$$

For all winding arrangements, in order to achieve a balanced winding, Q_s must be divisible by the number of phases m. For three-phase fractional-slot windings there is another requirement for balance. The denominator d in (3.27) cannot con-

tain 3^p as a factor [65]. If N_p contains a factor 3^p, then Q_s must also contain a factor 3^p in order for the winding to be balanced.

The maximum number of parallel circuits in a stator winding is set by how many times the winding is repeated along the circumference of the stator. The number of times that the winding repeats itself t is found as the greatest common divisor (GCD) between Q_s and $N_p/2$.

Based on the requirements for achieving a balanced winding, the designer is free to choose the number of slots Q_s. After selecting a value for Q_s, the performance and the parameters of the generator are calculated to ensure that the proposed design is within all the given constraints. Since the terminal voltage of the generator is not set, the designer is given more freedom to meet the requirements of the specific generator. This procedure for selecting the number of stator slots Q_S can take several iterations to find an optimal design.

There are only odd harmonics present in the airgap MMF distribution when Q_s/t is even. When Q_s/t is odd, both odd and even harmonics are present. Only harmonics that are multiples of t will be present [106]. Another way of finding the number of repeatable winding parts, is to divide N_p by d [107]. In addition, the maximum number of parallel circuits must be divisible by the chosen number of parallel circuits, i.e. the number of parallel circuits must be a factor in the maximum number of parallel circuits.

A general procedure for the layout of balanced, three-phase fractional slot windings based on the star of slot voltages as presented in [108, 109] is used as the basis for the analysis presented in Chapter 6.

In salient pole synchronous hydropoer generators, the stator coils are usually made of Roebel bars with one turn per coil. A cross section of a typical double-layer stator winding in one stator slot is presented in Fig. 3.11. Each stator bar is made of Roebel bar strands in parallel with an insulation layer around each bar. Between each bar and between the parallel strands there are insulating strands. There is typically a slot wedge on top of the upper layer to maintain the winding in the slot. A typical end-winding connection of a double-layer winding is also presented in Fig. 3.11.

The winding factor k_w tells us how effectively a coil and winding utilize the available flux per pole. It is desirable that the winding factor is high for the main harmonic of the flux and low for the flux of the other harmonics present in the flux. A short pitched winding is usually preferred for fractional-slot windings in order to reduce the amplitude of the other winding flux harmonics that are present.

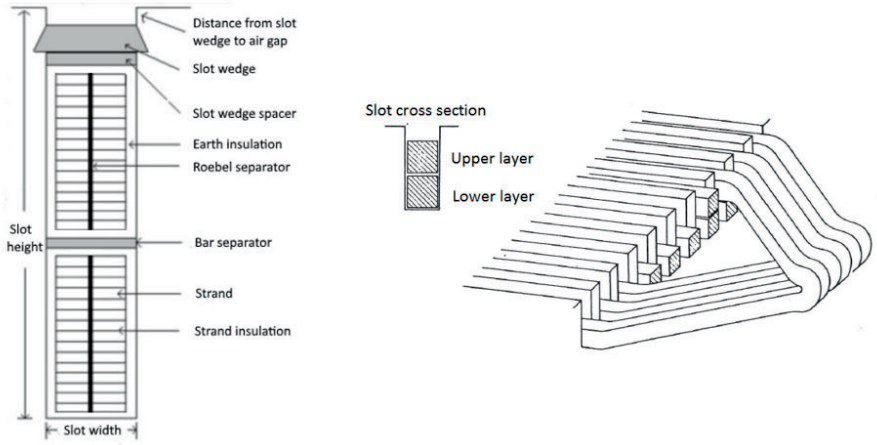

Figure 3.11: Illustration of stator winding cross section from [98] (left), and end-winding connections from [101].

Fig. 3.12 provides a simple illustration of a short pitched and a full pitched winding layout. In a short pitched winding, one stator bar is connected to a stator bar that is closer than a full pole pitch, τ_p away from it. This reduces the amount of flux passing through this coil compared to a full pitched winding.

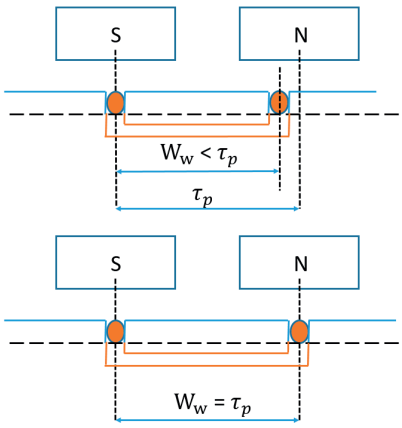

Figure 3.12: Illustration of short pitched winding (top), and full pitched winding [101].

The winding factor for the fundamental harmonic, k_w, see (3.28), is given as the product of the distribution factor, k_d, and the pitching factor, k_p, for the fundamental harmonic. As presented in [78], k_d is given by (3.29) and k_p is given by

(3.30), where $\frac{W_w}{\tau_p}$ is the relative coil pitch.

$$k_w = k_d \cdot k_p \tag{3.28}$$

$$k_d = \frac{\sin\left(\frac{\pi}{2m}\right)}{q \sin\left(\frac{\pi}{2mq}\right)} \tag{3.29}$$

$$k_p = \sin\left(\frac{W_w}{\tau_p}\frac{\pi}{2}\right) \tag{3.30}$$

The electrical angle between two stator slots α_s, see Fig. 3.14, is given by (3.31) where $\alpha_s^{'}$ is a reduced angle as described in the expression for the slot angle.

$$\alpha_s = \frac{2\pi}{Q_s} N_p = \frac{\pi}{mq} = \frac{\pi}{mz} \cdot d = \alpha_s^{'} \cdot d \tag{3.31}$$

A general procedure for the layout of balanced, three-phase fractional slot windings based on the star of slot voltages as presented in [108, 109] is used. The span from one pole to the next covers 180° electrically, which in a balanced three-phase system is separated into three phase belts of 60° each. This phase belt is then divided into z boxes spanning $\alpha_s^{'}$ degrees. The angle difference between two slots was shown in (3.31) to be $d \cdot \alpha_s^{'}$. If slot 1 is placed at 0°, then the next slot is placed in the box that is at an angle of $0^\circ + d \cdot \alpha_s^{'}$ and so on.

By using this approach it is possible to obtain a layout procedure similar to the one presented in Fig. 3.13, which can be used for any balanced three-phase fractional-slot winding.

Fig. 3.14 shows the voltage star of vectors for the first half of the example generator with 18 slots and 4 poles as the winding pattern repeats itself every two poles. The figure also shows how the resulting balanced three-phase system of voltages is produced by combining the slot voltages following the procedure presented in Fig. 3.13.

The winding layout for the generator G3 in Table 3.5 is presented in Table 3.1, and is produced by following the same design procedure as in the example case. The winding layout in Table 3.1 is made based on the method in Fig. 3.13. Table 3.1 has the same number of columns as the number of poles the winding uses to complete one layout pattern before it starts to repeat itself. The number of rows is equal to the number of phases. Each slot in the table is filled by counting the

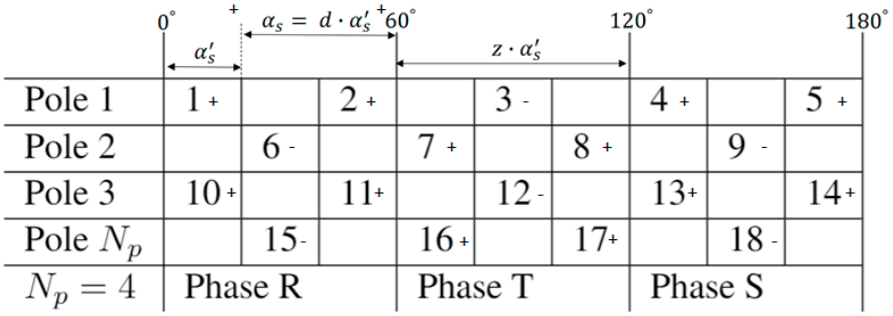

Pole 1	1 +		2 +		3 -		4 +		5 +
Pole 2		6 -		7 +		8 +		9 -	
Pole 3	10 +		11 +		12 -		13 +		14 +
Pole N_p		15 -		16 +		17 +		18 -	
$N_p = 4$	Phase R			Phase T			Phase S		

Figure 3.13: Winding layout procedure example. One of the simplest fractional-slot windings possible with $q = 1.5$, $N_p = 4$, $Q_s = 18$. The numbers in the table denotes the slot number. Current direction in each slot is indicated with + and -.

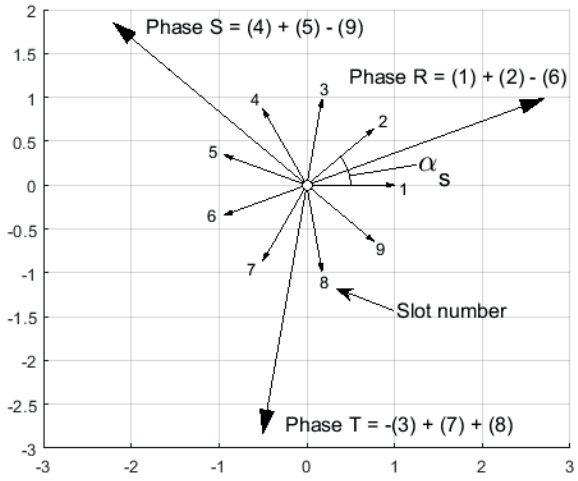

Figure 3.14: Resulting star of voltage vectors including voltage vectors for each slot and the resulting three-phase system. All values in per unit. One of the simplest fractional-slot windings possible with $q = 1.5$, $N_p = 4$, $Q_s = 18$. The numbers in the figure denotes the slot number.

number of slots in phase R, S or T in Fig. 3.13 respectively. For example, in Table 3.1, the first pole in Fig. 3.13 would have five slots in phase R, four slots in phase -T and four slots in phase S.

The presented procedure for winding layout is used in Chapter 6 as the basic

Table 3.1:
Winding layout for large hydrogenerator with 180 slots and 14 poles.

RRRRR	-T-T-T-T	SSSS	-R-R-R-R-R	TTTT	-S-S-S-S	RRRR
-T-T-T-T	SSSS	-R-R-R-R	TTTTT	-S-S-S-S	RRRR	-T-T-T-T
SSSSS	-R-R-R-R	TTTT	-S-S-S-S-S	RRRR	TTTT	SSSS

method for the winding layout. When short pitching the double layer winding, one of the layers is displaced by the number of slots that the winding is to be short-pitched by relative to the other layer.

3.1.4 Reactance calculations

The synchronous reactance, X_d, consists of the armature reaction component, X_{ad}, and the flux leakage component, X_l, see (3.32). Armature reaction is the main component of the synchronous reactance.

$$X_d = X_{ad} + X_l \tag{3.32}$$

The main component of the synchronous reactance is the armature reaction reactance given by (3.33).

$$X_{ad} = k_{d1} \frac{F_a}{F_\delta} \tag{3.33}$$

k_{d1} is a reduction coefficient of the d-axis magnetizing reactance in machines with salient poles. An expression for k_{d1} for salient poles with constant airgaps is given as (3.34) in [68] where $\frac{\tau_p}{\tau}$ is the relative pole arc.

$$k_{d1} = \left[\frac{\tau_p}{\tau} + \frac{1}{\pi} \sin \frac{\tau_p}{\tau} \pi \right] \tag{3.34}$$

By correcting for the fact that the airgap is not uniform, k_{d1} can be expressed using (3.35), where δ_{max} is the maximum airgap length.

$$k_{d1} = \left[\frac{\tau_p}{\tau} + \frac{1}{\pi} \sin \frac{\tau_p}{\tau} \pi \right] \cdot \left[1 + \frac{1}{3} \left(\frac{\delta_{max}}{\delta_0} - 1 \right) \right] \tag{3.35}$$

For traditional designs with a relative pole arc of 0.7, an average value of 0.83 can be used [105]. The MMF of the armature winding, as shown in [78], is given in (3.36) where I_c is the current in each stator bar.

$$F_a = \frac{4}{\pi}\frac{3}{2}\sqrt{2}I_c a k_w \frac{Q_s}{N_p} = \frac{4}{\pi}\frac{3}{2}\sqrt{2}I_s k_w \frac{Q_s}{N_p} \tag{3.36}$$

Similarly, [78] expresses MMF over the airgap as (3.37).

$$F_\delta = \frac{B_\delta}{\mu_0}\delta_0 \cdot k_C \tag{3.37}$$

By combining (3.33), (3.36) and (3.37), the expression for the armature reaction reactance is given as (3.38).

$$X_{ad} = k_{d1}\mu_0 \cdot \frac{6\sqrt{2}}{\pi}\frac{I_s k_w Q_s}{B_\delta \delta_0 k_C N_p} \quad (p.u.) \tag{3.38}$$

Using (3.38), one can see that the synchronous reactance is inversely proportional to both N_p and δ_0. X_d gives a measure of the machine magnetization current [110]. A larger air gap gives a smaller X_d, and more field winding ampere-turns to produce the same apparent power [32].

Reactance calculations were compared with measurements from three existing hydrogenerators using design specifications given in [88]. The generators have power ratings of 36, 52 and 320 MVA respectively. The results are given in Table 3.2. The calculated values are somewhat lower than the measured values for generator GI. For GII and GIII, the synchronous reactances calculated matches well with the measured values.

Table 3.2:
Comparison between calculated and measured reactance values from [88]

	G_I		G_{II}		G_{III}	
Symbol	M	C	M	C	M	C
X_d (p.u.)	0.98	0.97	0.96	0.97	1.25	1.28
M - measured value			C - calculated value			

The total leakage inductance, L_σ, is given by (3.39), and the leakage reactance is given as $X_l = 2\pi f_s L_\sigma / Z_b$ (p.u.). Z_b is the base impedance. Details for how to calculate the different components of the leakage inductance have not been provided here, but can be found in [32, 78, 111].

$$L_\sigma = L_\delta + L_u + L_d + L_w + L_{sq} \tag{3.39}$$

The different components of the leakage inductance are:

- L_δ, the airgap leakage inductance
- L_u, the leakage inductance due to slotting in the stator
- L_d, the tooth tip leakage inductance
- L_w, the end-winding leakage inductance
- L_{sq}, the leakage inductance due to skewing

The generators analyzed in this work do not have skewing. Therefore the leakage inductance due to skewing is not relevant here.

3.2 Losses

3.2.1 Mechanical losses

Bearing and windage losses in electrical machines can be calculated using several methods. Mechanical losses include losses in bearings and windage loss due to the cooling airflow within the machine. There are several methods for calculating these losses. The developments in computational fluid dynamics and available computational resources allows for detailed simulations of the airflow in electrical machines. These simulations are still time-consuming, and the uncertainty in the results can be significant.

Formulas for calculating the bearing and windage losses are generally based on curve fitting of loss measurements to machine length, diameter and rotational speed. Different textbooks on electrical machine design present variations to these formulas. Here, (3.40) given by [109] is used.

$$\begin{aligned} P_{fr} &= k_v D^3 n^2 \sqrt{L} \cdot 10^{-5} \quad \text{(kW)} \\ k_v &= 0.8(1.7 + 0.4D) \left(\frac{1.75}{D}\right)^{0.1} \left(\frac{n}{428}\right)^{0.4} \end{aligned} \tag{3.40}$$

3.2.2 Finite element methods for calculating iron losses

Method A: Loss-separation based on curve fitting of loss data (Bertotti)

A popular method for stator core loss estimation ,P_{iron}, is the loss-separation method (3.41) presented by Bertotti [58]. Loss-separation divides the core losses

into hysteresis loss P_h, classical eddy current loss P_c and excess or anomalous losses P_e.

$$\begin{aligned} P_{iron} = P_h + P_c + P_e &= k_h f B_m^2 + k_c f^2 B_m^2 + k_e f^{1.5} B_m^{1.5} \\ &= K_1 B_m^2 + K_2 B_m^{1.5} \end{aligned} \tag{3.41}$$

In (3.41), k_h denotes the hysteresis loss coefficient, k_e the excess loss coefficient, f the frequency and B_m the peak magnetic flux density. The coefficients K_1 and K_2 represent the terms that are a function of B^2 and $B^{1.5}$ respectively. K_1 and K_2 are given by (3.42). k_c is the classical eddy loss coefficient found using (3.43) where σ is the conductivity of the material and d is the lamination sheet thickness.

$$\begin{aligned} K_1 &= k_h f + k_c f^2 \\ K_2 &= k_e f^{1.5} \end{aligned} \tag{3.42}$$

$$k_c = \pi^2 \sigma \frac{d^2}{6} \tag{3.43}$$

A least square approach, see (3.44), is used to find K_1 and K_2 based on loss data given by the manufacturer of laminated steel.

$$\min_{\mathbf{K_1},\mathbf{K_2}} \quad f(K_1, K_2) = \sum \left[P_{iron,i} - \left(K_1 B_i^2 + K_2 B_i^{1.5} \right) \right]^2 \tag{3.44}$$

$P_{iron,i}$ is the loss data for combination i of flux density and frequency from the data sheet. The least square approach can be used for data at one or several frequencies. When curves for several frequencies are used to find the coefficients, it has been shown that the fitting are in agreement with the curve for the highest frequency curves while overestimating lower frequency losses.

In [112] loss curves for 50 Hz, 100 Hz, 200 Hz, 400 Hz, 1000 Hz and 2000 Hz for the laminated steel type M235-35A were used to calculate the loss coefficients of the Bertotti model. The 50 Hz losses were overestimated by more than 100% although the overall loss prediction error was only 1.5%. Since the bulk of the losses are caused by the lowest frequency, i.e. 50 Hz, only 50 Hz loss data are used when the least square method is used to find K_1 and K_2 in this chapter.

Knowing K_1 and K_2 we can find k_h and k_e using (3.45) where f_0 is the frequency that was used to obtain the loss curve.

$$\begin{aligned} k_h &= \left(K_1 - k_c f_0^2\right)/f_0 \\ k_e &= K_2/f_0^{1.5} \end{aligned} \tag{3.45}$$

The frequency domain model given by (3.41) is not suitable for time-stepping analysis. In order to use the loss separation method, the expression for hysteresis, eddy current and excess losses need to be modified. Hysteresis loss is modeled using (3.46) given by [113].

$$P_h(t) = H_{irr}\frac{dB_m}{dt} \tag{3.46}$$

Where H_{irr} is the irreversible component of the hysteresis loop given in (3.47).

$$H_{irr} = \frac{1}{\pi} \cdot B_m \cos(\theta) \tag{3.47}$$

θ is found by expressing the hysteresis loop as an equivalent elliptical loop having the same area as the hysteresis loop [113], where $B = B_m \sin(\theta)$. The modified expressions for eddy current and excess loss given by (3.48) and (3.49).

$$P_c(t) = \frac{1}{2\pi^2}k_c \cdot \left(\frac{dB}{dt}\right)^2 \tag{3.48}$$

$$P_e(t) = \frac{1}{C_e}k_e \cdot \left|\frac{dB}{dt}\right|^{1.5} \tag{3.49}$$

$C_e = 8.763$ from integration of the expression $C_e = (2\pi)^{1.5} \cdot \frac{2}{\pi}\int_0^{\frac{\pi}{2}} \cos\theta^{1.5} d\theta$.

Method B: Vector hysteresis model (Vector-Preisach)

Using the Preisach approach, the hysteresis losses, P_h, are calculated using (3.50). The eddy current losses are found using (3.48).

$$P_h(t) = \frac{1}{T_p}\int_{T_p} \mathbf{H} \cdot \frac{d\mathbf{B}}{dt}\, dt \tag{3.50}$$

Hysteresis has been modeled by the Vector-Preisach model, using angularly distributed scalar reversed Preisach models with $\mathbf{B}$ as input and $\mathbf{H}$ as output [114]. The classical Preisach-model can be expressed as (3.51) according to [115].

$$y(t) = \Gamma[u](t) = \iint_{\alpha \geq \beta} \mu(\alpha, \beta)[\gamma_{\alpha\beta} u](t)\, d\alpha\, d\beta \tag{3.51}$$

where $y(t)$ is the output of the Preisach model. $[\gamma_{\alpha\beta} u](t)$ is called the elementary Preisach hysteron since it is the basic block from which the Preisach operator $\Gamma[u](t)$ is constructed. The parameters α and β are increasing and decreasing values of the input $u(t)$, while $\mu(\alpha, \beta)$ is a distribution function.

A fixed-point procedure is used to connect the Preisach model and the finite element solution. The flux density $\mathbf{B}$ is found from the magnetic vector potential. Using $\mathbf{B}$ as input, $\mathbf{H}$ is found from the Preisach model using the fixed-point process using (3.52) [116].

$$\mathbf{H} = \nu_f \mathbf{B} + \mathbf{R} \tag{3.52}$$

Here ν_f is the fixed-point coefficient and $\mathbf{R}$ is a residual nonlinearity that is determined iteratively. In the inverted version of the Preisach model, the governing equation in the finite element model is given in [117].

where N_{cn}, S_n, i_n and β_n are the number of turns of a coil of phase n, the cross section of the nth phase coil side, and the current in phase n respectively. $\beta = 1$ for coil sides with a positive direction and $\beta = -1$ for coil sides with a negative direction. σ is the conductivity of the material, A is the z-component of $\mathbf{A}$, t is time and $\mathbf{R}$ is the residual nonlinearity from (3.52).

One of the issues with the Preisach model is that it is difficult to model the hysteresis curves at saturation [118]. This may lead to numerical problems in simulation which can lead to an overestimation of the core losses. The hysteresis loops of ferromagnetic materials can be measured accurately up to 1.4 T to 1.6 T. For parts of an electrical machine the flux densities can be higher than this. In finite element programs, the BH curve is often needed to be continuously defined up to 2 T and even higher [75].

Without further modeling of the BH-curve, this will provide an overestimation of the product between B and H and with it the core losses. Several improvements have been introduced to solve the problem of saturation. In [74] a model is proposed that corrects the angle between the B and H vector in saturation so that the overestimation of the losses is reduced, and in [75] bicubic spline algorithms were proposed to model the BH-curve at saturation to give more realistic hysteresis behavior.

3.2.3 Analytical method for calculating iron losses

Iron losses primarily consist of hysteresis losses, eddy current losses and excess loses due to other effects. It is difficult to determine the exact distribution between hysteresis and eddy current losses [70]. Normally this is estimated based on curve fitting of loss measurements using an Epstein frame.

Traditionally, in order to calculate core losses, some version of Steinmetz's equation for core loss has been used. The general version of Steinmetz's equation is given in (3.53).

$$P_{iron} = P_{10} \cdot \left(\frac{f}{50}\right)^{a_f} \cdot \left(\frac{B}{1.0}\right)^{a_b} \cdot m_{iron} \tag{3.53}$$

The coefficients a_f and a_b are found from curve fitting of loss data at different frequencies and levels of flux density. P_{10} is the specific losses (W/kg) at 1.0 T and 50 Hz and m_{iron} is the mass of iron. Here losses are assumed proportional to frequency to the power of 1.3. The power coefficients of the losses are based on material data originally presented in [111]. Based on this, the version of the Steinmetz equation used is given in (3.54).

$$\begin{aligned} P_{iron} &= \left(\frac{f}{50}\right)^{1.3} \cdot [P_{yoke} + P_{teeth}] \\ P_{yoke} &= k_1 P_{10} B_{ys}^2 \cdot m_{ys} \\ P_{teeth} &= k_2 P_{10} \left(\frac{B_{d,max} + B_{d,min}}{2}\right)^2 \cdot m_{ts} \end{aligned} \tag{3.54}$$

B_{ys}, $B_{d,max}$ and $B_{d,min}$ are the stator yoke flux density, the maximum tooth flux density and the minimum tooth flux density respectively. In order to take rotational fields, effects from manufacturing/machining and harmonics in different parts of the iron into account, correction factors k_1 and k_2 are set to 1.6 and 2.0 respectively [78].

The weight of the stator teeth, m_{ts}, is found using (3.55) as given by [119]. L_n is the iron length when the ventilation ducts are excluded, $b_{t,mean}$ is the mean width of the stator tooth, h_s is the height of the stator slot and Q_s is the number of stator slots. γ_{Fe} is the mass density of iron and k_{Fe} is the stacking factor of the iron core.

$$m_{ts} = b_{t,mean} \cdot h_s L_n Q_s \cdot \gamma_{Fe} k_{Fe} \tag{3.55}$$

The weight of the stator yoke, m_{ys}, is found by assuming that the volume of the yoke is the volume of a hollow cylinder. When the volume is found this is multiplied by the mass density of iron. D_o is the outer diameter of the stator.

$$m_{ys} = \pi \left[\left(\frac{D_o}{2} \right)^2 - \left(\frac{D + 2h_s}{2} \right)^2 \right] \cdot L_n \cdot \gamma_{Fe} k_{Fe} \tag{3.56}$$

3.2.4 Pole surface losses

This section presents a framework for estimating the pole surface losses in the generator analytically. The MATLAB script used for the analytical design investigations in this thesis has been expanded to include the method for calculating pole surface losses presented here.

Flux density harmonics in the airgap induce losses in the surface of the pole shoes. These losses include harmonics due to the stator slot ripple at no-load, the interaction of the slot ripple permeance and the armature MMF at load and higher order MMF harmonics. No-load surface losses $P_{ps,no-load}$ is given by (3.57) where the expression for the armature reaction (3.38) is inserted into the loss expressions given in [32].

$$P_{ps,no-load} = 232d \left[(k_{Cs} - 1) B_\delta \tau_u \right]^2 N_p A_p \left(\frac{Q_s n_s}{60} \right)^{1.5} \quad (kW) \tag{3.57}$$

where d is the thickness of the pole shoe laminations, k_{Cs} is the stator slotting Carter's coefficient, B_δ denotes the airgap flux density, τ_u the stator slot pitch, N_p the number of poles and A_p the airgap surface area of each pole. Q_s denotes the number of stator slots and n_s the rotational speed in rpm. In addition to the pole surface losses at no-load, there are losses due to the impact which the slotting of the stator has on the armature MMF $P_{ps,full-load}$ given by (3.58) [32].

$$P_{ps,full-load} = K' \left(\frac{1}{(k_{Cs} - 1)} \cdot k_{d1} \frac{6\sqrt{2}}{\pi \mu_0} \frac{I_s k_w}{B_\delta \delta_0 k_c} \right)^2 P_{ps,no-load} \quad (kW) \tag{3.58}$$

$K^{'} = 0.2$ is a parameter that takes into account the fact that the airgap is longer at the sides of the pole face [32]. I_s is the stator current, k_C is the total Carter's coefficient, k_{d1} is the coefficient given by (3.35), k_w is the total winding factor and δ_0 is the physical airgap length.

The surface loss due to higher order MMF harmonics when there are damper windings $P_{ps,full-load}^{armature}$ can be estimated using by (3.59) [120]. If no damperbars are installed, $P_{ps,full-load}^{armature}$ can be estimated using (3.60) from [32] instead.

$$P_{ps,full-load}^{armature} = \frac{1.85 N_p N_B L_B C_B K_{f300}}{A_B} \left(\frac{\tau_p}{k_c \delta_0} \right)^2 \\ \ldots \cdot \left[\frac{\frac{k_{d1}}{2000} \frac{6}{\pi} \sqrt{2} I_s k_w \frac{Q_s}{N_p}}{\frac{(t_2 - b_{sh})}{k_C \delta_0} / (1 - \cos \delta_B) + (1 - 0.64 \frac{\tau_p}{L_{ew}} \beta)} \right]^2 \cdot 10^{-8} \quad (kW) \tag{3.59}$$

where N_B, L_B, C_B and A_B is the number of damperbars per pole, the length of each damperbar, the ratio of the damperbar resistivity compared to the resistivity of copper and the cross section of each damperbar respectively. L_{ew} is the end winding length, β is the winding short pitch ratio, b_{sh} is the damper winding slot opening, τ_p is the pole pitch and t_2 is the damper bar pitch. $K_{f300} = 1.96 d_B \sqrt{1/C_B}$ and $\delta_B = 6 t_2 / \tau_p \cdot \pi$ radians, where d_B is the damperbar diameter.

$$P_{ps,full-load}^{armature} = \frac{2.1}{\sqrt[3]{q}} \left(\frac{K_{ch}}{(k_{Cs} - 1)} \cdot k_{d1} \frac{6\sqrt{2}}{\pi \mu_0} \frac{I_s k_w}{B_\delta \delta_0 k_c} \right)^2 P_{ps,no-load} \quad (kW) \tag{3.60}$$

where q denotes the number of slots per pole and phase and K_{ch} is a factor dependent on the pitching of the winding. K_{ch} is in the range between 0.05 and 0.06 for a short pitch ratio of 0.8 to 0.87 [32].

The total pole surface losses, P_{ps}, are given as the sum of no-load losses, full-load losses and additional full-load losses due to higher order harmonics (3.61).

$$P_{ps} = P_{ps,no-load} + P_{ps,full-load} + P_{ps,full-load}^{armature} \tag{3.61}$$

3.2.5 Copper losses

Method for calculating copper losses

The copper losses in the stator winding of the machine are given by (3.62). The DC resistance is given by (3.63) where ρ is the copper resistivity, $A_{cu,s}$ the stator winding copper cross section, and a the number of parallel circuits. Losses in the field winding are calculated in a similar manner.

$$P_{cu,dc} = 3R_{dc} \cdot I_s^2 \tag{3.62}$$

$$R_{dc} = \frac{\rho L_\phi}{A_{cu,s} a} \tag{3.63}$$

The copper length of one phase winding is calculated using (3.64). Here L_{av} is the average length of each winding given by (3.65) [78], D is the airgap diameter, Q_s is the number of stator slots and W_w is the coil span in number of slots.

$$L_\phi = \frac{L_{av} Q_s}{3a} \tag{3.64}$$

$$L_{av} = 2L + 2.8\frac{\pi D}{Q_s} W_w + 0.4 \tag{3.65}$$

In addition to the equivalent DC losses, different harmonic components of the current gives additional copper losses. The current waveform is extracted from the finite element simulation, and a Fourier transform is used to obtain the harmonic spectrum. The main AC eddy-current loss component is calculated using the 50 Hz harmonic of the current waveform and the same analytical method as for the higher order current harmonics using (3.66).

The higher order current harmonics from the FEM simulation are used as an input for calculating the additional AC copper losses due to converter operation using (3.66). After the harmonic spectrum of the stator current is known, the AC resistance is calculated for each harmonic frequency and the AC losses are found using (3.66) where ν denotes the harmonic.

$$P_{cu,ac} = 3\sum (R_{ac,\nu} - R_{dc}) I_{s,\nu}^2 \tag{3.66}$$

Each current harmonic experiences its own effective resistance R_{ac} given by (3.67) which consists of the AC resistance of the end winding R_{end} and the AC resistance components from upper layer bar $R_{ac,u}$ and the lower layer bar $R_{ac,l}$. The AC resistance of the end winding is usually considered equal to the DC resistance [109].

$$\begin{aligned} R_{ac} &= R_{end} + R_{ac,u} + R_{ac,l} \\ &= \frac{R_{dc}}{L_\phi} \left[\left[L_\phi - \frac{2LQ_s}{3a} \right] + (k_{R,u} + k_{R,l}) \frac{LQ_s}{3a} \right] \end{aligned} \tag{3.67}$$

Due to skin and proximity effects, the AC resistance R_{ac} is k_R times higher than the DC resistance. In the case of a two-layer winding, the AC resistance factor k_R is not the same for each layer. The expression for the upper layer $k_{R,u}$ is given by (3.68) from [78], while the lower layer resistance factor $k_{R,l}$ can be calculated by (3.69).

$$k_{R,u} = \varphi + \frac{z_t^2 - 1}{3}\psi \tag{3.68}$$

$$k_{R,l} = k_{R,u}\left(1 + \frac{2z_t^2}{3}\xi^4\right) \tag{3.69}$$

Skin effect makes the subconductor height seen by each harmonic ξ given by (3.70) smaller than the physical strand thickness h_{c0} [78]. z_t is the number of strands in the conductor, f is the harmonic frequency, σ_c is the conductivity of the conductor, z_a the number of parallel strands, b_{c0} is the strand width and b_u the slot width. φ and ψ given by (3.71) and (3.72) are factors that are dependent on the reduced conductor height ξ [78].

$$\xi = h_{c0}\sqrt{\pi f \mu_0 \sigma_c \frac{z_a b_{c0}}{b_u}} \tag{3.70}$$

$$\varphi(\xi) = \xi\frac{\sinh 2\xi + \sin 2\xi}{\cosh 2\xi - \cos 2\xi} \tag{3.71}$$

$$\psi(\xi) = 2\xi\frac{\sinh \xi - \sin \xi}{\cosh \xi + \cos \xi} \tag{3.72}$$

3.3 Radial forces

Radial magnetic forces are among the main sources for vibration in the generator. In order to calculate the radial force density, the Maxwell stress tensor is employed to calculate the radial force density f_r with (3.73).

$$f_r = \frac{1}{2\mu_0}\left(B_r^2 - B_t^2\right) \tag{3.73}$$

The radial component of the force density f_r can be written as the contributions of the radial components of the flux density f_{rr} minus the contributions from the tangential flux density components f_{rt}, see (3.74).

$$f_r = f_{rr} - f_{rt} = \left(\frac{1}{2\mu_0} B_r^2\right) - \left(\frac{1}{2\mu_0} B_t^2\right) \tag{3.74}$$

The lowest mode of vibration is equal to the GCD of Q_s and $2p$, which is two in the generators considered in this chapter [81].

The second order radial force component is produced by pairs of flux density harmonics whose harmonic order differs by two (order i and j that gives $i - j = 2$). How these pairs interact to produce the second order radial force component is investigated in the following paragraphs.

The second order harmonic radial force component that is caused by the radial flux density components f_{rr} can be expressed with (3.75).

$$f_{rr}(2^{nd}) = \frac{1}{2\mu_0} \left[\frac{1}{2} B_{r1}^2 + \sum_{k=1,2,3}^{\infty} B_{rk} \cdot B_{r(k+2)}\right] cos(2\theta) \tag{3.75}$$

where k is the spatial harmonic order and B_{rk} is the airgap flux density component of harmonic order k.

3.4 Optimization model

3.4.1 Problem formulation

There is a long list of optimization methods of linear and nonlinear programming, indirect and direct, with constraints, deterministic, stochastic and evolutionary methods that have been used for the design of electrical machines [32]. Genetic algorithms (GAs) are one of these evolutionary strategies that have been popular in the design of electrical machines. As the author of this work has previously used GAs for machine design in [35], it was decided to continue using GAs in this work.

GAs are population-based, evolutionary algorithms which follow the principles of reproduction, natural selection, and diversity. GAs are one of the most used families of stochastic optimization methods in electrical machine design. When using GAs, while finding the global optimum can never be entirely ensured, it is possible to get reasonably close to it. More details on the implementation of GAs as they are used in this thesis are given in [35] where a hybrid version of a GA was used. In the hybrid version, a gradient optimization method was used as a final stage after the GA had found the optimal area of the solution space. Here, the gradient step is not included in the design process. A flowchart illustrating the

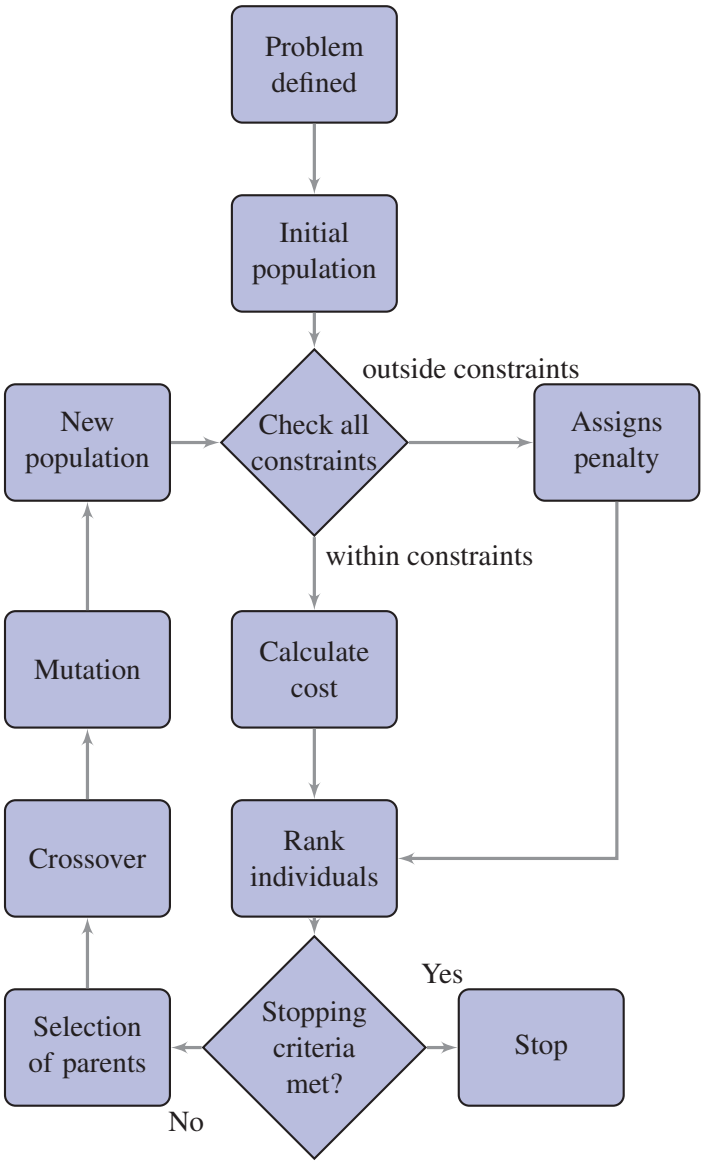

Figure 3.15: Flowchart for the optimization procedure [98].

optimization procedure is presented in Fig. 3.15.

Variables used in the optimization together with upper and lower bounds are given in Table 3.3. The bounds on each variable are set to give a design space that is sufficiently large while at the same time providing reasonable values. The geometric variables are visualized in Fig. 3.16.

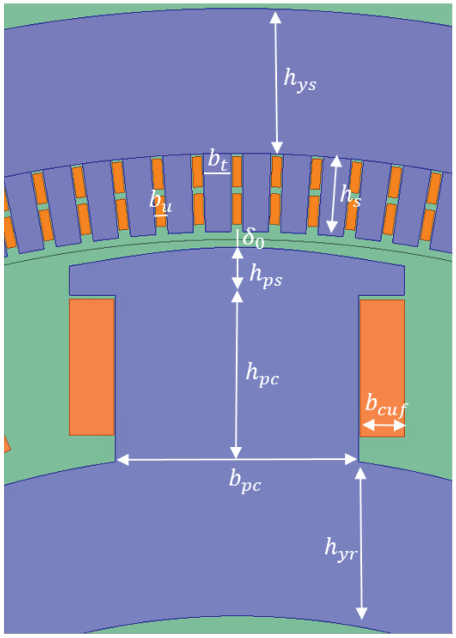

Figure 3.16: Geometric variables

3.4.2 Objective function

In order to optimize both production cost and efficiency at the same time, without using multiple objective functions, the cost of the generator is chosen as the objective function. In the cost function, C_{tot}, see (3.76), both material costs and the net present value of the cost of losses are included. Cost of losses is divided into load dependent losses, P_{ld}, and constant losses, P_{cons}. The constant losses are assumed to be iron losses, mechanical losses, exciter losses and rotor copper losses at no-load. Load dependent losses are assumed to be stator copper losses, rotor copper losses at load and additional losses.

$$\begin{aligned} C_{tot} =& C_{ld} \cdot P_{ld} + C_{cons} \cdot P_{cons} + C_{steel} \cdot m_{iron,rotor} \\ &+ C_{lam} \cdot m_{iron,stator} + C_{cu} \cdot (m_{cu,stator} + m_{cu,rotor}) \end{aligned} \tag{3.76}$$

Table 3.3:
Independent machine variables

		lower	upper
Q_{ss}	Number of stator slots divided by 6	13	65
D	Stator bore (m)	2	7
n_v	Number of cooling ducts	20	60
b_u	Width of stator slot (mm)	10	40
n_{str}	Number of strands per stator slot	20	120
b_{pc}	Pole core width (mm)	200	900
n_f	Number of turns per pole	30	200
b_{cuf}	Width of field winding (mm)	50	300
δ_0	Airgap length (mm)	0	60
h_{cus}	Height of Roebel bar strand (mm)	1.5	2.5
h_{cuf}	Height of field winding turn (mm)	4.0	5.0
L	Axial length (m)	0.75	5

Prices for the different materials are based on typical values similar to values used in other publications [121]. The unit prices for the active materials that are used are:

- stator iron C_{lam}: 4 €/kg
- rotor iron C_{steel}: 6 €/kg
- copper C_{cu}: 11 €/kg

For the losses, it is assumed that the generator is not run as a base plant at rated power output all the time. The cost of losses may vary from market to market. In this paper the cost of constant losses is set to 3000 €/kW, while the cost of load dependent losses is set to 2000 €/kW.

3.4.3 Constraints

The main design constraints used in the optimization process are given in Table 3.4.

The synchronous reactance is normally limited to maintain stable operation when the generator is connected to the grid. According to [122], the synchronous react-

Table 3.4:
Parameter constraints

Parameter	Constraint
Synchronous reactance*	$\leq$ 1.2 p.u.
Transient reactance	$\leq$ 0.4 p.u.
Subtransient reactance	$\geq$ 0.15 p.u.
Tooth flux density	$\leq$ 1.7 T
Pole core flux density	$\leq$ 1.6 T
Rotor yoke flux density	$\leq$ 1.3 T
Stator current density	$\leq$ 5 A/mm^2
Rotor current density	$\leq$ 5 A/mm^2
Rotor tip speed at runway speed	$\leq$ 150 m/s
Inertia constant $\frac{T_M}{T_w}$	$\geq$ 4
* - initial value	

ance value of hydrogenerators can normally be found in the range from 0.6 p.u. to 1.5 p.u., the transient reactance from 0.2-0.5 p.u. and the subtransient reactance from 0.15-0.35 p.u.

For the optimization process, typical upper limit values of 1.2 p.u and 0.4 p.u. for the synchronous and transient reactance were selected based on what was recommended in the literature. Additionally, the subtransient reactance is important for limiting the short circuit currents and to prevent failures from spreading to other parts of the power system. A lower limit of 0.15 p.u. was implemented for the subtransient reactance.

The loading of the generator is restricted by the design of the insulation and the cooling of the machine [78]. In order to estimate the temperature rise in the different parts of the generator, a thermal equivalent circuit network is used [90]. If the cooling of the machine is not sufficient, the generator has to be redesigned. The maximum inlet velocity of the cooling air into the stator cooling ducts is set to 16 m/s.

The current density needs to be limited to prevent overheating. Common values range from 3 to 5 A/mm^2 [32]. Based on the available literature, it is reasonable to choose 5 A/mm^2 as the upper limit for the current density in the process of finding the optimal design of the genrator.

The total resistance of the winding is at its minimum when the ratio of AC to DC resistance is 1.33 [78]. If the resistance ratio is substantially higher than this, the generator is expected to experience excessive heating close to the stator winding. For the optimization process it is therefore practical to choose 1.5 as the maximum AC to DC resistance factor of the stator winding.

According to [122] the mechanical starting time, i.e. the time it takes to accelerate the rotor from standstill to rated speed using nominal torque, is given as $T_M = 2 \cdot H$. For large generators connected to the grid, the system operator often specifies restrictions to its moment of inertia. This is to maintain sufficient inertia in the power system, which preserves the system stability. Statnett, the Norwegian system operator states in the Norwegian grid codes for transmission system [123] that the ratio between the time constants for the moment of inertia T_M and the waterway T_w should be more than 4. T_w is usually set to 1s [32].

3.5 Case studies

Table 3.5 presents the main data on the generators that are studied in Chapter 4, 6 and 7.

Table 3.5:
Design specifications

	G1	G2	G3	G4	G5
Power (MVA)	122.6	320	105	105	75 kVA
Power factor	0.9	0.86	0.9	0.9	0.9
Speed (rpm)	120	428.6	428.6	85.7	500
Number of poles	60	14	14	70	12
Number of slots	504	114	180	432	108
Number of slots per pole and phase	$2\ \frac{4}{5}$	$2\ \frac{5}{7}$	$4\ \frac{2}{7}$	$2\ \frac{2}{35}$	3
Stator outer diameter (m)	11.3	5.39	4.47	12.4	0.876
Airgap diameter (m)	10.6	4.4	3.7	12	0.725
Machine length (m)	1.626	3.6	1.8	0.96	0.303

Generators G1, G2, G3, and G4 are all large hydropower generators with power ratings above 100 MVA, which is the power range of the largest converter-fed synchronous hydropower generator that has been installed. G1, G3 and G4 were selected to represent generators with different rotational speeds, pole numbers and designs at this power level. G2 was selected to represent a high-speed generator at one of the higher power ratings available for hydropower.

Generators G2 and G3 were chosen for several reasons. First, detailed design data and specifications were available. This made them suitable for loss analysis and finite element simulations. Second, they are both 428.6 rpm generators with the same lowest order flux density and radial force density harmonics. With different numbers of slots per pole and phase, this made them suitable for analysis in Chapter 6 on radial forces.

G1 in Table 3.5 is a 504-slot, 60 pole, 60 Hz generator that is used in several publications, e.g. [38, 53]. This generator is chosen as a case to study the core losses in Chapter 4 due to the fact that the available, published data contains measured losses, simulated losses, geometric and material data. This makes G1 a suitable case for comparison of different core loss models.

In Chapter 6, generators G2, G3 and G4 are analyzed. These three generators were chosen to have both low-speed and high-speed generators, and machines with both a high and a lower number of slots per pole and phase. G2, G3 and G4 all have the same lowest order radial force components. Simulations are made using both stationary and time-stepping finite element simulations.

G5 is a generator test setup [124] that is used to perform different loss measurements that are discussed in Chapter 4. G5 is the generator test setup at the electrical machines lab at Uppsala University. It is one of the only test setups available at universities to perform measurements for hydropower research. The author of this work visited Uppsala University to perform loss measurements and to verify the finite element simulations that are presented in Chapter 4 and 6.

G1 and G2 are used in Chapter 4 to compare different methods for estimating the core losses.

G3 is used to investigate the additional losses in the stator core, stator winding and damper winding that are produced during converter operation in Chapter 5.

In Chapter 7, generator G3 is used as the basis for finding the optimal design. During the design process, the generator is used to optimize the design for different rotational speeds and number of poles to find the optimal rated frequency. Generator G3 is also used to investigate what happens to the total cost of the machine when the requirement on the synchronous reactance is relaxed.

Chapter 4

Loss analysis - modeling, analysis and validation measurements

A framework for numerical modeling and analysis of different losses in hydrogenerators is presented in this chapter. Finite element simulations and loss predictions are compared to experimental results from a synchronous generator test setup. Different core loss models are presented and compared to loss data from large hydrogenerators and the generator test setup. The use of core loss correction factors is investigated in order to find out which values are optimal for use.

4.1 Finite element simulations

In this chapter, finite element simulations with the Ansys Maxwell finite element simulation software are used to study flux densities, voltages, currents and core losses in the generator. Finite element simulation software is also used to model the behavior of the generator in converter operation. All simulations are made using 2D models where the stack length in the axial direction is given as an input parameter. An example of a simulation showing flux lines and flux density distribution is given in Fig. 4.1. For this chapter, time-stepping finite element simulations are used.

Rotor and stator magnetic behavior are modeled using nonlinear curves for the relationship between flux density **B** and magnetic field intensity **H** using data from a manufacturer of laminated steel. Both rotor and stator core material are assumed to be isotropic. In addition, the magnetic vector potential is considered to be zero along the outer border of the stator yoke and along the inner border of the rotor ring.

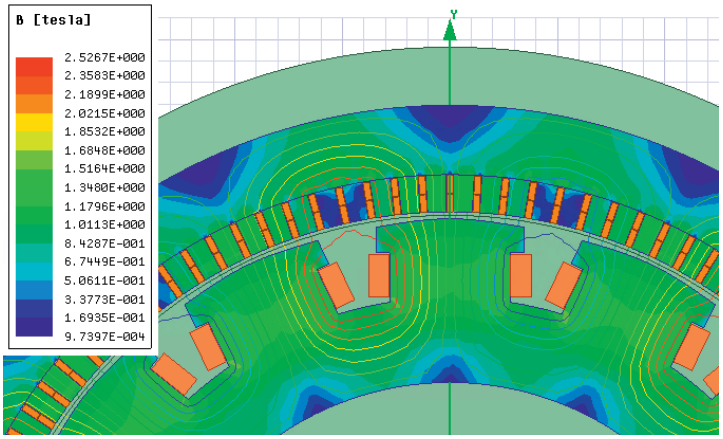

Figure 4.1: Plot of flux lines and flux density distribution in a hydropower generator.

Furthermore, external circuits are used to load the output terminals of the generator, and to model the 3D effect of damperbars on the finite element simulation of the generator, see Fig. 4.2. The external load circuit is modeled with the given phase resistance of the stator winding $\mathrm{R_{Phase}}$ and a load impedance that consists of a load resistance $\mathrm{R_{Load}}$ and a load inductance $\mathrm{L_{Load}}$. If the generator were to have a capacitive load, the load inductance can be replaced by a load capacitance. In the damperbar circuit, $\mathrm{R_{Interbar}}$ denotes the resistance of the end rings between each damperbar and $\mathrm{R_{Interpole}}$ the resistance of the end rings between each pole.

In order to investigate the effects of converter operation on copper and iron losses, two converter topologies are used. The converters have been implemented by one of my colleagues at the Department of Electric Power Engineering at the Norwegian University of Science and Technology (NTNU), using an external circuit representation [42]. Only the machine-side converters are modeled. The converters are modeled as connected to a DC-source that represents the DC-link capacitor, which is connected to the grid-side converter [42].

First, a two-level voltage source converter (VSC), and then a three-level neutral-point-clamped (NPC) topology with specifications given in Table 4.1 are used. As stated in [42], due to computational issues, the frequency converters are modeled as simply as possible. Frequency converters are therefore modeled with ideal switches and sinusoidal pulse-width modulation (PWM). Four carrier frequencies are simulated.

First a 450 Hz case is simulated. Then 1050 Hz, 2100 Hz and 10500 Hz are

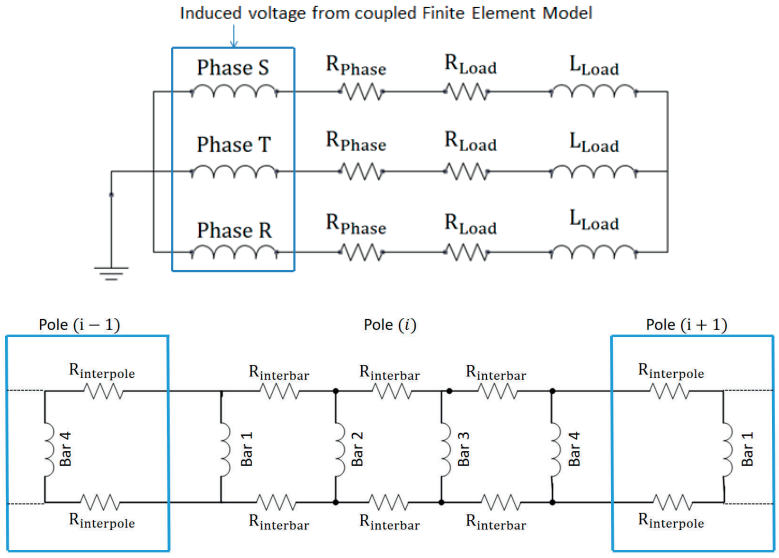

Figure 4.2: External circuits: for modeling load (top) and damperbar circuit for one pole. Generic damper winding configuration for illustration only.

used to investigate the effect of possible developments in semiconductor devices. Converter operation is simulated using generator G1 in Table 3.5 using the same converter circuits that were used for [42] to investigate possible vibration problems during converter operation. The power electronic circuit is illustrated in Fig. 4.3. In order to include the effect of converter switching, a sufficiently small time step of 10 microseconds was used. The converters are modeled with ideal, lossless switches and sinusoidal pulse width modulation due to computational considerations.

Table 4.1:
Converter specifications

Converter	Configuration	2-level, 3-level NPC
	Switches	Ideal
	Type of pulse-width modulation	Sinusoidal
	Carrier frequency	450 Hz, 1050 Hz 2100 Hz, 10500 Hz

There are several challenges to the numerical modeling of hydrogenerators. Para-

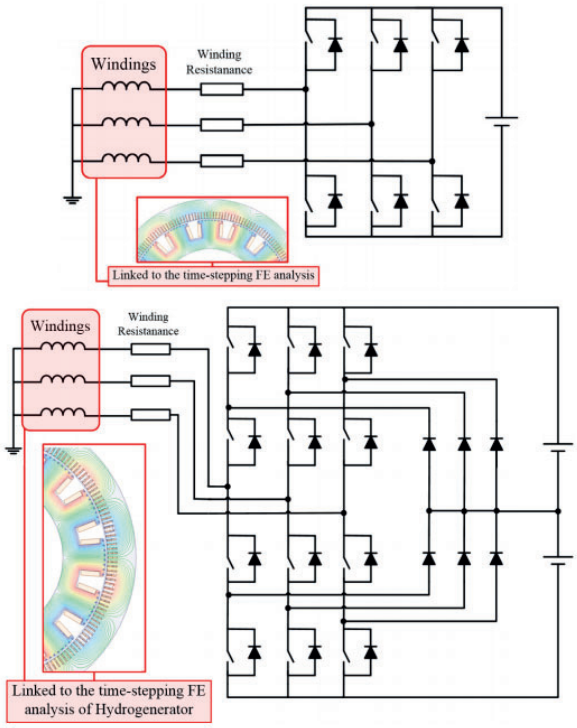

Figure 4.3: Coupled converter circuit models used in finite element simulations. two-level VSC (top) and three-level NPC topologies, illustration from [42].

meters such as stack length, effective airgap and the magnetic BH-curve used in the design data from manufacturer can deviate substantially from the actual values. In [125] the sensitivity to these three parameters was compared to measured data from open-circuit, short-circuit and heat run tests for four different generators with the same design data. It was found that the effective airgap for one of the generators was 20% smaller than the design airgap and that the effective airgaps can deviate up to 30% from the design value [125]. Model parameters should be tuned to measurements to ensure a more accurate model. In order to check the accuracy of the finite element simulations, a series of tests was performed on a synchronous generator test setup described in [124].

4.2 Measurements and comparison with simulations

The generator test setup presented in 4.4 and 4.5 is driven by a 75 kW induction motor drive. The output torque from the motor drive is used to calculate the input power when the mechanical losses and the core losses are estimated. By changing

the speed of rotation, the mechanical losses can be measured if the generator is run with open stator winding circuits and no excitation current. The friction and windage losses are measured together with the losses in the gearbox since only the total input power P_{input} is measured. P_{input} is given by (4.1). where T is torque in Nm and ω is rotational speed in rad/s. Furthermore, the gearbox losses are considered load independent and only dependent on the speed of rotation.

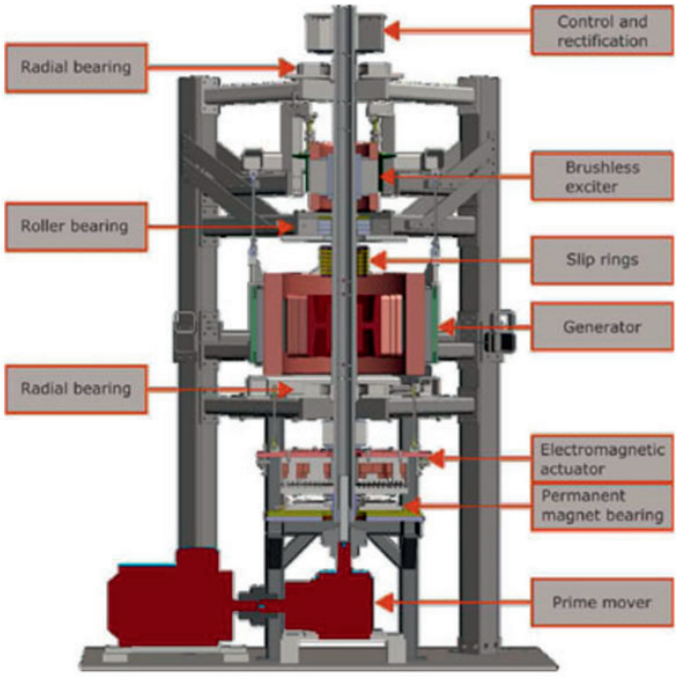

Figure 4.4: CAD drawing of experimental setup from [88].

$$P_{input} = T \cdot \omega \tag{4.1}$$

According to the IEC 60034 [51] standard, the iron losses and mechanical losses are considered constant losses for each rotational speed. Iron losses P_{iron} are therefore measured using the no-load test where they are found by subtracting the mechanical losses P_{mech} from the total input losses, see (4.2).

$$P_{input} = P_{iron} + P_{mech} \tag{4.2}$$

The rated line voltage of the test setup generator G5 in Table 3.5 is 156 V and

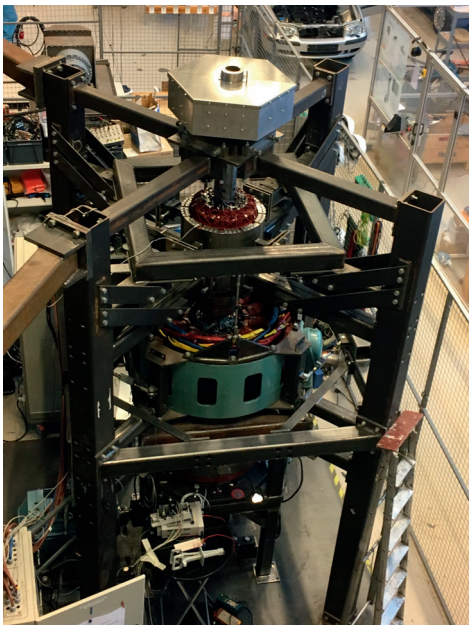

Figure 4.5: Generator test setup at Uppsala University, private photo.

the rated current is 278 A. G5 has a design airgap length of 8.4 mm. Rated field current at no-load is 12.4 A and at full load the rated field current is 20.8 A.

The experimental test setup is shown in Fig. 4.6. The prime mover is modeled by an induction motor that is driven by a ABB ASC800 frequency converter with a speed accuracy of 0.1-0.5% and connected to the generator via a gearbox. The output torque is estimated with a linearity accuracy of $\pm 4\%$ and a repeatability accuracy of $\pm 3\%$. Output power is calculated using the output torque, given as a percentage of nominal output torque. The nominal output torque is found based on the speed and power ratings of the induction motor that is driven by the frequency converter. In this case the rated power is 74.9 kW at 2130 rpm (223 rad/s), giving a torque reference of 336 Nm.

The output torque from the converter used in the measurements is given in discretized steps of 0.01% of rated torque at 500 rpm. This corresponds to an accuracy of the measured output power of ± 7.49 W. The speed accuracy of the frequency is given as $\pm$0.1-0.5%, which given that the given output torque is accurate, result in an output power that can have an accuracy error of $\pm$7.5-7.53 W at 500 rpm.

Direct temperature measurements on the drive system, in particular on the gearbox whose losses change with temperature, would have improved the accuracy of the

measurements. Direct temperature measurements were not available during the time the measurements were performed. In order to minimize the impact of temperature on the measured data, the generator was driven without excitation until the measured input power needed to cover the mechanical losses stabilized. This process took approximately one hour.

Ideally, the measurements should have been performed with the gearbox and machine temperatures being logged. In addition, the torque and speed should have been measured directly at the shaft between the gearbox and the generator, in order to avoid any uncertainty regarding the efficiency of the gearbox. The speed and torque should have been measured with equipment that have lower accuracy errors than 0.1%. Such equipment was not available at the time the measurements were performed.

In addition, the stator core material used in the stator of the generator is not known. Therefore, material data from the manufacturer was not available. The solution was to use available data from Cogent, one manufacturer of laminated steel for electrical machines. The steel quality that was found to fit best with the measured data was M530-50A. Not knowing the exact type of laminated steel used in the generator is one additional source of accuracy error in the measurements.

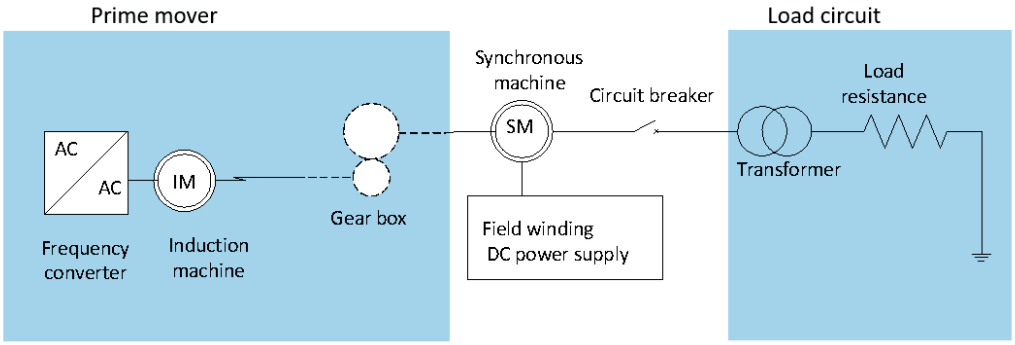

Figure 4.6: Experimental setup.

Stator phase voltages and stator phase currents were measured using sensors with voltage outputs. LabVIEW was used to collect the measured signals using data acquisition equipment from National Instruments. All signals were recorded with a 10 kHz sampling frequency for 1 second. The field current was controlled by a EA-PS 8160-170 10000W DC power supply, and it was read directly from the output display of the DC supply.

Airgap flux density was measured with a Hall-effect sensor mounted on the surface

of one of the stator teeth and recorded using LabVIEW, see Fig. 4.7. This was performed for different operation points, both in no-load and loaded with a 3.5Ω per phase resistance.

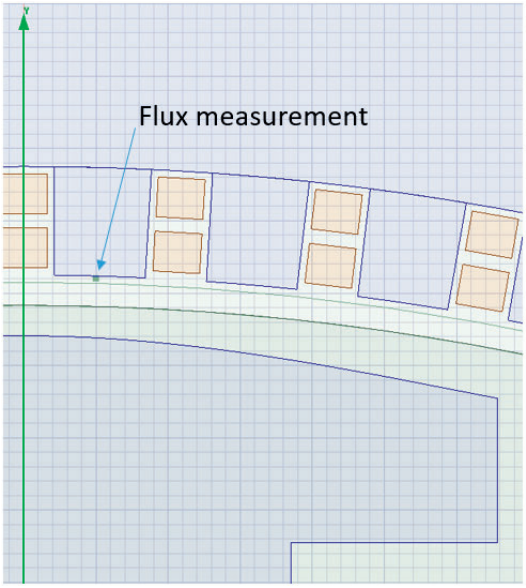

Figure 4.7: Model drawing of generator test setup showing placement of Hall-effect sensor for flux density measurement.

According to IEC60034 standard [51] mechanical losses and iron core losses are considered constant losses. These are measured during the no-load test. In the same way, iron losses are estimated using finite element simulations at no-load. When calculating the iron core losses in the stator P_{iron}, it is useful to calculate losses in the yoke and teeth separately, see (4.3) .

$$P_{iron} = k_1 P_{yoke} + k_2 P_{teeth} \tag{4.3}$$

k_1 is the correction factor for the stator yoke and k_2 is the correction factor for the teeth losses. These correction factors are used to correct for rotational field loss, losses due to machining of the laminations, harmonic losses and different effects that make the calculated losses P_{yoke} and P_{teeth} deviate from the measured losses.

There are various methods for estimating the iron losses, some of which are explained in the following section.

4.2.1 Rotational fields and associated core loss components

Classical methods for estimating core losses are based on the assumption that the field in the stator core is purely pulsating. This assumption does not usually hold, and therefore different correction factors based on empirical knowledge are used.

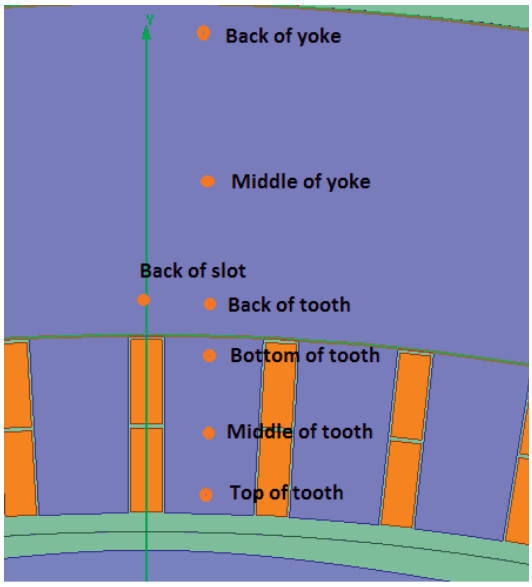

Figure 4.8: Stator geometry

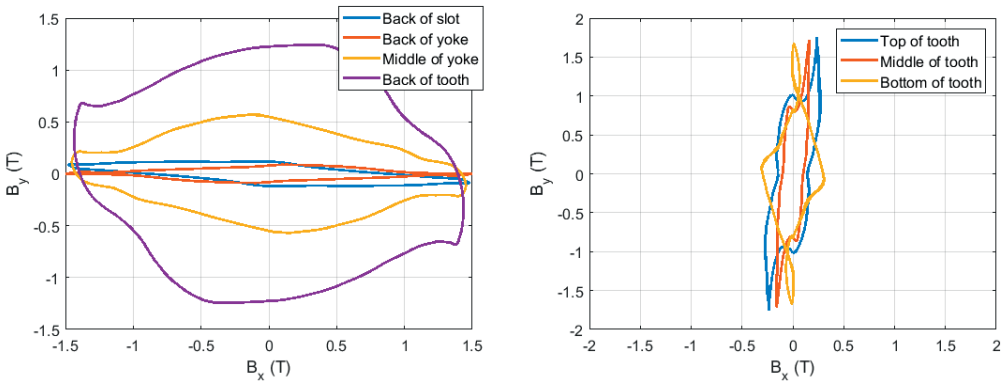

Figure 4.9: Rotational field plot for the 320 MVA, q = 2 $\frac{5}{7}$ generator at full-load operation in the yoke (left) and in the teeth.

The x- and y- component of the B-field in the yoke of the stator of generator G2 in Table 3.5, is presented in the upper part of Fig. 4.9. It can be observed that

the degree of rotation in the field varies in different parts of the yoke. At the back of the slot the field can be considered pulsating with the y-component of the field dominating. In the back of the tooth, see Fig. 4.8, the field is rotational with the two components of the field having similar amplitudes. The field in the middle of the yoke is less rotational with the maximum amplitude in the y-direction being about one third of the maximum amplitude in the x-direction. At the back of the yoke the field is pulsating in a similar manner to the back of the slot.

The field is plotted at full-load for the teeth at three different positions: close to the airgap, close to the yoke and in the middle of the teeth in Fig. 4.9. It can be observed that even though the field has a degree of rotation, it is not to the same extent as in the yoke. It seems that the assumption of the field being pulsating can be considered valid in the teeth.

4.2.2 Flux density and stator no-load voltage measurements

In order to compare measured and simulated no-load core loss, it is important to be sure that the induced voltage is the same in both simulations and measurements. Fig. 4.10 shows the measured no-load voltage at 500 rpm. It can be noted that the measured induced phase voltage is higher than the simulated voltage using the design data for the experimental test setup.

According to [125], the effective value of several of parameters of the generator can deviate from the design values. In particular, the stack length, the effective airgap length and the BH-curve can be different from that which is calculated in the design phase.

Changing the BH-curve did not change the simulations to any great extent in this case. By reducing the airgap length to 89% of the design value, the induced voltage from simulations was brought to correspond well with the measured value. The same results could be achieved by increasing the axial length of the generator test setup in the simulations. Thus changing the axial length the same percentage would mean adding approximately 36 mm, while the change in the airgap length is only approximately one mm.

For the simulations for the no-load case, all values are retrieved from simulations with the reduced airgap length. In Fig. 4.10 the induced phase voltage from simulations at different rotational speeds are compared to measurements. It can be seen that with parameter adjustments, the simulated no-load voltages fit well with measurements for all rotational speeds.

Fig. 4.11 presents the comparison of the measured and simulated airgap flux density for the generator test setup. Both the loaded case and the no-load case are

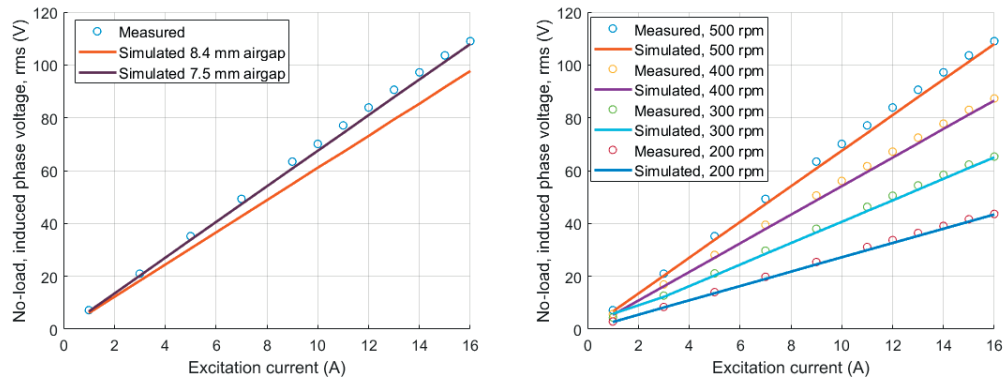

Figure 4.10: Measured and simulated induced phase voltage at no-load at 500 rpm using design airgap and modified airgap (left) and at different rotational speeds.

presented with a 9 A excitation current. Simulations show satisfying agreement with measurements in both the loaded and the no-load case. For the loaded case, the design airgap length was used. In no-load, the adjusted airgap was used.

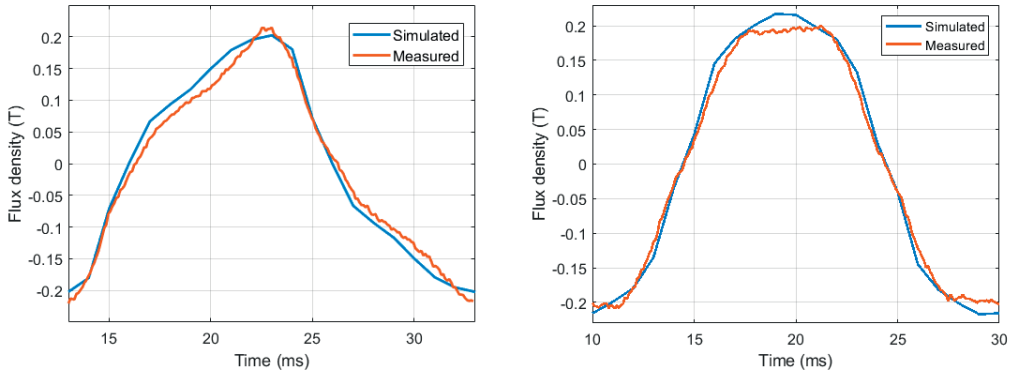

Figure 4.11: Radial flux density on the surface of stator teeth at 500 rpm operation, measured using Hall-effect sensor. With 9 A excitation current loaded with 3.5Ω per phase (left) and no-load at 9 A excitation current.

4.2.3 No-load loss measurements

Experimental results are compared to simulations for the generator test setup G5 presented in Table 3.5. The losses were measured by recording the input power from the frequency converter to the prime mover.

The first test was conducted in order to measure the mechanical losses from fric-

tion, ventilation and the gearbox. Mechanical losses were measured by running the test generator at different rotational speeds without excitation current.

Mechanical losses can be considered constant according to the IEC 60034 standard. The efficiency of the gearbox is not dependent on load, only on rotational speed. The measured mechanical losses are subtracted from the input power to estimate the iron core losses during the no-load loss test.

The measured mechanical losses are presented in Fig. 4.12 and compared to the analytical estimate for the mechanical losses given by (3.40). It was found that the analytical formula for the mechanical losses underestimated the losses of the generator test setup. The sum of squared errors (SSE) is presented in Table 4.2.

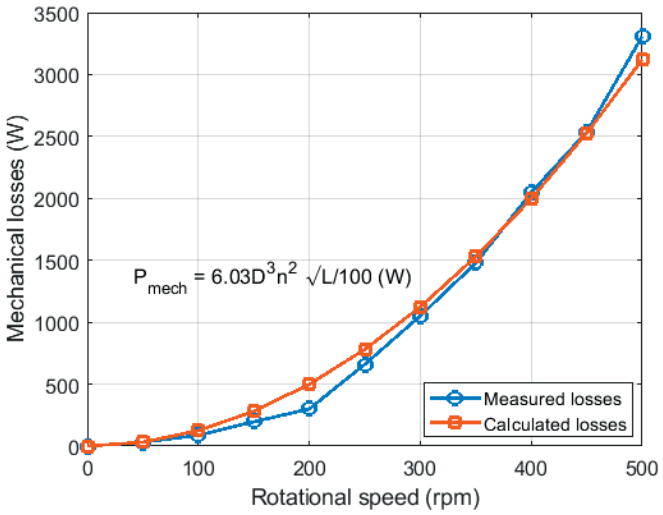

Figure 4.12: Measured mechanical losses compared to analytical loss estimates.

Using the loss coefficient given in (3.40) gives a large value for the SSE. Therefore a new value for the loss coefficient was found by minimizing the SSE, yielding a loss coefficient of 6.03. If the SSE at only rated rotational speed is to be minimized, the value of the loss coefficient would become 6.31. Using the coefficient that minimizes the SSE gives an estimation of the mechanical losses that fits well with the measured losses. One of the reasons that can partially explain why the original loss coefficient did not estimate the losses in the test setup well is that the gearbox losses are included in the measurement. The equation is originally made for cases without gearbox losses. Another reason is that the loss coefficient is based on measurements on large hydropower generators. The scalability of the equation does seem to be inaccurate without modification of the loss coefficient.

Table 4.2:
Sum of squared error for analytical estimation
of mechanical losses for generator test setup

Original loss coefficient:	12 850 483 W^2
Optimized loss coefficient:	104 519 W^2

Core loss measurements at 500 rpm and 400 rpm are compared to measurements in Fig. 4.13, where the Bertotti loss separation approach is used, see (3.46), (3.48), and (3.49). At 500 rpm, simulations give accurate results at most levels of excitation current. Different correction factors are used for the yoke losses.

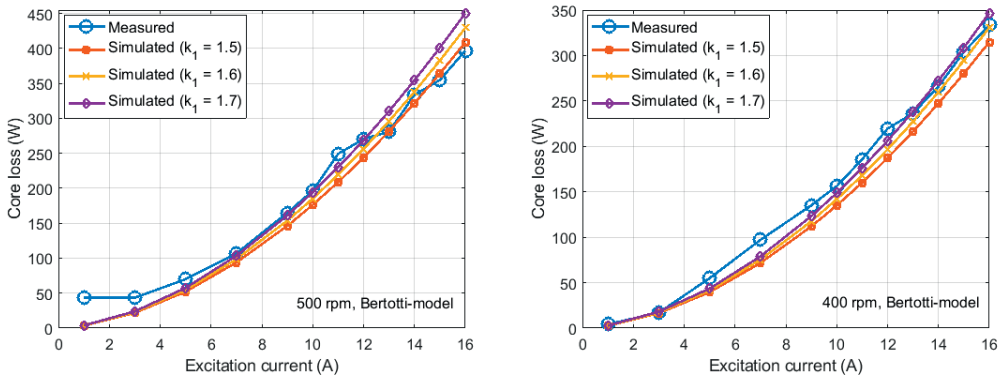

Figure 4.13: Comparison between measured and estimated stator core loss for the generator test setup. Different correction factors are used in the core loss estimations. Measurements and simulations at 500 rpm (left) and 400 rpm.

The results have not been found to be conclusive regarding which value should be used. The SSE is used to quantify how well the core loss prediction from simulations fits with the measured data. It is presented in Table 4.3 that overall, using a yoke correction factor of 1.6 gives the best loss estimate at 500 rpm as the SSE is 5% lower than the SSE that can be obtained using a correction factor of 1.5 and 34.7% lower than when 1.7 is used as the correction factor for the yoke.

At high levels of excitation during operation at 500 rpm, i.e. 14-16 A, using a yoke correction factor of 1.5 gives the lowest SSE, with only 20% of the $k_1 = 1.6$ SSE and 7% of the $k_1 = 1.7$ SSE. Between 7 and 13 A, a yoke correction factor of 1.7 seems to give the lowest prediction error according to Table 4.3, with the SSE being 77% of the SSE for $k_1 = 1.6$ and 38.6% of the SSE for $k_1 = 1.5$.

Table 4.3:
Sum of squared error for core loss prediction on generator test setup

	500 rpm:			400 rpm:		
	$k_1 = 1.5$	$k_1 = 1.6$	$k_1 = 1.7$	$k_1 = 1.5$	$k_1 = 1.6$	$k_1 = 1.7$
Total :	6036.6	5730	8774.6	5262.7	2230.2	1171.4
1 - 6 A :	2390.3	2242.1	2110.5	238.3	180.1	131.3
7 - 13 A :	3276.6	1641.5	1263.8	3757.2	1912.4	804.6
14 - 16 A :	369.8	1846.3	5400.3	1267.2	137.7	235.5

Results from SSE analysis is given in W^2.

Below 7 A the core loss prediction of the Bertotti method does not match the measured losses well, but the error is smallest when using a correction factor of 1.7. The measured losses are higher than the predicted losses and not reduced in the same way as with a reduced excitation current. One reason for the higher measured losses at low excitation currents may be that it is a more complex task to separate the core losses from the mechanical losses. It is difficult to separate core losses of a few W from mechanical losses of several kW, see Fig. 4.12. Therefore, the real core losses may be lower and closer to the predicted losses than those that have been measured.

Measured and simulated core loss at 400 rpm is also presented in Fig. 4.13. It can be seen that the measured and simulated losses are in agreement. According to Table 4.3 the SSE of the worst fitting yoke correction factor, i.e. $k_1 = 1.5$ for 400 rpm, is 8.2% lower than the best fitting choice of yoke correction factor for 500 rpm. Overall, for 400 rpm, using $k_1 = 1.6$ instead of $k_1 = 1.5$ lowers the SSE to 42.4% of its previous value. Using $k_1 = 1.7$ reduces the SSE by an additional 47.5%, indicating that the yoke correction factor that gives the best loss prediction is 1.7 at this rotational speed.

Measured losses are higher than the simulated loss at 5-7 A excitation current, while the lowest levels of excitation current corresponds well with measurements. For an excitation current between 14 A and 16 A, using $k_1 = 1.6$ gives a SSE that is 41.5% lower than when $k_1 = 1.7$ is used. For all other levels of excitation current, using $k_1 = 1.7$ gives the best results.

In Fig. 4.14 the measured losses at 500 rpm are compared to both the Bertotti method and the Vector-Preisach approach, using (3.50) and (3.48). It can be stated that both methods are able to provide reasonable results. The analysis suggests that the Bertotti model gives a better core loss prediction at all levels of excitation. The more detailed Vector-Preisach model does not predict the core loss as well as

the Bertotti method.

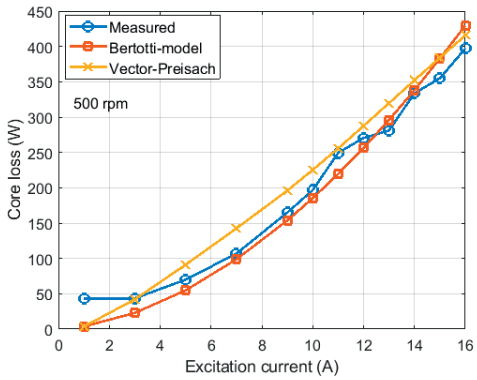

Figure 4.14: Comparison of different methods for estimating the core loss in generator test setup at 500 rpm.

Losses were also measured for 300 rpm and 200 rpm. Measurements are compared to simulations with the Bertotti approach in Fig. 4.15. Using $k_1 = 1.7$ gives the smallest SSE for both 300 rpm and 200 rpm, see Table 4.4.

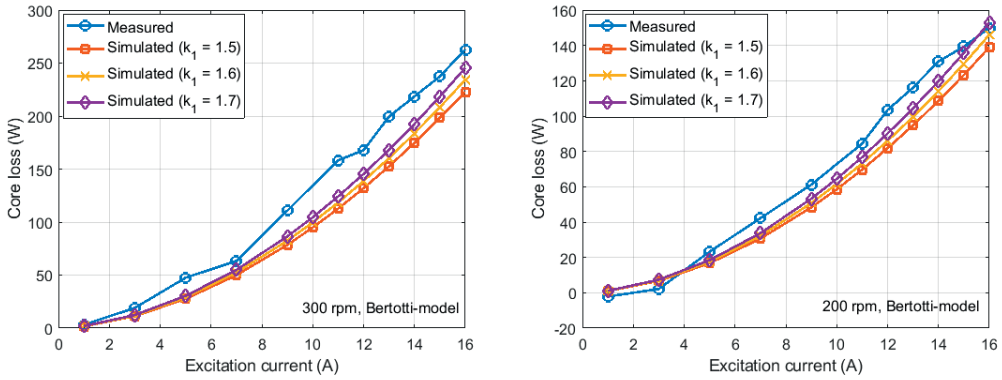

Figure 4.15: Comparison between measured and estimated stator core loss for the generator test setup. Different correction factors are used in the core loss estimations. Measurements and simulation at 300 rpm (left) and 200 rpm.

For 300 rpm the best fitting yoke correction factor offers the second highest SSE of all the measured rotational speeds. With an SSE of 4988.5, it is only smaller than the best case SSE for 500 rpm at 5730. At low levels of excitation, i.e. 1-6 A, the simulated losses fit the measured losses better. Measured losses are, in general, higher than simulated losses for both 300 rpm and 200 rpm. This may be due to

Table 4.4:
Sum of squared error for core loss prediction on generator test setup

	300 rpm:			200 rpm:		
	$k_1 = 1.5$	$k_1 = 1.6$	$k_1 = 1.7$	$k_1 = 1.5$	$k_1 = 1.6$	$k_1 = 1.7$
Total:	12288.1	8167	4988.5	2382.3	1386.4	717.3
1 - 6 A:	459.6	397	339	72.7	66	61
7 - 13 A:	6787.3	4890.5	3314.7	1438.9	912.3	508.3
14 - 16 A:	5041.2	2879.4	1334.9	870.6	390.1	148.1

Results from SSE analysis is given in W^2.

some inaccuracy in the measurements. It may also be due to the fact that the loss data used in the model are given for 50 Hz operation, while 300 rpm gives 30 Hz operation for this machine.

The core loss prediction from simulations fit better with measurements at 200 rpm than at 300 rpm. Simulations predict lower losses than those measured. The difference between measured and predicted losses is smaller for 200 rpm than for 300 rpm. Overall, predicted losses with the Bertotti method are close to the measured losses at all rotational speeds and excitation currents. It is not conclusive which correction factor gives the best prediction. The best correction factor value changes from case to case. It is also likely that better measurement equipment with better accuracy would yield better results.

In Fig. 4.13, the measured core losses at 1-2A excitation current, 500 rpm, are substantial. This is not the case for the core losses measured at other rotational speeds. Part of the explanation might be the accuracy of the measurements.

At 500 rpm, the mechanical losses are larger than for the other rotational speeds. Mechanical losses seem to increase with the square of the rotational speed. The mechanical losses are multiple times larger than the core losses. It can therefore be difficult to separate the core losses from the mechanical losses accurately at low excitation currents.

In addition, the gearbox losses might not be perfectly constant. Oscillations in the mechanical losses can be part of the explanation for why the core losses appear to be substantial at 1-2 A, 500 rpm. In conclusion, core losses at 1-2 A excitation current and 500 rpm are likely to be smaller than the measurements indicate.

4.2.4 Load loss measurements

Load tests were performed on the test setup with a resistive load. The test setup generator was loaded using a 3.5 Ω per phase load-resistor connected via a transformer with a turns ratio of 156:400, as presented in Fig. 4.6. The measured load current and phase voltage is compared to simulations in Fig. 4.16.

It can be seen that a accurate fit between measured and simulated voltage and current in loaded operation is achieved after some tuning of the model. Using the design airgap length of 8.4 mm gives agreement between simulations and measurements in loaded operation. Due to thermal limitations it was not possible to run the test setup with load with an excitation current above 9 A.

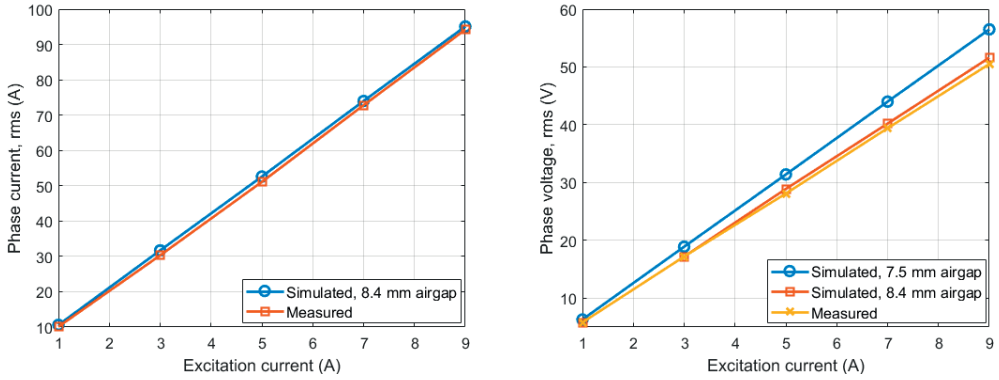

Figure 4.16: Comparison between measurements and simulations during load at 500 rpm. Load current (left) and induced phase voltage during load.

Output power was calculated using LabVIEW where the power factor was calculated. Total losses in the test setup generator at load are measured by subtracting the output power from the input power. The difference between the output power from LabVIEW and the measured input power is compared to the estimated total losses in Fig. 4.17 and Table 4.5. The estimated total losses consist of mechanical losses, iron core losses and stator copper losses.

Results based on previous measurements on the test setup generator presented in [88] and [126] have found the stator winding DC resistance to be 20.1178 mΩ. Copper losses are calculated from the measured stator current using the given DC resistance value.

The AC-to-DC ratio of the winding resistance was found using (3.68) and (3.69) to be 1.076, meaning that the AC copper losses are 7.6% of the DC copper losses. The AC copper losses for a field current of 9 A are presented in Table 4.5. The

total copper losses are the sum of the DC and AC losses, i.e. 1.076 times the DC copper losses.

Table 4.5:
Comparison of measured and estimated total losses at 9A excitation current

	Measured:	Calculated:
Mechanical losses (W):	3309.1	3309.1
Core losses (W):	164.9	161.1
Copper losses, DC (W):	535.6*	545.8
Copper losses, AC (W):	40.7*	41.5
Total losses (W):	4056.1	4057.5

*Estimated based on measured current

The pole surface losses of the test setup generator were estimated using (3.57), (3.58) and (3.60) presented in Section 3.2.4. In no-load the surface losses were estimated at 1.3 W at 500 rpm, and the corresponding full-load losses were estimated to 3.4 W. Compared to the other losses, these losses are considered small and hard to separate. It is assumed that the surface losses are included in the no-load core loss measurement and in the total loss measurement at load.

The estimated losses in Fig. 4.17 seem to correspond well with the measured difference between input and output active power. The sum of calculated losses at the lowest levels of excitation current was found to be unable to predict all the losses measured using the input-output method. Overall, the results from finite element simulations give satisfying results compared to measurements when the expected parameter-tuning is taken into account.

It is found that finite element simulations are able to give accurate results when compared to measurements. It is not always sufficient to use design data for the generator, as real parameter values may deviate from those given by the manufacturer. Therefore, it is highly recommended by the author to tune the design values for the generator used in simulations with measured results.

4.3 Core loss methods applied on large generators

Stator core losses have been calculated for two large hydrogenerators. One 122.6 MVA, q = 2 $\frac{2}{35}$ generator and one q = 2 $\frac{5}{7}$ generator with a power rating of 320 MVA have been studied. Different methods for predicting the stator core loss have been compared to given reference values.

Core loss predictions for the 122.6 MVA generator are presented in Fig. 4.18. All three methods give similar core loss estimates to those found in [38]. In [38]

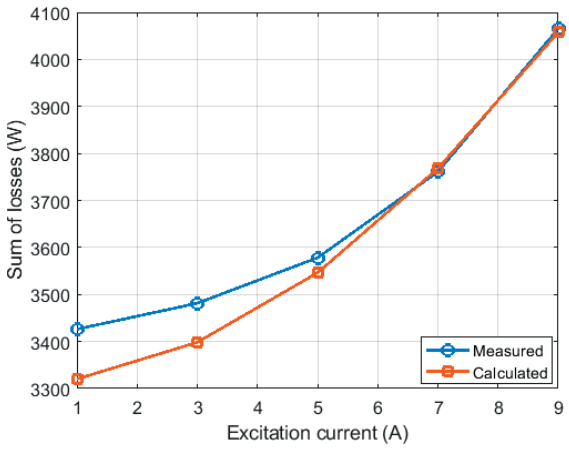

Figure 4.17: Comparison between estimated losses and difference between measured input and output power.

finite element simulations were used together with measurements to find the iron losses in the 122.6 MVA generator. Calorimetric tests were performed according to standard IE/CEI Std. 34-2:1972. Additional information about the accuracy of the measurements are not given in [38].

Losses are calculated with the Bertotti method using (3.46), (3.48), and (3.49), and analytically using (3.54). The Vector-Preisach losses are calculated using (3.50) and (3.48).

Both the Bertotti approach and the more complex Vector-Preisach method were found to give similar results in this generator. It is worth noting that the generator is designed with flux density in the normal range with little saturation. For this particular generator, it is considered most appropriate to use either 1.6 or 1.7 as the correction factor for the simulated losses in the stator yoke.

Fig. 4.19 presents the same comparison for the 320 MVA generator. The reference value for the core losses are the design losses given by the manufacturer. Measurement data are not available for this generator. Therefore, information about the accuracy of the reference losses are not available.

Again, the Bertotti approach is able to give a core loss prediction that is close to the reference value. It seems that the Bertotti model is able to offer accurate core loss estimates for different power ratings and design types, as it provides accurate predictions for all the generators that have been studied here.

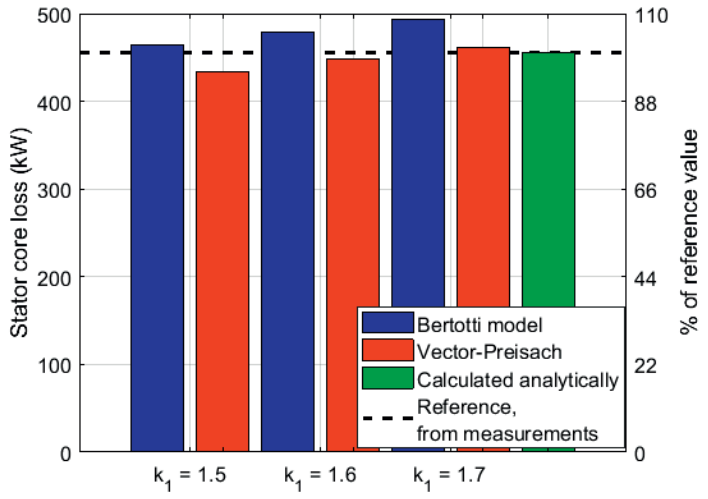

Figure 4.18: Comparison of different methods for estimating the stator core loss of generator G1 a 122.6 MVA, q = 2 $\frac{2}{35}$ generator. Reference value is core losses found from measurements in [38]. k_1 is the correction factor used for the stator yoke loss.

For the 320 MVA generator, see Fig. 4.19, it seems that using a correction factor of 1.5 or 1.6 gives the best results. Based on the results presented, it is not clear what value for the correction factor of the yoke losses should be used. The results indicate that this must be decided on a case-by-case basis where the simulated values are compared to measured loss data.

The Vector-Preisach model seems to be able to predict the core loss without correction factors for the 320 MVA generator, see Fig. 4.19. For the 122.6 MVA generator and the test rig machine the Vector-Preisach model needed the same correction factors in order to provide as accurate loss estimates as the Bertotti approach.

Fig. 4.20 presents how the core losses change with different levels of magnetization for the 320 MVA generator. It can be seen that the core losses estimated using the Vector-Preisach model are higher than the results from the Bertotti model using 1.6 as the yoke correction factor at 100% of no-load magnetization. For 70-90% of no-load magnetization, the core losses estimated using Vector-Preisach are somewhat lower than the results from the Bertotti model. One reason for this is that the Vector-Preisach model can be quite sensitive to saturation due to to the difficulties of modeling the nonlinear magnetization curve.

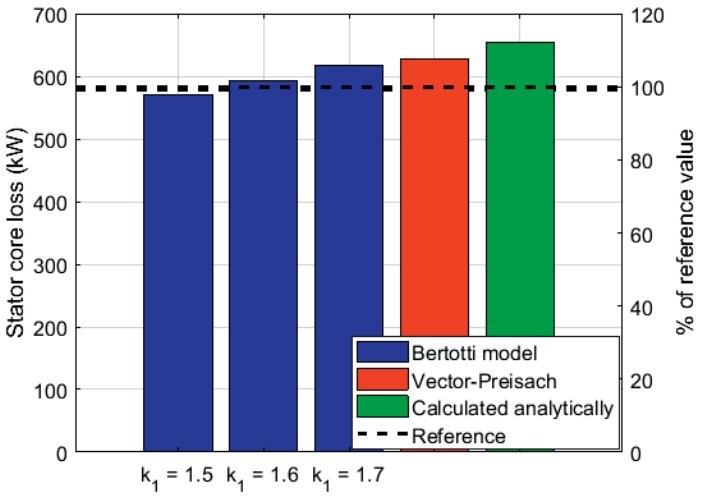

Figure 4.19: Comparison of different methods for estimating the stator core loss of a 320 MVA, q = 2 $\frac{5}{7}$ generator. k_1 is the correction factor used for the stator yoke loss.

The core loss estimation at different magnetization levels are separated into yoke and teeth core loss in Fig. 4.21. For the stator teeth, where the flux density is higher than in the yoke, the core loss is increased drastically when the magnetization is increased from 90% to 100% of the no-load value using the Vector-Preisach approach. This is not the case with the Bertotti model, as it is not as sensitive to saturation as the Vector-Preisach model. Below 90% of no-load magnetization, the Vector-Preisach approach gives lower loss estimates than the Bertotti model for the stator teeth. For the stator yoke, the result is the opposite, see Fig. 4.21. This explains why the total core loss estimates are approximately the same for this generator using both models. Where the Vector-Preisach approach gives a high estimate the Bertotti model gives a lower estimate, and vice versa.

This clearly indicates that the more sophisticated model does not necessarily give better results, and that methods such as the Vector-Preisach should be used with caution. For all the methods it is recommended to calibrate the simulations with real test results in order to be sure that the loss prediction can be trusted.

4.4 Conclusions

A framework for modeling and analysis of losses in large hydrogenerators has been presented. Loss predictions have been compared to experimental results.

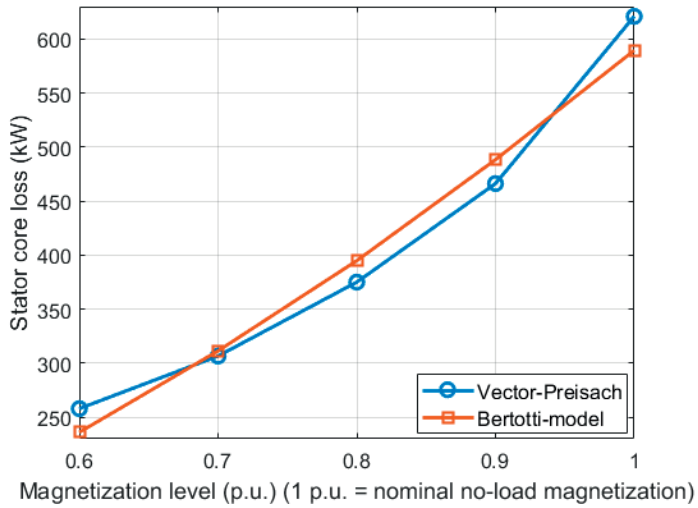

Figure 4.20: Comparison of different methods for estimating the stator core loss of a 320 MVA, q = 2 $\frac{5}{7}$ generator at different levels of magnetization.

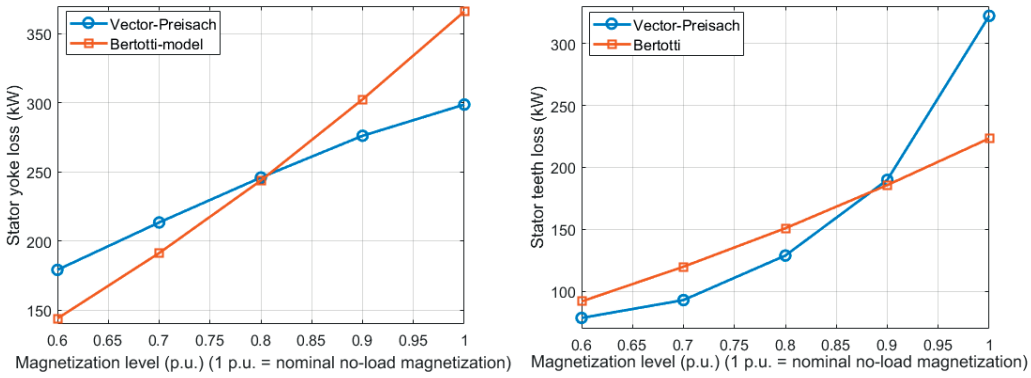

Figure 4.21: Comparison of different methods for estimating the stator core loss of a 320 MVA, q = 2 $\frac{5}{7}$ generator at different levels of magnetization. Yoke core loss (left) and teeth core loss.

It is found that finite element simulations are able to give good results when compared to measurements. It is not always sufficient to use design data for the generator, as real parameter values may deviate from those given by the manufacturer. Therefore it is highly recommended to tune the parameters used in the simulations with measured results.

Different core loss models were compared to measurements on a synchronous generator test setup. Both the traditional Bertotti model based on loss separation and a more detailed Vector-Preisach hysteresis model were used. Different core loss correction factors were applied in order to discover which values should be used optimally.

Overall, predicted losses with the Bertotti method are close to the measured ones at all rotational speeds and excitation currents. It is not conclusive which correction factor gives the best prediction, and it seems that it must be individually decided for each case. The analysis indicates that the Bertotti model gives better core loss prediction at all levels of excitation. The more detailed Vector-Preisach model does not predict the core loss as well as the Bertotti method. It is likely that better measurement equipment with greater accuracy would give better results.

Stator core losses have been calculated for two large hydrogenerators. One 122.6 MVA, q = 2 $\frac{2}{35}$ generator and one q = 2 $\frac{5}{7}$ generator with a power rating of 320 MVA have been studied. Different methods for predicting the stator core losses have been compared.

The Bertotti approach was able to give a core loss prediction that was close to the reference value for both the large hydrogenerators. It seems that the Bertotti model is able to give good core loss estimates for different power ratings and design types, as it provides good predictions for all the generators that have been studied here.

Based on the results presented, it is not clear what value for the correction factor of the yoke losses should be used. The results indicate that this must be decided on a case-by-case basis where the simulated values are compared to measured loss data.

Using the same correction factors as for the Bertotti model, the Vector-Preisach model was able to predict the core losses similarly well in the 122.6 MVA generator. For the 320 MVA generator, the Vector-Preisach model predicted the same core losses as the Bertotti model without using any correction factors. One reason for this may be that the Vector-Preisach model might be sensitive to saturation due to the difficulties of modeling the nonlinear magnetization curve.

The Vector-Preisach model has not been found to improve the core loss prediction significantly, and it has been found to be more sensitive to saturation. This indicates that this more detailed model does not necessarily give better results. Methods such as the Vector-Preisach should be used with much care. For all the methods it is recommended to calibrate the simulations with real test results in order to be sure that the loss prediction can be trusted.

Chapter 5

Additional losses due to converter operation

This chapter investigates the effect of converter operation on AC eddy-current copper losses in the stator and damper windings, and on the losses in the stator iron core of a hydropower generator. Stator currents are computed using finite element simulations. The computed current waveforms are used as an input to estimate the AC copper losses in the stator due to converter operation using an analytical approach. Damperbar losses and iron core losses are calculated directly in the finite element analysis. The generator is simulated with a two-level voltage source converter and a three-level neutral-point-clamped converter topology. Different carrier frequencies are used to investigate their effect on the losses in the generator. Methods for handling these additional losses are discussed and analyzed.

5.1 Effect of converter operation on losses in the generator

This chapter investigates the effect of converter operation on the losses in the generator using a combination of finite element simulations and analytical methods for loss estimation. Generator G3, a 105 MVA, q = 4 $\frac{2}{7}$ generator is used in the analysis. Some of the questions that this chapter will investigate are:

- What is the effect of converter operation on the AC losses in the stator and damper windings?
- What can be done to mitigate the potentially adverse effects of converter-operation on the losses in the stator and damper windings?
- How large will the additional iron losses in the stator large hydrogenerators

be during converter operation?

The generator is analysed using finite element simulations as is described in Section 4.1. The framework for calculating the AC eddy-current losses is presented in Section 3.2.5.

5.2 Additional copper losses due to converter operation

AC copper losses due to converter operation have been calculated using a combination of finite element simulation and analytical expression. In Fig. 5.1 the harmonic spectrum of the stator current is presented for a two-level voltage source converter and a three-level NPC topology using 450 Hz and 1050 Hz as carrier frequency. Current waveforms are shown in Fig. 5.2.

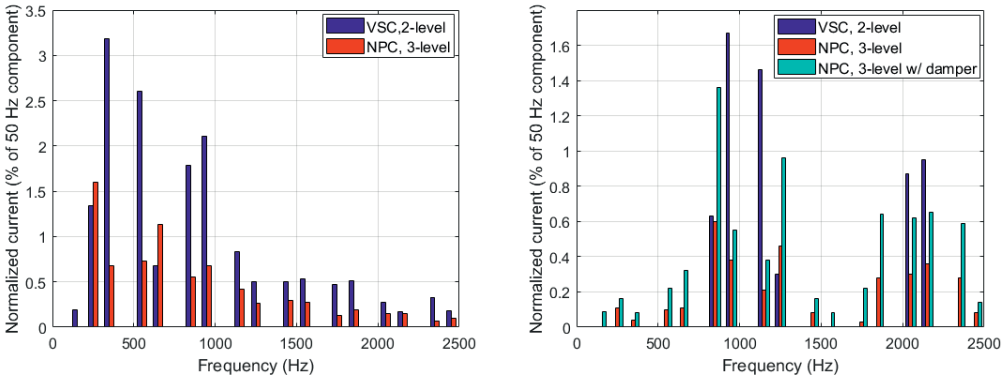

Figure 5.1: Time harmonic spectrum of converter-fed stator current at 450 Hz carrier frequency (left), and 1050 Hz carrier frequency.

As discussed in [42], the dominant additional harmonics produced by the converter switching are $f_{PWM} \pm 2f_s$, $f_{PWM} \pm 4f_s$ and $2f_{PWM} \pm f_s$. f_{PWM} is the carrier frequency and f_s is the synchronous grid frequency. For the case with a 450 Hz carrier frequency, the dominant harmonic frequencies are then 250 Hz, 350 Hz, 550 Hz, 650 Hz, 850 Hz and 950 Hz. If a 1050 Hz carrier frequency is used, the dominating current harmonic components are found at 850 Hz, 950 Hz, 1150 Hz, 1250 Hz, 2050 Hz and 2150 Hz. Converter switching produces, in addition, even higher frequency current harmonics whose amplitudes decrease with increased frequency.

Fig. 5.1 also shows that the amplitude of the current harmonics is drastically reduced when the two-level converter is replaced with a three-level NPC-topology. With a 450 Hz carrier frequency the total harmonic distortion (THD) is reduced

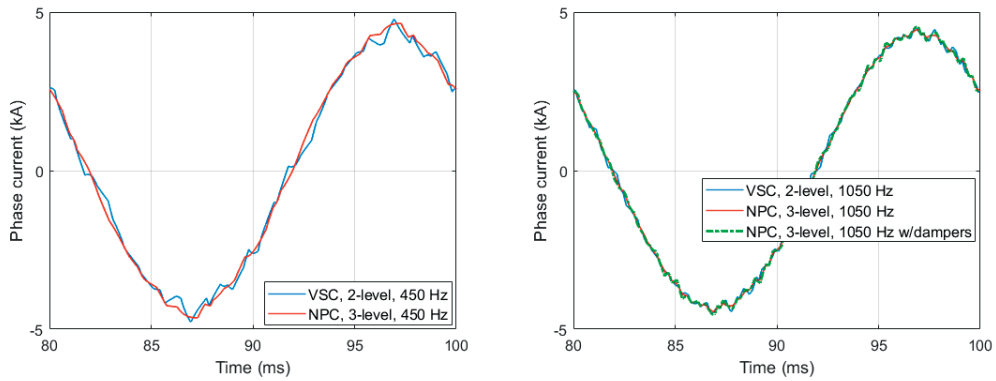

Figure 5.2: Simulated stator current waveforms at 450 Hz carrier frequency (left) and 1050 Hz carrier frequency.

from 5.39% to 2.47% by replacing the two-level VSC with a three-level NPC.

It can be seen by studying Fig. 5.1 that the amplitude of the dominant current harmonics is reduced when the carrier frequency is increased from 450 Hz to 1050 Hz. This gives a lower THD than using the 450 Hz carrier frequency. For the two-level topology the THD is 2.66% and for the NPC the THD is 1.09%.

Using a higher carrier frequency increases the frequency of the dominating current harmonics produced by converter operation. An increased carrier frequency increases the amplitude of these current harmonics. The net effect of these two mechanisms is, sadly, that the AC copper losses increase with higher carrier frequencies.

It is observed in Fig. 5.1 that the presence of damperbars in the rotor will increase the amplitude of the current harmonic components. This results in a significantly higher THD, 2.25%, which is twice the THD experienced without damperbars. Part of the reason for this is that having damperbars reduces the total generator inductance experienced by the converter. Having a lower inductance means that the filtering ability of the circuit is lower, which gives higher current amplitudes.

AC copper losses are compared to the AC copper loss for sinusoidal operation in Fig. 5.3 for the two different converter topologies using 450 Hz and 1050 Hz as the carrier frequency. As can be seen, current harmonics produced by switching increase the AC copper loss from a modest 27.5 kW to between 79 and 485 kW which would cause intolerable heating and probably destroy the winding.

One solution for reducing the AC copper loss is to reduce the strand thickness.

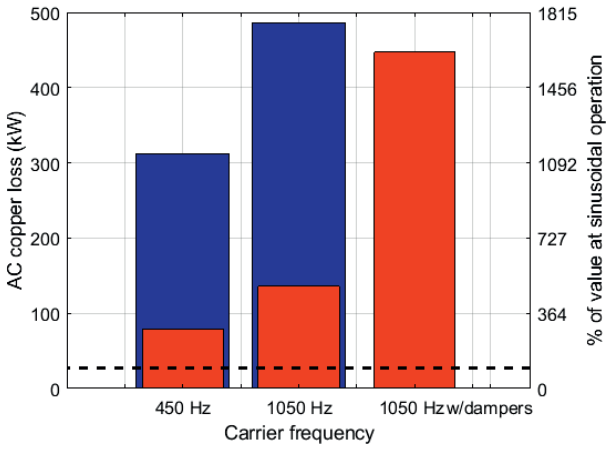

Figure 5.3: AC copper loss at different carrier frequencies.

The original strand thickness of this generator is 1.8 mm. In order for the DC copper loss to stay constant, the number of strands was increased to keep the total conductor area constant.

The effects of reducing the strand thickness on the AC copper loss are presented in Fig. 5.4. It can be seen that it is possible to achieve the same level of AC losses using the NPC-topology as during sinusoidal operation.

Using the lower carrier frequency, i.e. 450 Hz, allows us to reach the original AC copper loss value at a strand thickness of 1.0-1.3 mm. By reducing the strand thickness down towards 1.0 mm it will push towards the lower limit on strand thickness for commercially available Roebel bars.

The minimum bar length needed to achieve full transposition is given by (5.1), where P is the transposition pitch and n_{spb} is the number of strands per bar. In order to have a fully transposed bar, the total length L_{min} must be at least as long as the length of a transposition pitch times the number of strands in the bar.

$$L_{min} = n_{spb} \cdot P \tag{5.1}$$

The transposition factor $F_{transposition}$ given by (5.2) is required to be at least 5 [127]. Depending on the width of each strand in the bar b_{str}, the minimum transposition pitch is given by (5.2).

$$F_{transposition} = \frac{L_{min}}{b_{str} \cdot n_{spb}} = \frac{P}{b_{str}} \tag{5.2}$$

Choosing a lower strand thickness increases the number of strands. Given the length of the transposition pitch, increasing the number of strands will increase the minimum length of the machine required to achieve a fully transposed winding, see (5.1). In a case with many strands per bar, the minimum required length to achieve full transposition could become longer than the axial length of the machine. Then it would become necessary to increase the stack length of the generator.

If 1050 Hz is used as the carrier frequency, the strand thickness would have to be reduced to 1.1 mm or below. This would be challenging to achieve.

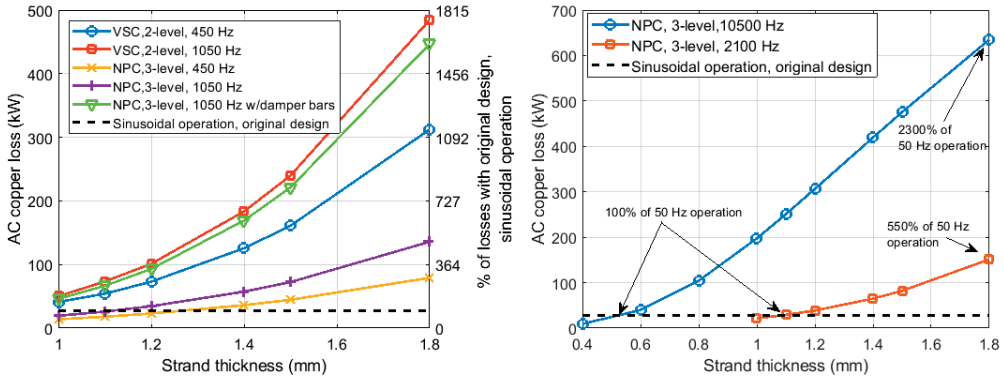

Figure 5.4: Comparison of AC copper losses with different converter topologies and winding designs. Carrier frequency of 450 and 1050 Hz (left), and 2100 and 10500 Hz.

Possible developments in semiconductor technology may allow for the use of higher carrier frequencies. In order to investigate this, the generator is simulated with a carrier frequency of 2100 Hz and 10500 Hz. The current harmonic spectrum for the two cases is presented in Fig. 5.5. It can be seen that the amplitude of the current harmonics is reduced when the carrier frequency is increased. The frequency of each harmonic is also higher for higher carrier frequencies.

The net effect on the losses of increasing the carrier frequency to 2100 Hz and 10500 Hz is presented in Fig. 5.4. It can be seen that although the amplitude of the harmonic currents produced by the converter is small, the AC copper losses increase with increasing carrier frequency. The strand thickness would also have to be reduced to a larger extent for carrier frequencies of 2100 and 10500 Hz than was the case for 450 and 1050 Hz.

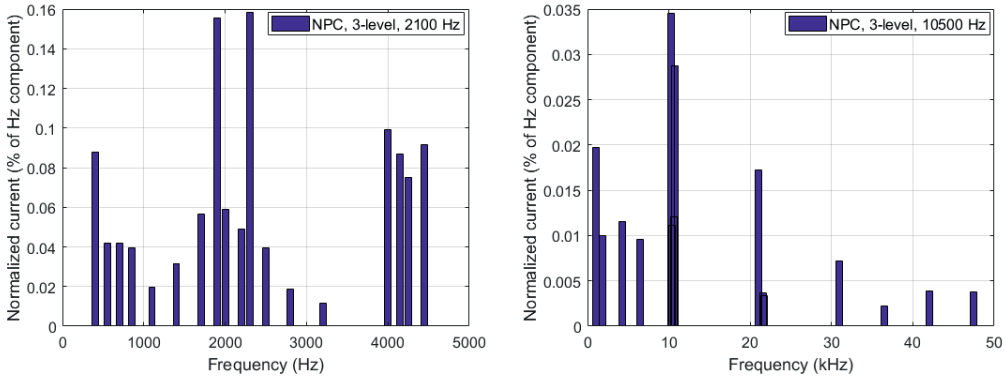

Figure 5.5: Time harmonic spectrum of converter-fed stator current at 2100 Hz carrier frequency (left) and 10500 Hz carrier frequency.

As was discussed for carrier frequencies of 450 Hz and 1050 Hz, a strand thickness down to 1.0 mm is challenging to achieve. As seen in Fig. 5.4, for a carrier frequency of 10500 Hz the strand thickness would have to be reduced to 0.4-0.5 mm. When strand thicknesses this low are required, it might be advisable to look into other options, e.g installing a filter, to avoid overheating and damaging the winding.

In the previous paragraph, it was seen that the damperbars increase the AC copper loss in the stator winding substantially. Converter operation also increases the losses in the damperbars themselves. The two-level VSC topology produces a richer current harmonic spectrum than the three-level NPC topology. This leads to more additional losses with a two-level topology than a three-level topology would produce. While the net effect of increasing the carrier frequency on the stator AC copper losses was that the losses increased, the opposite is true for the losses in the damperbars.

Damperbar losses are calculated directly in the finite element software. The additional losses using carrier frequencies of 450 Hz, 1050 Hz and 2100 Hz are listed in Table 5.1. The resulting losses are 51.9 times, 12.8 times and 5.6 times the losses during sinusoidal operation. The reduction in damperbar losses with increasing carrier frequency is substantial. Thus, using a two-level converter still yields multiple times the damperbar losses experienced in 50 Hz sinusoidal operation, and can therefore not be considered a viable solution.

It is presented in Table 5.1 that the effect of increasing the carrier frequency from 450 Hz to 1050 Hz for the NPC topology is that the losses are decreased from 9.2

times the losses under sinusoidal operation to 3.9 times the losses under sinusoidal operation. By increasing the carrier frequency to 2100 Hz, the damperbar losses are further reduced to 2.3 times the loss under sinusoidal operation. Using a three-level topology is therefore more suitable than the option with a two-level converter, but the increased losses still might cause local heating issues.

There are ways to limit the additional losses in damperbars during converter operation. For the stator winding, reducing the strand thickness means reducing the additional AC copper losses caused by converter harmonics. It is possible to utilize this method for the damperbars in a similar way. In Fig. 5.6 the original damperbar configuration is shown to the left and an alternative damperbar configuration to the right. The total cross section of the damper winding was initially kept the same. The difference is that the number of damperbars per pole is increased from seven to 15, reducing the radius of each damperbar to 68.6% of its original value. It can be seen that the radius of the damperbars is too large to reduce the induced damperbar losses, see Alternative Configuration I in Table 5.1. Thus, as a result, the losses are increased by one third.

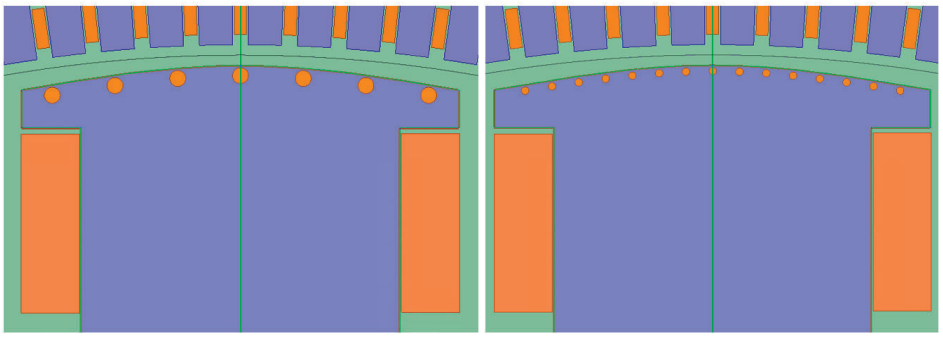

Figure 5.6: Alternative damperbar configurations. Traditional seven bars per pole configuration (left) and alternative 15 bars per pole configuration.

By reducing the radius of each damperbar further, the damperbar losses are reduced. From Table 5.1 it can be seen that the damperbar losses with alternative damper winding configuration II are reduced by 33.5 compared to the damperbar loss with the original damperbar configuration. The radius of each bar is set to 46.7% of its original value. The damperbar loss is still 2.6 times larger than during sinusoidal operation.

This shows that the increase in damperbar losses can be reduced by using an alternative configuration for the damper winding. Further optimization of the damper winding configuration may offer even better results. It should here be noted that

Table 5.1:
Damper winding losses in converter operation at unity power factor

	Damperbar losses (kW)		
f_{PWM} / Topology	450 Hz	1050 Hz	2100 Hz
2-level VSC	498.2 (5189%)	123.3 (1284%)	54.1 (564%)
3-level NPC	88.7 (924%)	37 (385%)	22.2 (231%)
Alternative configuration w/NPC I		49.5 (516%)	
Alternative configuration w/NPC II		24.6 (259%)	
Sinusoidal operation	9.6		

% of losses at sinusoidal operation.

the damping performance of any new configuration has to be checked before any decision or change is made in order to ensure satifsfying operation of the generator.

If a generator is built for converter operation using a two-level or a three-level topology like the ones that are industry standard, one of the following actions must be taken to avoid overheating and damage to the windings:

- The strand thickness must be reduced compared to traditional designs

Or

- A filter would have to be installed between the converter and the generator.

There are limits to how much the strand thickness can be reduced. To mitigate the additional eddy-current losses due to converter operation, a strand thickness as thin as 1.0 mm or lower might be needed. Having strand thicknesses at 1.0 mm and lower is not a viable option. In such a case, and if a frequency converter is to be installed in an existing installation, using a filter will be necessary to avoid excessive heating and damage to the windings.

Based on Fig. 5.4 and Table 5.1, the following conclusion are made:

- Damperbars should not be used when a generator is operated with a two- or three-level converter topology.

Including damperbars in a converter-fed synchronous hydrogenerator without a harmonic filter increases the AC copper losses in the stator. In addition to this,

the losses in the damperbars themselves increase by 130% to 5087.5% during converter operation. This would lead to overheating and most likely the generator catching fire.

If the generator is to be able to operate directly connected to the grid without the converter, then the damperbars must be included to ensure stable operation. Using a filter between the converter and the generator might then be the only option if a two-level or three-level converter is to be used.

5.3 Additional stator iron losses due to converter operation

The same converter topologies that were used to investigate the additional copper losses in the stator winding and damper bars of the 105 MVA, q = 4 $\frac{2}{7}$ generator were used to estimate the additional core losses during converter operation. Measured loss data were not available for this machine. Fig. 5.7 presents the core loss at unity power factor. Core losses were calculated using the Bertotti model. The generator is run with sinusoidal excitation and two different converter topologies at different carrier frequencies in order to investigate the effect of converter harmonics. A two-level voltage source converter and a three-level NPC-converter are simulated with the generator. It is found that the stator core loss, compared to sinusoidal operation, is increased by 20-24% when the two-level topology is used. With the three-level converter the increase in core loss is 11-16%.

For both the converter topologies the difference in core losses between converter operation and sinusoidal operation seems to be reduced by increasing the carrier frequency. Using the three-level converter, the additional stator core loss presented in 5.7 is reduced from 15.6% to 13.6% and 11.5% when the carrier frequency is changed from 450 Hz to 1050 Hz and 2100 Hz. For the two-level converter, the increase in core loss is reduced from 23.7% to 21.8% and 20.7%.

The core loss with and without converter operation is separated into losses in the teeth and in the yoke in Fig. 5.7. It can be noted that the loss in the teeth shows a larger percentage increase than the loss in the yoke when converter- and sinusoidal operation is compared. For the two-level topology the increase in teeth loss is from 23-25.3% depending on carrier frequency. The yoke loss increases by 19-22.6%. Lower carrier frequencies result in higher core losses. The increase in teeth and yoke loss is smaller with the tree-level topology. Yoke losses increase by 8.6-12.4%. The teeth losses increase by 15.5-20%.

The results that have been presented shows that increasing the carrier frequency will reduce the additional iron losses during converter operation.

Fig. 5.7 estimates that an increase in the iron core loss in the range of 10-30% can

be expected using traditional two- and three-level converter topologies. Increasing the number of voltage levels to five, seven or more has been proved to reduce the additional core loss so much that they can become insignificant [57].

Based on this it is concluded that although the additional iron losses during converter operation using two- or three-level topologies are modest, the benefits of using a multi-level converter topology are worthy of further consideration.

It should be noted that the results presented here are produced using existing loss calculation methods that are not designed to incorporate the effect of converter operation. The results should only be taken as a first indication for the level of additional losses in the stator core during converter-operation. More studies should be performed and better core loss estimation methods should be investigated before drawing any firm conclusions on the effect of converter operation on core losses in hydropower generators. This, however, falls outside the scope of this work.

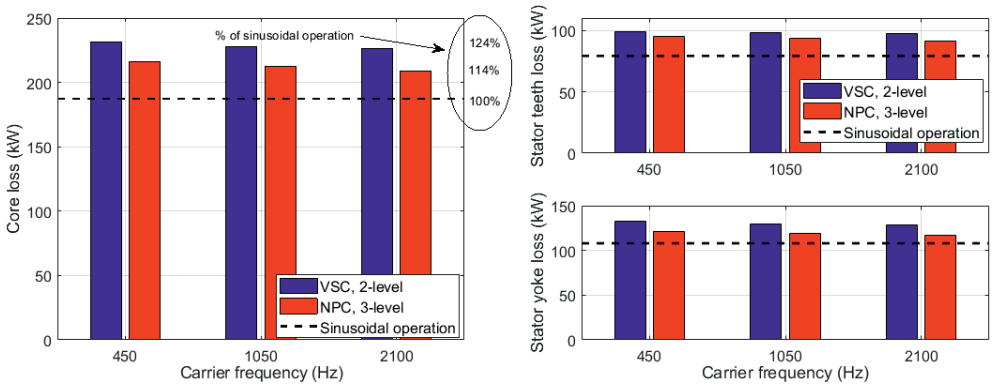

Figure 5.7: Core loss of 105 MVA, q = 4 $\frac{2}{7}$ generator at unity power factor using frequency converter and different carrier frequencies. Total losses (left) and tooth and yoke losses.

5.4 Conclusions

The effect of converter operation on AC copper loss in hydrogenerators has been investigated. Using a higher carrier frequency increases the frequency of the dominating current harmonics produced by converter operation. An increased carrier frequency decreases the amplitude of these current harmonics leading to a lower total harmonic distortion of the stator current. The net effect of these two mechanisms is that the AC copper losses increase with higher carrier frequencies.

Current harmonics produced by switching in two- and three-level converters increase the AC copper losses in traditionally designed stator windings in large hy-

drogenerators. These additional losses could cause intolerable heating and potentially destroy the windings. Using a three-level converter topology instead of a two-level topology gives significant reductions in the AC copper loss.

It is possible to reduce the AC copper losses by reducing the strand thickness in the stator winding. If a generator is going to be built for converter operation using a two-level or a three-level topology like the ones that are available today, it is found that:

- The strand thickness would have to be reduced compared to traditional designs.
- If this is not possible, a filter between the converter and the generator must be used.

Including damperbars in a converter-fed synchronous hydrogenerator increases the AC copper losses in the stator. In addition to this, the losses in the damperbars themselves increase substantially. The additional damperbar losses are smaller using a three-level topology than when a two-level topology is used. Increasing the carrier frequency reduces the additional damperbar losses. It seems that changing the damper winding configuration can also reduce the additional damperbar losses.

- It is advised against using damperbars, if possible, when two- or three-level converter topologies are used.

The results indicate that an increase in the iron core loss in the range of 10-30% can be expected using traditional two- and three-level converter topologies. Additional losses are smaller for the three-level topology than for the two-level converter. For both the converter topologies the difference in core losses between converter operation and sinusoidal operation was reduced by increasing the carrier frequency. It is concluded that the additional iron losses during converter operation using two- or three-level topologies are modest.

Based on the investigation into the additional copper and iron losses in converter operation, the benefits of using a multi-level converter topology are worthy of further investigations.

Chapter 6

Radial forces - influence of winding layout and airgap length

This chapter investigates the flux density and radial force spatial harmonics in large salient pole synchronous hydrogenerators. Vibration due to magnetic forces is mainly caused by low order harmonics in the airgap flux density distribution. The influence of winding layout and airgap length on the lowest order radial force component are analyzed. Airgap flux density and radial force density distributions of three different generators are computed using finite element calculations. The flux density components that contributes to the lowest order force component, and the source for these harmonic components, are investigated. It is found that reducing the airgap length leads to a less than proportional increase in the lowest order radial force component. A rearrangement of the winding layout is found to be an effective method for reducing the lowest order radial force component. The same applies to having damperbars installed, even though the effect is smaller than that achieved by a rearrangement of the winding layout.

6.1 Converter operation and its impact on radial forces

Converter operation of hydropower generators has been shown to introduced both opportunities and challenges, e.g. additional losses. In addition to introducing additional losses, converter operation could introduce challenges regarding radial forces and possible vibration problems. The main issues that might produce problems when the generator is to be converter-fed are:

- Radial forces due to current harmonics produced by the converter

- Changes in the radial forces due to changes in generator design:
  - Effect of changes in airgap length
  - Effect of damperbars

The first topic, radial forces due to current harmonics produced by converter-operation has been investigated by a colleague at The Department of Electric Power Engineering at the Norwegian University of Science and Technolgy (NTNU). The impact of these current harmonics produced by the converter has been presented in [42], and will therefore not be covered further in this chapter.

The focus of the rest of this chapter will be on the design-related impact of converter-operation on the radial forces in the generator. What is meant here is that converter operation relaxes some of the stability requirements that 50 Hz, grid-connected generators have to comply with, i.e. damperbar requirement, upper limit on the per unit value for the synchronous reactance.

The flux density harmonics that contribute to the lowest order radial force component are investigated. Then the effect of changing the airgap length on the lowest order radial force component is investigated. In addition, the effect of damperbars at different airgap lengths is analyzed and discussed. Finally, a method that can be used to mitigate the effect of low order radial force components is presented and investigated.

6.2 Analysis of flux density harmonics

In order to study the causes of the radial forces in hydropower generators based on the Maxwell stress tensor, the spatial harmonic orders of the radial flux density would have to be investigated. Finite element simulations are used to compute the airgap flux density. The harmonic components of the three generators investigated, generators G2, G3 and G4 in Table 3.5, are extracted using a Fourier transformation of the flux density waveform.

The radial spatial harmonic flux density distribution for all three generators at both no-load and full-load are presented in Fig. 6.1. The main flux density harmonic is equal to the pole pair number p. Spatial harmonic orders of odd multiples of the pole pair number are present at no-load.

In addition, spatial harmonics due to slotting are also present. Some of these harmonics, like the ones of order $Q_s \pm p$, have a considerable amplitude. Q_s is the number of slots in the stator. For the q = 2 $\frac{5}{7}$ generator, harmonic orders 107 and 121 are produced by the slotting effect, while for the q = 4 $\frac{2}{7}$ generator harmonic

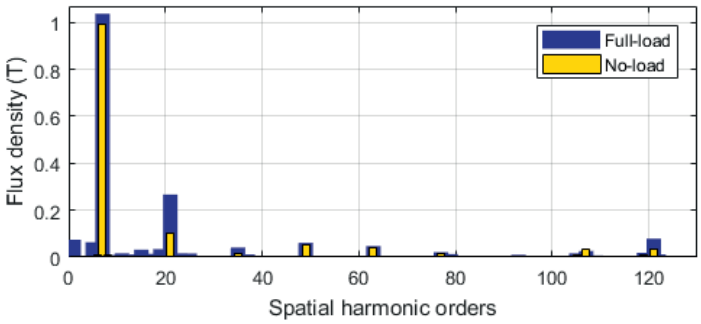

(a) Generator G2: q = 2 $\frac{5}{7}$

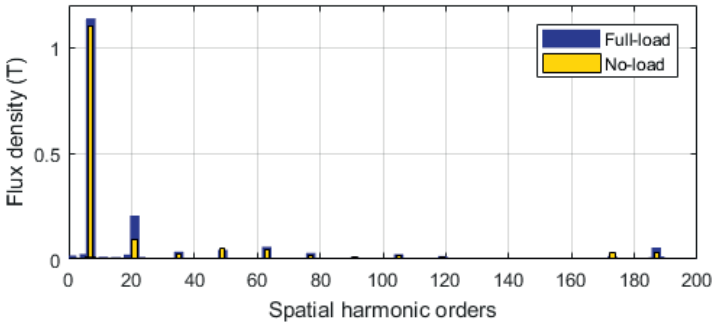

(b) Generator G3: q = 4 $\frac{2}{7}$

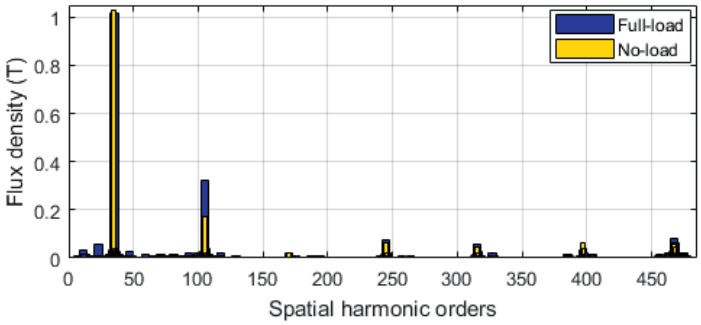

(c) Generator G4: q = 2 $\frac{2}{35}$

Figure 6.1: Harmonic orders of flux density in the airgap at full-load and no-load.

orders 173 and 187 are present due to slotting. In the case of the q = 2 $\frac{2}{35}$ generator, the 397th and 467th harmonics are produced by slotting.

As can be seen from Fig. 6.1 that several harmonic orders that are not present at no-load are visible in the full-load case. Subharmonics, harmonics adjacent to the main harmonic, and harmonics adjacent to the harmonic of order $3p$ are produced by the armature MMF.

It can be noted in Fig. 6.2, a small subharmonic of order 1 can be observed in all three generators. The lowest order flux density harmonic given by the greatest common divisor (GCD) of Q_s and p is 1 for all three generators. All generators were selected to have the lowest possible order of the radial force component.

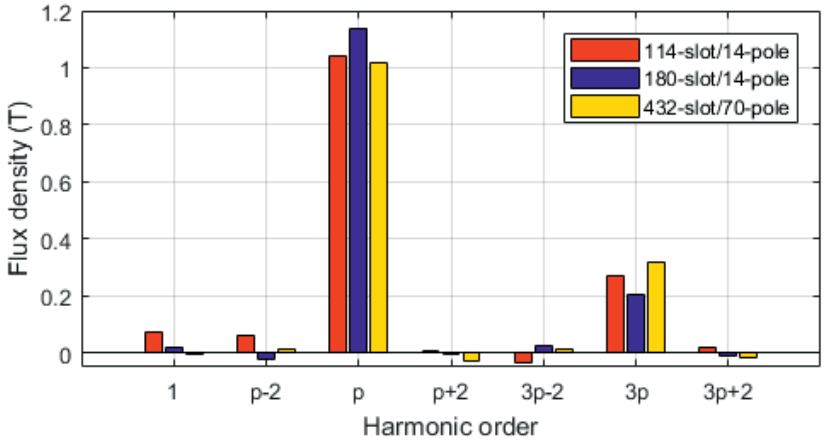

Figure 6.2: Spatial harmonic orders of flux density contributing to the production of second order radial force harmonic.

6.3 Analysis of radial force density

In the generators considered, the tangential flux density harmonics were found to contribute with less than 1% of the second order radial force density. It is therefore neglected in the further analysis.

From Fig 6.2, it can be seen that only a few harmonic components of the airgap flux density of generators G2 and G3 have amplitudes of sufficient size to be included in equation (3.75). Based on this, the second spatial harmonic component of f_{rr} of the q = 2 $\frac{5}{7}$ generator can be written as (6.1).

$$f_{rr}(2^{nd}) = \frac{1}{2\mu_0}(\frac{1}{2}B_1B_1 + B_5B_7 + B_7B_9 + B_{19}B_{21} + B_{21}B_{23}) \qquad (6.1)$$

It is observed that the amplitude and sign of the flux density harmonics in (6.1) determines the amplitude of the second order harmonic force component. From Fig. 6.2 it can be seen that the 1st, 5th, 7th, 9th, 21st and 23rd of the q = 2 $\frac{5}{7}$ generator have the same sign. The 19th harmonic has the opposite sign.

In Fig. 6.3a we can observe that the interaction between the flux density harmonics of orders 5/7, 7/9 and 21/23 contribute to increasing the total second order radial force density. In the q = 2 $\frac{5}{7}$ generator the square of the first order harmonic (6.1) gives a small contribution to the increase in the second order radial force component. The interaction between the harmonic pair of orders 19/21 contributes to a reduction in the total second order radial force density.

The same analysis applies to the q = 4 $\frac{2}{7}$ generator, see Fig. 6.3b. It is the same pairs of flux density harmonics that contribute to the second order force component. In the q = 4 $\frac{2}{7}$ generator and the q = 2 $\frac{2}{35}$ generator, the amplitude of the first order flux density harmonic is so small that the contribution to the second order force component is negligible.

For generator G4, it is also seen in Fig. 6.2 that there are only a few harmonic components that contribute to the second order component of f_{rr}. Similar to generators G2 and G3, the second harmonic component of f_{rr} can be written as (6.2).

$$\begin{aligned} f_{rr}(2^{nd}) = \frac{1}{2\mu_0}(&B_{33}B_{35} + B_{34}B_{36} + B_{35}B_{37} + B_{103}B_{105} \\ &+ B_{104}B_{106} + B_{105}B_{107} + B_{106}B_{108}) \end{aligned} \tag{6.2}$$

From Fig. 6.2 it can be seen that the 33rd, 35th, 103rd and 105th flux density harmonic of the q = 2 $\frac{2}{35}$ generator have the same sign. The 37th and the 107th flux density harmonic have the opposite sign.

In Fig. 6.3c we can observe that the interaction between the flux density harmonic pairs of orders 34/36, 35/37, 104/106 and 105/107 contribute to increasing the total second order radial force density. The interaction between the harmonic pairs of orders 33/35, 103/105 and 106/108 contributes to a reduction in the total second order radial force density.

Based on Fig. 6.3 it can be concluded that the second order force component is mainly produced by the interaction between the main flux density harmonic and the two flux density components adjacent to the main harmonic. These harmonics have small amplitudes in no-load operation. It can be seen from Table 6.1 that the second order radial force component is small in no-load. Based on this it can be concluded that the harmonics of the stator MMF produce most of the lowest order

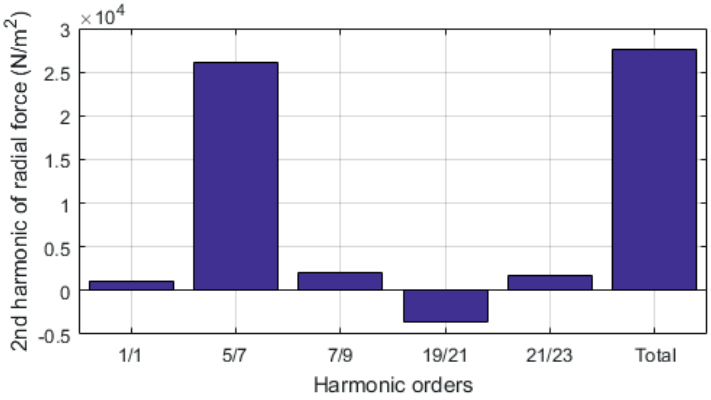

(a) q = 2 $\frac{5}{7}$ generator

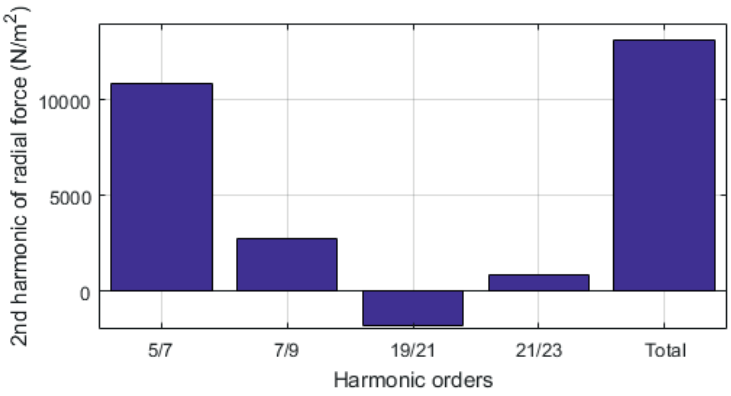

(b) q = 4 $\frac{2}{7}$ generator

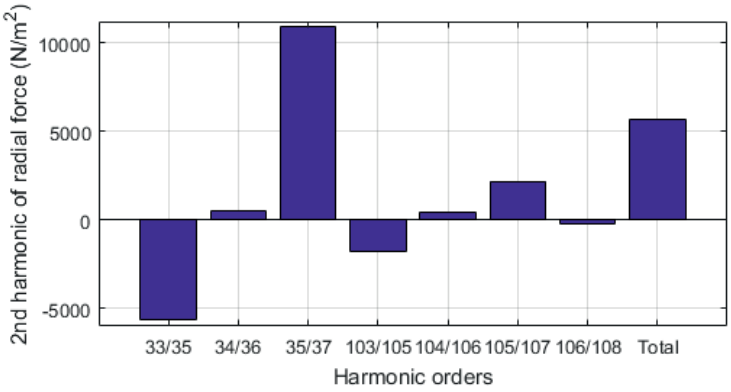

(c) q = 2 $\frac{2}{35}$ generator

Figure 6.3: Contribution of different flux density harmonics that produce the second harmonic order on radial force distribution.

radial force component.

Table 6.1:
Second order radial force component at different loading

	F_2 (N/m^2)	
Generator:	No-load	Full-load
q = 2 $\frac{5}{7}$	1253	27610
q = 4 $\frac{2}{7}$	387	13140
q = 2 $\frac{2}{35}$	521	5671

Load dependency on the second order radial force component of the q = 4 $\frac{2}{7}$ generator is explored in Fig. 6.4. Since the second order force component is mainly produced by the interaction between the main flux density harmonic and the adjacent harmonics produced by the stator winding MMF, the amplitude of the force component increase with increasing load.

With linear material properties in the magnetic circuit of the generator, a proportional increase in the radial forces with increasing loading of the stator windings may be expected. As can be seen in Fig. 6.4, this is clearly not the case. The main cause for the second order component is the product of the flux density harmonics of order $p-2$ and p. It can be seen that the change in the force component follows the same slope as flux density harmonic of order $p-2$. The main flux density harmonic remains more or less constant.

As the loading of the stator winding increases, the flux density component of order $3p$ increases. This leads to more saturation in the generator, which will reduce the increase of the flux density harmonic of order $p-2$. Increasing the loading beyond 100% increases the saturation even more, which leads to a reduction in both the flux density harmonics adjacent to the main harmonic and the second order radial force component.

6.4 Effects of airgap length and damperbars

In [128] it was found that the cost of the generator is reduced when the synchronous reactance is increased by reducing the airgap length. In this section the influence on the lowest order radial force component of reducing the airgap length is investigated. The main flux density harmonic is kept constant when the airgap length is reduced.

The effect of reducing the airgap length on the radial force component of lowest harmonic order is presented in Table 6.2. It can be seen that reducing the airgap length to as little as 60% of its initial value leads to modest increases in the radial

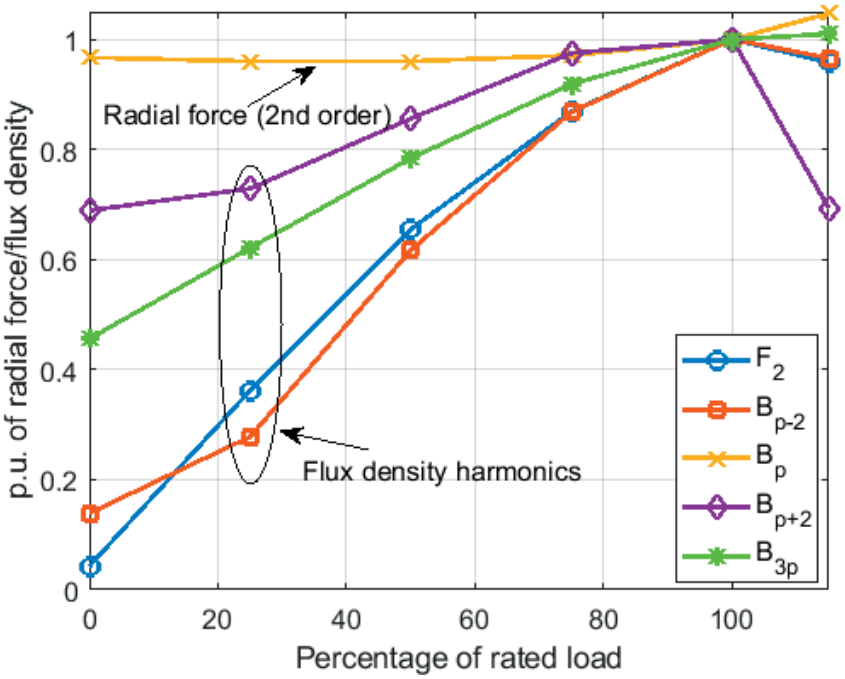

Figure 6.4: Effect of loading on the second order radial force component in the q = 4 $\frac{2}{7}$ generator.

force component. Reducing the airgap length to 60% increases the lowest order force component of the q = 2 $\frac{2}{35}$ generator by 47.6%, the q = 2 $\frac{5}{7}$ generator by 40.2% and the q = 4 $\frac{2}{7}$ generator by 22.3%.

If it is assumed the increase in the second order radial force component is proportional to the reduction in airgap length, the increase should have been 66.7%. Some of this could be explained by the change in the effective airgap length not being the same as the change in the physical airgap length due to Carter's coefficient. Another explanation that is worthy of consideration is the saturation level of each generator.

For generators G2 and G3, it is the flux density component of order $p - 2$ that interacts with the main harmonic to produce most of the second order radial force density. It can be seen from Table 6.2 that the increase in this component closely resembles the increase in the second order force component. For the q = 2 $\frac{5}{7}$ generator the increase in the flux density component of order $p - 2$ was 36.5% while the force component increased with 40.2%. The same case can be seen for the q = 4 $\frac{2}{7}$ generator where the flux density harmonic of order $p - 2$ increased by 29.2% while the force increased by 22.3%. The same effect is seen for the q = 2 $\frac{2}{35}$ generator. The only difference is that for this generator it is the flux density harmonic of order $p + 2$ and not $p - 2$ in interaction with the main harmonic that produces most of the second order radial force.

Table 6.2:
Effects of changing the airgap length

q	2 $\frac{5}{7}$		4 $\frac{2}{7}$		2 $\frac{2}{35}$	
Airgap (mm)	35 o	22 r	27 o	16 r	25 o	15 r
B_{p-2} (T)	0.063	0.086	0.024	0.031	0.014	0.014
B_{p-2}	6.1%	8.3%	2.1%	2.6%	1.4%	1.4%
B_p (T)	1.04	1.06	1.14	1.17	1.017	1.016
B_{p+2} (T)	0.005	0.011	0.006	0.006	0.027	0.033
B_{p+2}	0.5%	1%	0.5%	0.5%	2.7%	3.2%
F_2 ($\mathrm{N/m^2}$)	27610	38710	13140	16070	5671	8370

o - original and r - reduced airgap. % of B_p

Table 6.3 presents the distribution of magnetic energy in the different parts of the generators at different airgap lengths. Values for the different parts are given in percentage of the total magnetic energy, which is proportional to the magnetic reluctance. A high percentage means a high reluctance, which means that a large share of the magnetic energy is consumed in the given part.

Table 6.3:
Magnetic energy in different parts of the generators

q	$2\frac{5}{7}$		$4\frac{2}{7}$		$2\frac{2}{35}$	
Airgap (mm)	35 o	22 r	27 o	16 r	25 o	15 r
Airgap (%)	81.0	77.2	50.8	41.2	75.1	71.3
Stator yoke (%)	0.4	0.8	1.5	2.3	0.6	1.0
Stator teeth (%)	0.7	1.5	0.3	0.5	1.5	3.4
Pole core (%)	10.1	11.7	36.3	41.9	6.6	7.6
Rotor ring (%)	2.0	2.4	7.3	8.5	8.6	8.1
Total (kJ/m)	269	207	339	288	559	404

(%) of the total magnetic energy, o/r - original/reduced airgap.

One can see that the main part of the magnetic energy is stored in the airgap. For the q = $2\frac{5}{7}$ and q = $2\frac{2}{35}$ generators 71-81% of the magnetic energy is consumed in the airgap. For the q = $4\frac{2}{7}$ generator 40-51% is consumed in the airgap.

It is seen in Table 6.3 that the share of the total energy consumed in the airgap is reduced when the airgap is reduced. This is because the saturation level increases in all the iron parts in the magnetic circuit. Except for the airgap, the pole core and rotor ring are the parts that have the highest share of magnetic energy. In particular, the pole core which has to conduct all the flux produced by the field winding is likely to be saturated.

The q = $4\frac{2}{7}$ generator has a significantly higher saturation level in the pole core and share of the magnetic energy than the other generators. A consequence of this is that the amplitude of the flux density harmonics in the airgap of the q = $4\frac{2}{7}$ generator is smaller than would have been the case with a less saturated pole core.

A more saturated generator seems to reduce the lowest order spatial harmonic of the radial force density distribution through a reduction in the amplitude of the flux density harmonics adjacent to the main flux density harmonic. The downside to increasing the saturation is increased losses in the iron parts.

In [87] it was assumed that all the magnetic energy was consumed in the airgap. This study has shown that this is not the case for large synchronous hydrogenerators. Using only the airgap permeance function and the stator MMF harmonics is not sufficient to calculate the amplitude of the airgap flux density harmonics correctly. With 20-50% of the magnetic energy not being consumed in the airgap, it is clear that finite element simulations are needed.

Based on Table 6.2 it is concluded that in salient pole synchronous hydrogenerators

a reduction in the airgap length will not result in a linear increase in the lowest order radial force component as was predicted by [87].

The effects of damperbars on the second order radial force harmonic are investigated by running q = 4 $\frac{2}{7}$ generator at unity power factor. The generator is run with and without damperbars, and with both the original and the reduced airgap length. Fig. 6.5 presents the results for the second order force component at the original airgap length. The average value of the second order force component is reduced by 30% when the damperbars are installed. It can be seen that the effect of damperbars varies with time, so that the effect seems to vary from an 18.7% reduction to a 39.2% reduction.

The flux density harmonic components that produces the majority of the second order radial force component are presented in Fig. 6.6. It can be seen that the damperbars lead to the same time variation in the flux density components as in the radial force component. The flux density harmonics of order B_{p-2} and B_{p+2} are reduced, while the main flux density harmonic B_p increases slightly, resulting in a lower average value for the second order radial force component.

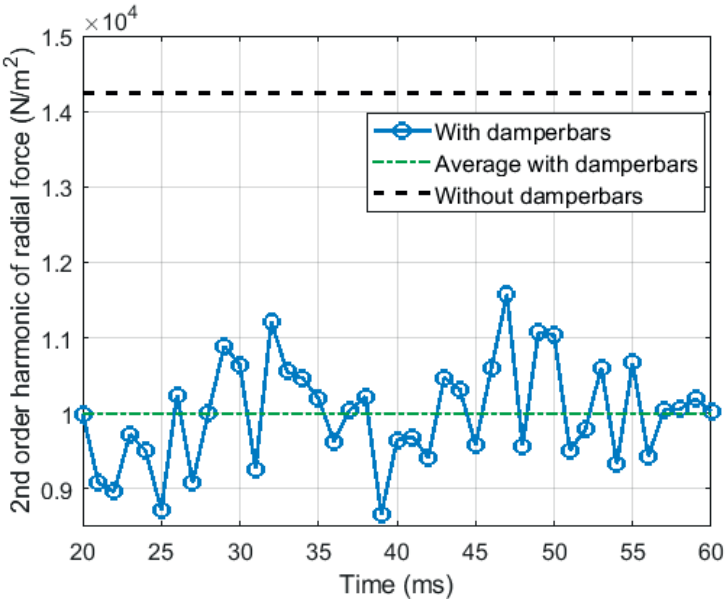

Figure 6.5: Effect of damperbars on the second order radial force component in the q = 4 $\frac{2}{7}$ generator at unity power factor.

Table 6.4 presents the effect of damperbars on the second order radial force component and the main flux density harmonics contributing to the lowest order force

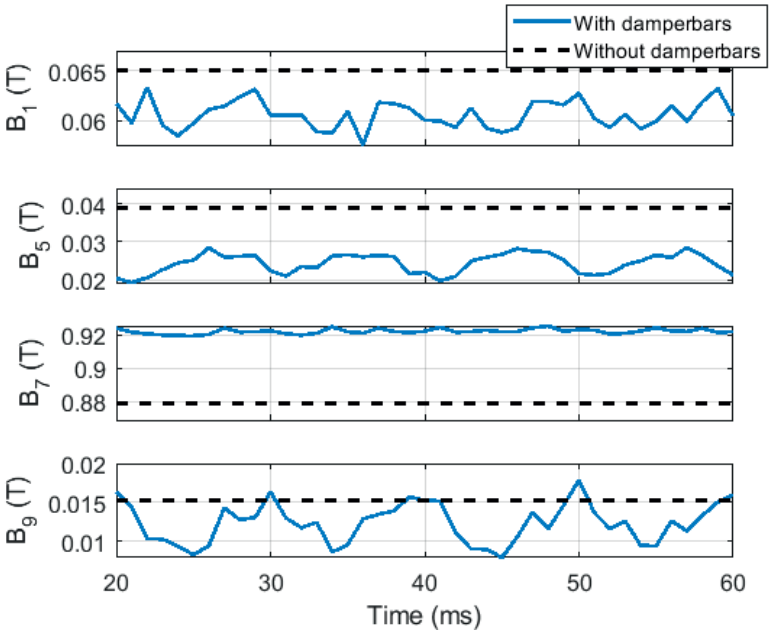

Figure 6.6: Effect of damperbars on the main airgap flux density harmonics in the q = 4 $\frac{2}{7}$ generator at unity power factor.

component at the original and the reduced airgap length. As presented in Table 6.2, when damperbars are removed, B_{p-2}, B_{p+2} and F_2 increase with a reduction in the airgap length. With damperbars F_2 does not seem to increase with reduced airgap length. The reason for this is that B_{p-2} and B_{p+2} remain almost unchanged. F_2 is actually reduced somewhat due to the fact that B_p is reduced by 4.6%.

In conclusion, the damperbars are able to reduce the lowest order radial force component by between 20-40% compared to the case without damperbars. The damperbars are able to reduce the lowest order force component more efficiently when the airgap length is reduced. The downside of this is that the losses in the damperbars themselves are increased from 7 kW to 13.4 kW when the airgap length is reduced.

Losses in the pole shoe surface are expected to increase when the airgap length is reduced in a similar manner to that seen for the damperbars. The analytical framework presented in Chapter 4 is used to estimate the pole surface losses in this case. In the q = 4 $\frac{2}{7}$ generator, the losses increased from 4.8 kW to 12.4 kW, while the losses increased from 18.0 kW to 42.4 kW in the q = 2 $\frac{2}{35}$ generator. For the q = 2 $\frac{5}{7}$ generator, the losses increased from 35.9 kW to 89.1 kW.

Table 6.4:
Effects of damperbars

	wo/ damperbars		w/ damperbars	
Airgap (mm)	27 o	16 r	27 o	16 r
B_1 (T)	0.065 (7.4%)	0.081 (9.6%)	0.061 (6.6%)	0.065 (7.4%)
B_{p-2} (T)	0.039 (4.4%)	0.055 (.5%)	0.024 (2.6%)	0.025 (2.8%)
B_p (T)	0.879	0.841	0.922	0.880
B_{p+2} (T)	0.015 (1.7%)	0.026 (3.1%)	0.012 (1.3%)	0.14 (15.9%)
F_2 ($\mathrm{N/m^2}$)	14240	16940	9994	9345

o - original and r - reduced airgap. % of B_p .

6.5 Effects of winding layout

The flux density harmonic components adjacent to the main harmonic are the ones that produce most of the lowest order radial force component. In Table 6.5 the two adjacent harmonics to the main flux density harmonic are presented for no-load and full-load. The amplitude of the main harmonic is the same in both load conditions. It can be noted that for the q = 4 $\frac{2}{7}$ and the q = 2 $\frac{5}{7}$ generators, the harmonic of order $p + 2$ is more or less independent of loading. In addition, this flux density harmonic is much smaller than the harmonic of order $p - 2$.

The harmonic of order $p - 2$ is mostly given by the armature MMF. Together with the main harmonic it is the main contributor to the lowest order radial force component. It is of interest to find a winding arrangement that minimizes this flux density harmonic while maintaining the amplitude of the main harmonic.

For the q = 2 $\frac{2}{35}$ generator, see Table 6.5, it can be seen that harmonic of order $p - 2$ is barely affected by loading. The harmonic of order $p + 2$ is the largest contributor to the lowest order force component together with the main harmonic. It can be seen that this flux density harmonic component is present both at no-load and full-load.

The q = 2 $\frac{5}{7}$ generator is chosen in order to investigate how the winding layout pattern is affecting the flux density harmonic of order $p - 2$. This generator has the largest second order force component and the flux density component of order $p - 2$. The winding pattern of the original winding is 3-3-3-2-3-3-2, see Table 6.6. It was produced using the method for winding layout that was presented in Section 3.1.3 using the voltage-star concept and a procedure similar to that presented in Figs. 3.13 and 3.14.

It is found that the pattern can be ordered in 21 possible configurations. All these

Table 6.5:
Flux density harmonics of order $p \pm 2$

	B_{p-2} (T)		B_{p+2} (T)	
Generator:	No-load	Full-load	No-load	Full-load
q = 2 $\frac{5}{7}$	0.003 (0.3%)	0.063 (6.1%)	0.005 (0.5%)	0.005 (0.5%)
q = 4 $\frac{2}{7}$	0.003 (0.3%)	0.024 (2.1%)	0.004 (0.4%)	0.006 (0.5%)
q = 2 $\frac{2}{35}$	0.017 (1.7%)	0.014 (1.4%)	0.019 (1.9%)	0.027 (2.7%)

% of main harmonic component value.

patterns were implemented and simulated. Of all the possible patterns, a pattern giving one of the lowest flux density component of order $p-2$ while barely reducing the main harmonic was selected. The new winding pattern is 3-3-3-2-2-3-3, see Table 6.7, and the comparison to the original winding pattern is shown in Table 6.6. The voltage waveform of the original and the new winding layout are presented in Fig. 6.7 Several winding configurations gave a satisfying reduction in the flux density harmonic of order $p-2$, but they also gave a significant reduction in the main harmonic.

Table 6.6:
Original winding layout configuration.

RRR	-T-T-T	SSS	-R-R	TTT	-S-S-S	RR
-T-T-T	SSS	-R-R-R	TT	-S-S-S	RRR	-T-T
SSS	-R-R-R	TTT	-S-S	RRR	TTT	SS

Table 6.7:
New winding layout configuration.

RRR	-T-T-T	SSS	-R-R	TT	-S-S-S	RRR
-T-T-T	SSS	-R-R-R	TT	-S-S	RRR	-T-T-T
SSS	-R-R-R	TTT	-S-S	RR	TTT	SSS

The flux density harmonics of order 1, $p-2$, p, $p+2$ and the lowest order radial force component of all the 21 winding layouts that were analyzed are presented in Table 6.8.

It can be seen from Table 6.9 that the reduction in the flux density harmonic of order $p-2$ is 63.5%. The second order radial force component sees a 60.7% reduction when the winding pattern is changed. The flux density harmonic of

Table 6.8:
Effects of changing the winding pattern

Pattern:	B_1 (T)	B_{p-2} (T)	B_p (T)	B_{p+2} (T)	F_2 (N/m^2)
2-2-3-3-3-3-3	0.14	0.032	1.178	0.004	13880
2-3-2-3-3-3-3	0.12	0.020	1.171	0.002	12150
2-3-3-2-3-3-3	0.063	0.057	1.172	0.008	25420
2-3-3-3-2-3-3	0.065	0.057	1.147	0.013	26480
2-3-3-3-3-2-3	0.14	0.018	1.093	0.013	15960
2-3-3-3-3-3-2	0.16	0.028	1.047	0.010	13010
3-2-2-3-3-3-3	0.14	0.046	1.104	0.023	22210
3-2-3-2-3-3-3	0.11	0.008	1.119	0.018	11970
3-2-3-3-2-3-3	0.043	0.055	1.111	0.025	32060
3-2-3-3-3-2-3	0.07	0.055	1.098	0.015	28780
3-2-3-3-3-3-2	0.14	0.020	1.046	0.009	16400
3-3-2-2-3-3-3	0.14	0.041	1.075	0.012	16170
3-3-2-3-2-3-3	0.11	0.032	1.071	0.014	19350
3-3-2-3-3-2-3	0.071	0.057	1.076	0.012	28680
3-3-2-3-3-3-2	0.074	0.061	1.056	0.008	28000
3-3-3-2-2-3-3	0.15	0.023	1.025	0.005	10860
3-3-3-2-3-3-2	0.075	0.063	1.038	0.005	27610
3-3-3-3-2-2-3	0.17	0.21	0.985	0.003	10120
3-3-3-3-2-3-2	0.15	0.025	0.991	0.008	16990
3-3-3-3-3-2-2	0.18	0.018	0.956	0.011	9380

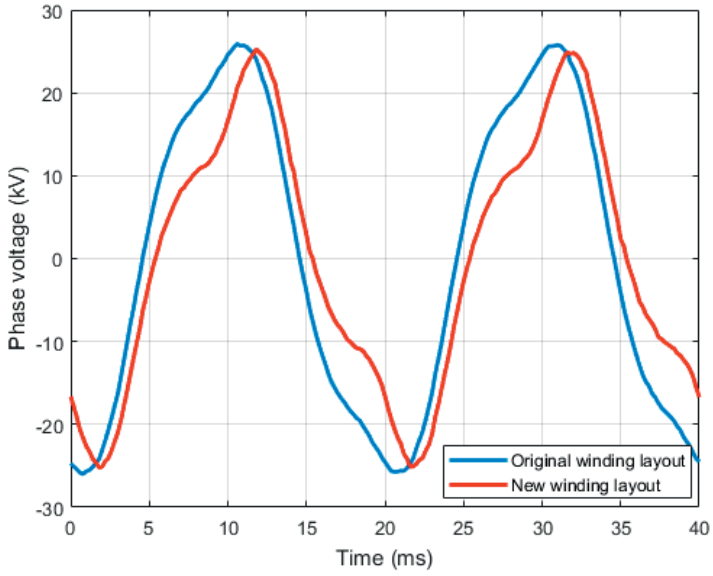

Figure 6.7: Voltage waveform of phase voltage in q = 2 $\frac{5}{7}$ generator with different winding layouts.

order $p+2$ remains unchanged while the main harmonic component sees a 1.25% reduction.

Since both subharmonic components and harmonic components are produced by the winding pattern, it was expected that these could change with new winding patterns. It turned out that for all the patterns implemented and simulated, the harmonic flux density components with harmonic order k times p remained practically unchanged ($k = 3, 5, 7$, etc).

The subharmonic flux density component of order 1 was found to change considerably with the change in winding pattern. As can be seen in Table 6.9 this component was doubled in the new pattern compared to the original winding layout. It seems that a reduction in the flux density harmonic of order $p-2$ provides an increase in the first order harmonic. The increase in the first order flux density harmonic increases the second order force component. This helps to explain why the reduction in the lowest order radial force component is smaller than the reduction in the flux density harmonics of order $p-2$ and p.

Two main conclusions may be drawn from this. First, that the amplitude of the largest flux density harmonic adjacent to the main, or fundamental, harmonic can be heavily reduced by careful rearrangement of the winding configuration. Second,

Table 6.9:
Effects of changing the winding pattern

Layout:	B_1 (T)	B_{p-2} (T)	B_p (T)	B_{p+2} (T)	F_2 (N/m^2)
Original	0.075 (7.2%)	0.063 (6.1%)	1.038	0.005 (0.5%)	27610
New	0.15 (14.6%)	0.023 (2.2%)	1.025	0.005 (0.5%)	10860

% of main harmonic component value B_p.

in cases where low order radial forces cause vibration problems, the problem can be significantly reduced by rearranging the winding configuration. Again, this reinforces the conclusions made in [94] and [87] about the usefulness of winding-reconfiguration when the goal is to reduce low order radial forces.

6.6 Conclusions

The following conclusions can be drawn from the analysis presented in this chapter:

It has been found that the lowest order harmonic component of the radial force is primarily produced by the main flux density harmonic component and its adjacent harmonic components.

In salient pole synchronous hydrogenerators, the magnetic circuit can be heavily loaded. In the cases investigated here, more than 20% of the magnetic energy is consumed in parts of the generator other than the airgap.

Reducing the airgap length leads to a less than proportional increase in the lowest order radial force component due to increased saturation in the generator and the fact that a substantial part of the magnetic energy is not consumed in the airgap.

Based on the damperbar configuration that was studied it was found that damperbars are able to reduce the lowest order radial force component by between 20-40% compared to the case without damperbars. The damperbars are able to reduce the lowest order force component more efficiently when the airgap length is reduced. The downside of this is that the losses in the damperbars themselves are increased when the airgap length is reduced.

The amplitude of the largest flux density harmonic adjacent to the main harmonic can be heavily reduced by careful rearrangement of the winding configuration. In cases where low order radial forces cause vibration problems, the problem can be significantly reduced by rearranging the winding configuration. It was possible to reduce the lowest order radial force component by more than 60% by rearranging the winding layout.

If the flux density harmonics and the radial forces in large synchronous hydrogenerators are to be calculated accurately, it is found that finite element simulations are needed.

Chapter 7

Optimal design for converter-fed operation

The purpose of this chapter is to investigate how the rated frequency affects cost, weight and efficiency of the generator. The rated speed of rotation varies between 275 rpm and 600 rpm, while the nominal frequency used is between 25 and 75 Hz. The optimal frequency that gives the lowest total cost is reached between 40 Hz and 50 Hz. Generators with higher rotational speeds tend to have a higher optimal rated frequency. The maximum allowed per unit value of the synchronous reactance is normally decided by the grid codes in order to maintain the stability of the system. In this chapter the constraint on the synchronous reactance is relaxed from 1.2 per unit to 2.0 per unit and then removed altogether. It is concluded that the total generator cost is reduced when the synchronous reactance is increased.

7.1 Cost coefficients used to find the optimal design

In order to optimize both production cost and efficiency at the same time, without using multiple objective functions, the cost of the generator is chosen as the objective function. Prices for the different materials are based on typical values similar to those used in other publications [121]. The unit prices for the active materials that are used are:

- stator iron C_{lam}: 4 €/kg
- rotor iron C_{steel}: 6 €/kg
- copper C_{cu}: 11 €/kg

For the losses, it is assumed that the generator is not run as a base plant at rated power output all the time. The cost of losses may vary from market to market. In this paper the cost of constant losses is set to 3000 €/kW, while the cost of load dependent losses is set to 2000 €/kW.

7.2 Choice of optimal rated frequency

In variable speed pumped storage power plants, the converter-fed synchronous machine has been presented as a promising solution to use instead of the traditional fixed-speed, grid-connected, synchronous generator. In this case the rated frequency of the hydropower generator can be chosen independent from the grid frequency.

The purpose of this chapter is to investigate what the optimal rated frequency would be for a large hydropower generator when the converter-fed synchronous machine topology is used. In order to achieve this the generator design is optimized to minimize the total cost, which consists of the cost of materials and the cost of energy losses.

The minimum total cost of active materials and energy lost found through the optimization process is presented in Fig. 7.1 for different rotational speeds and rated frequencies. It can be seen that although the total cost changes with rotational speed and rated frequency, the difference is modest. The total cost of the most expensive design option in Fig. 7.1 is only 18% higher than the cheapest design.

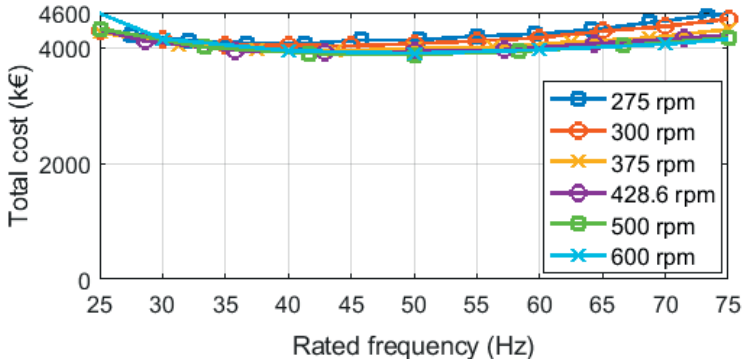

Figure 7.1: Total generator cost at different rated frequencies and rotational speeds.

Fig. 7.2 presents the total cost of the generator as a function of rated frequency and rated rotational speed, focusing on the range from the cheapest to the most expensive design. It is found that the cost of materials is reduced when the rated frequency is increased due to the fact that the total weight is reduced for higher fre-

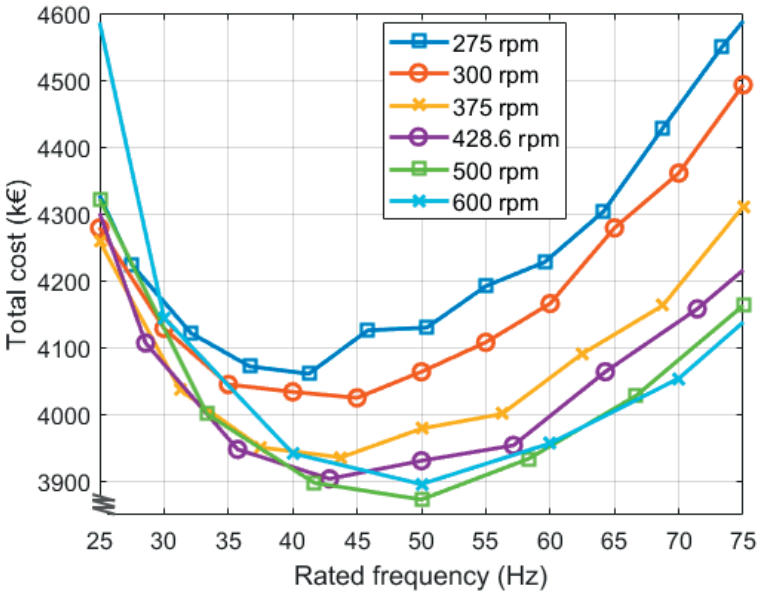

Figure 7.2: Total generator cost at different rated frequencies and rotational speeds.

quencies. The mechanisms driving the weight reduction will be further elaborated upon in Section 7.2.1.

The cost of losses and the total losses are increased when the rated frequency is increased. The major reasons for this will be explained in more detail in the following paragraphs. To summarize, the total cost of the generator will reach its minimum at the optimal rated frequency where the reduction in materials cost is equal to the increase in the cost of losses. The optimal rated frequency seems to be in the range of 40 Hz to 50 Hz with the slower rotational speeds giving lower values for the optimal frequency.

At lower rated frequencies, the total cost is reduced when the rated frequency is increased. This is the case up to rated frequencies of 40 Hz to 50 Hz where the total cost reaches its minimum value for all rotational speeds. When the rated frequency is increased past the frequencies that yield the lowest total cost, the total cost is increased for all rated frequencies and rotational speeds.

7.2.1 Weight of materials in the generator

An increase in the rated frequency is produced by adding more poles to the generator. Since an additional pole will require more space along the airgap periphery, it is found beneficial by the optimization algorithm to increase the airgap diameter

D as can be seen in Fig. 7.3. There is no conclusive trend to be found for the axial length other than a slight increase at the highest rated frequencies. As a product, the airgap volume D^2L increases when the rated frequency is increased, see Fig. 7.3.

With regard to different rotational speeds, it can be seen that D is larger and L is smaller for the lowest rotating generators. The airgap volume is higher for the slower generators as the airgap diameter yields a stronger impact on the volume than the axial length. Slower rotational speeds require a higher pole number to produce the same rated frequency. Therefore, the diameter and volume becomes larger. Slower generators tend to be shorter in axial length than the faster rotating ones.

Based on (3.7) it can be seen that when the airgap volume D^2L goes up the armature loading A and the magnetic loading B_δ needed to produce the rated power is reduced. This can be seen in Fig. 7.4, where the armature loading is reduced considerably and the magnetic loading is also reduced slightly when the rated frequency is increased. When A and B are reduced the required field current and stator current goes down, resulting in less copper needed and less current to cause copper losses.

Since the armature loading, which is a function of the stator current, is reduced when the rated frequency is increased, the stator current is reduced and the stator voltage is increased. At higher rated frequencies the stator voltage is more dominant in producing the rated output power than the stator current. This has a direct impact on the weight of copper used in the stator winding and the copper losses in the winding.

When the airgap volume is increased, the required armature loading is found to go down, reducing the rated stator current. When the rated stator current is reduced the cross section needed to avoid excessive heating of the winding caused by a current density that is too high for the cooling system is reduced. As a consequence the amount of copper used in the winding can be reduced and with it the weight of the winding, see Fig. 7.5.

Another factor that tends to reduce the weight of the stator winding is that when the rated frequency is increased, the pole pitch and coil pitch will be reduced to maintain a high winding factor. When the coil pitch is reduced, the length of the end winding is reduced, giving an additional reduction in the weight of copper as presented in Fig. 7.5.

When the rated frequency is increased by increasing the number of poles, the air gap length is reduced in order to keep the synchronous reactance constant as de-

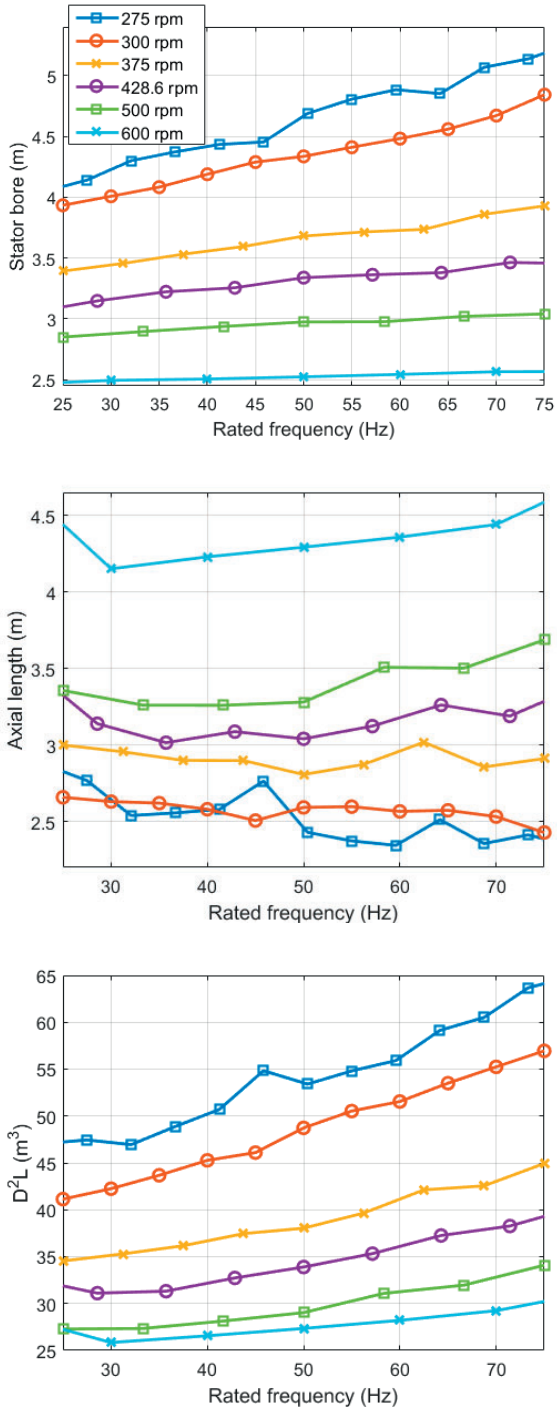

Figure 7.3: Stator bore (top), axial length (middle) and airgap volume at different rated frequencies and rotational speeds.

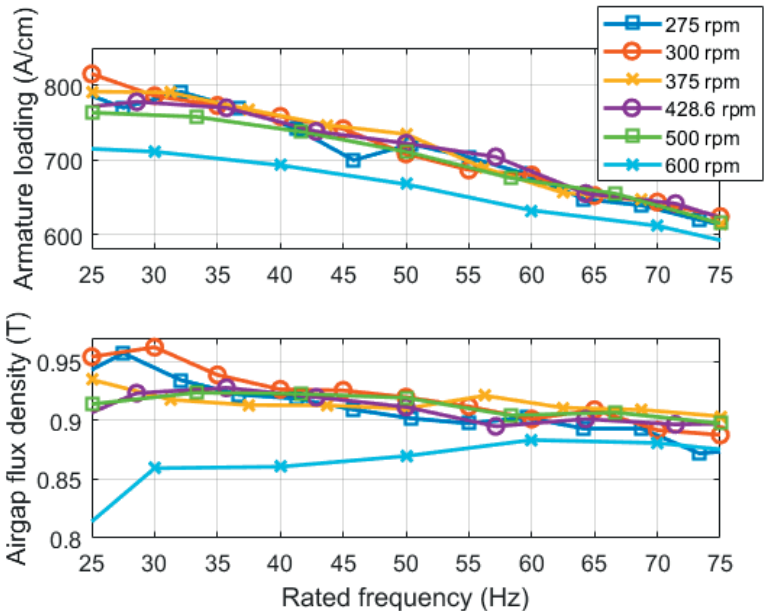

Figure 7.4: Loading of the generator, electric loading (top) and magnetic loading.

scribed in (3.38). The required magnetizing ampere-turns per pole is reduced when the air gap length is reduced, see Fig. 7.6, and so is the thickness of the stator yoke.

The weight of the field winding is also presented in Fig. 7.5. When the required ampere-turns per pole is reduced, the required amount of copper in each pole will go down and reduce the weight of the winding. A higher number of poles will increase the weight of copper in the field winding since copper is added for each additional pole. The net effect is that the weight of the field winding is reduced when the rated frequency is increased.

The total weight of active materials in the generator and the weight of stator iron is presented in Fig. 7.7. It can be seen that the weight of both stator iron and the total weight are reduced considerably when the rated frequency is increased, which is the same trend as was observed for the stator and field winding in Fig. 7.5.

As presented in (3.10), when the rated frequency is increased by increasing the number of poles the thickness of the stator yoke and the rotor ring is reduced. The reduction in stator yoke thickness is visualized in Fig. 7.8 where the geometries of two 275 rpm generators with 180 slots are drawn. Both generators have the same stator bore diameter, the same slot width and the same sloth height. To the left, a generator with 14 poles is shown in comparison to the generator to the right, which is designed with 26 poles. From Fig. 7.8 it can be seen that the height of the rotor

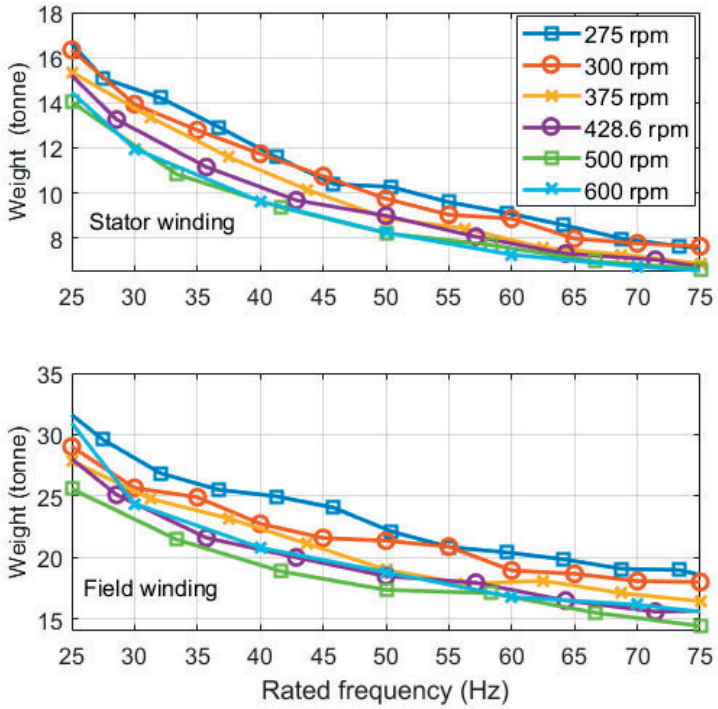

Figure 7.5: Weight of stator winding (top) and field winding (bottom).

ring is also reduced when frequency is increased.

In conclusion, as described, the total weight of active materials is reduced substantially due to the reductions in stator and rotor iron, stator and field winding weight.

7.2.2 Losses in the generator

The stator winding copper losses are presented in Fig. 7.9, including both the AC and DC copper losses. The AC, eddy current copper losses are small compared to the DC losses, but they increase slightly from 6-7 kW at the lowest rated frequencies to 22-23 kW at the highest rated frequencies. The stator copper losses remain stable over the frequency range, with the copper losses being 8-13% higher at 75 Hz than they are at 25 Hz.

There are two mechanisms that help keep the copper losses at the same level: First, when the airgap volume is increased, as was seen in Fig. 7.3, the required armature loading was found to be reduced. This result in a lower required stator current and

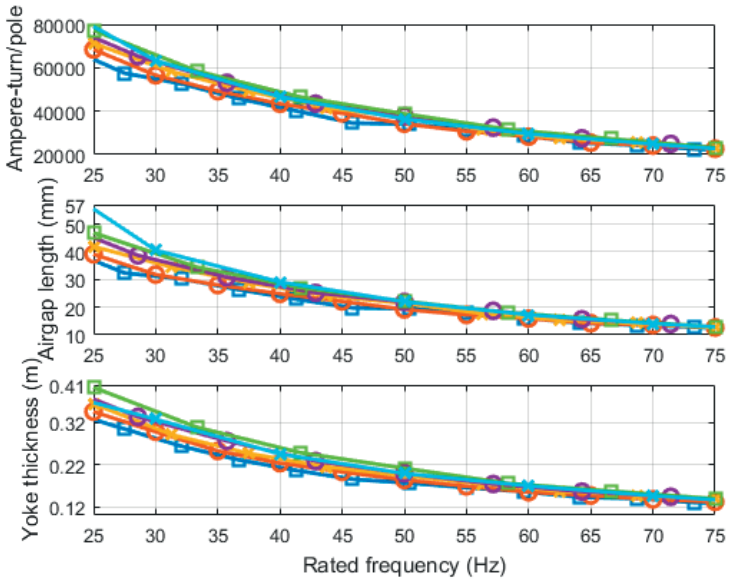

Figure 7.6: Magnetizing ampere-turns per pole (top), airgap length (middle) and stator yoke thickness (bottom) for different rated frequencies.

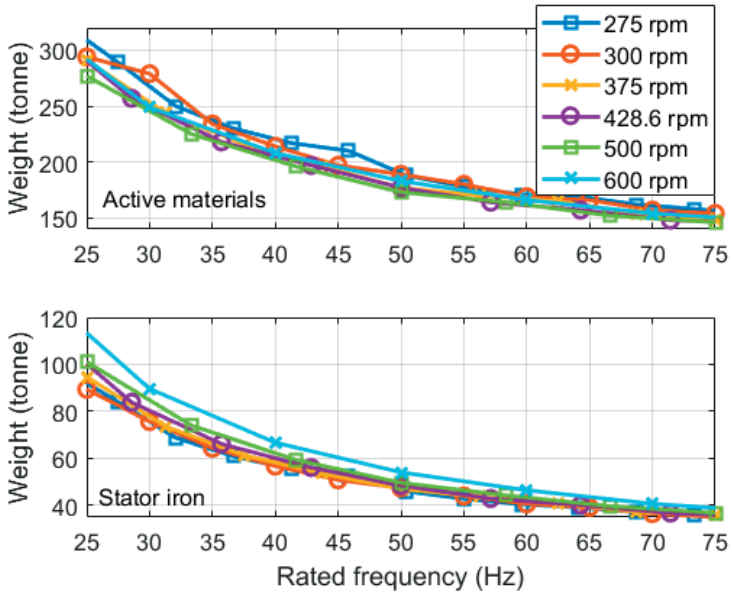

Figure 7.7: Weight of active materials (top) and weight of iron in stator (bottom).

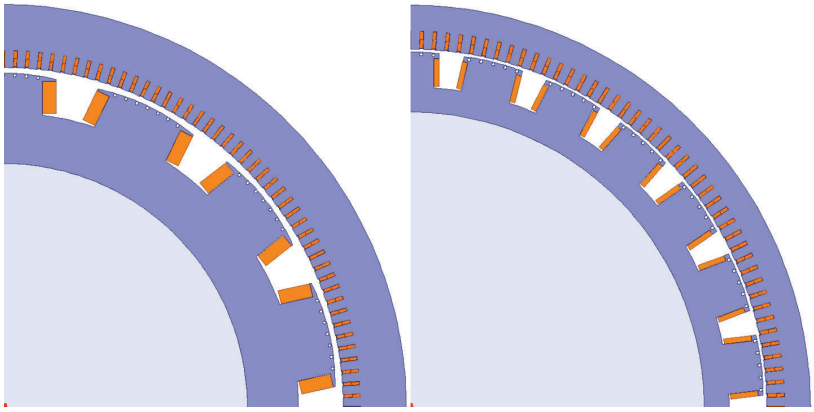

Figure 7.8: Geometries of two 275 rpm generators. Left: 14 poles. Right: 26 poles. Both generators have the same stator bore diameter, slot height, slot width and number of slots.

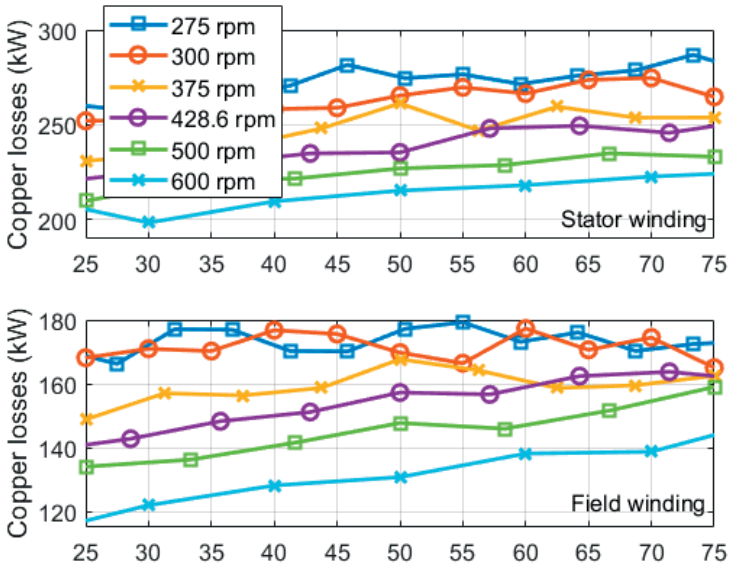

Figure 7.9: Stator copper losses (top) and field winding copper losses.

a higher stator voltage. When the stator current is reduced, the copper losses are reduced too.

The second mechanism results in the opposite effect. Since the stator current is reduced, the copper cross section needed to maintain an acceptable current density

in the winding is also reduced. When the cross section is reduced, the effective DC resistance of the winding is increased, giving an increase in the copper losses. The net effect of these two mechanisms is a slight increase in the stator copper losses at higher rated frequencies.

Copper losses in the field winding are given in Fig. 7.9. When the number of poles is increased, the necessesary number of ampere-turns per pole is reduced. This reduces the current needed, and/or the number of turns, which reduces the copper losses per pole. Increasing the number of poles increases the field winding losses. The net effect, as can be seen in Fig. 7.9, is that the field winding losses increase when the rated frequency is increased.

Based on Fig. 7.3, Fig. 7.4, and Fig. 7.9, it appears that the feasible design space for the generator running at 275 rpm is narrow. It can be seen that the axial length fluctuates more for the 275 rpm designs than what is the case for the other rotational speeds.

The electric loading in Fig. 7.4 is less stable for the 275 rpm designs. This indicates that the optimization algorithm has more difficulty finding feasible designs where the temperature requirements are met. When the electric loading is reduced the axial length must be increased in order to maintain the same output power.

The cooling issues the optimization algorithm appears to experience for the 275 rpm designs are reflected in the copper losses in Fig. 7.9, where these seems to fluctuate more for the designs running at the lowest rotational speed.

Stator iron losses are presented in Fig. 7.10. The reduction in the weight of stator iron will reduce the iron losses with a higher rated frequency, while the increased rated frequency will increase the iron losses, see (3.54). The mechanical losses, also presented in Fig. 7.10, increase when the rated frequency is increased. The main reason for this is that the mechanical losses are calculated as a function of both D and L, see (3.40). Since D^2L increases with higher rated frequency, the mechanical losses increase in turn.

The efficiency of the generator at different rotational speeds and rated frequencies are presented in Fig. 7.11. These results give us that the highest efficiency at a given speed of rotation appears to be achieved at low rated frequencies. Efficiency seems to increase for all rated frequencies above 50 Hz by increasing the speed of rotation. At the lowest rated frequencies it seems to be the case that lower rotational speeds give a higher efficiency. At frequencies above 50 Hz, the fastest rotating generators tend to have a higher efficiency than the slower rotating ones.

It can be seen that the efficiency starts to decrease for all rotational speeds as the

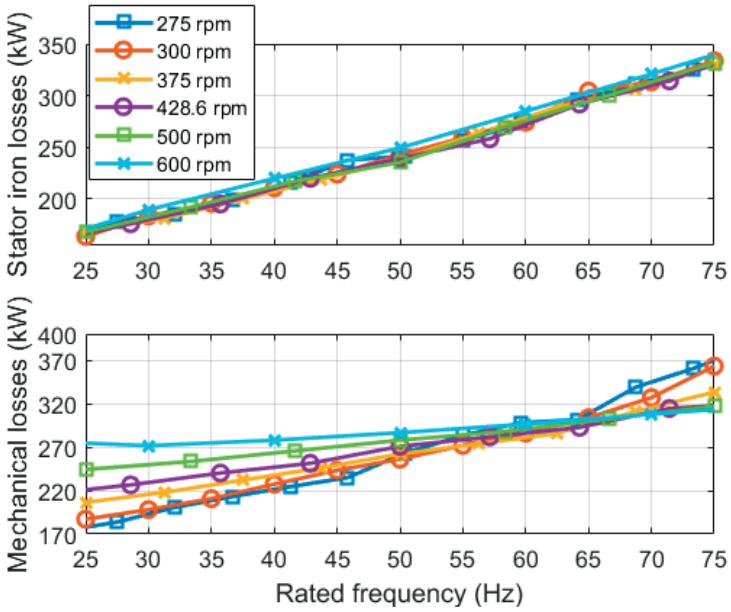

Figure 7.10: Stator iron losses (top) and mechanical losses at different rated frequencies and rotational speeds.

rated frequency is increased past 40 Hz. As was presented in Fig. 7.9, the copper losses slightly increase with frequency. The main drivers for the reduced efficiency at higher rated frequencies are found in Fig. 7.10. The mechanical and iron core losses are found to increase with frequency, which results in a reduction in the efficiency at all rotational speeds.

7.2.3 Main findings

When the number of poles is increased to increase the rated frequency the total weight of active materials in the generator is reduced. This is true for rotor and stator iron, stator copper and the copper in the field winding.

When the weight of the generator is reduced at higher rated frequencies the result is a slimmer generator with a thinner stator yoke and rotor ring. The reduction in the weight of the generator makes the cost of the materials small compared to the cost of losses as a share of the total cost.

By increasing the rated frequency the airgap volume D^2L is increased, allowing for a smaller armature loading. An effect of this is that the stator voltage is increased and that the stator current is reduced. The increase in rated frequency reduces the required airgap length to maintain the rated synchronous reactance

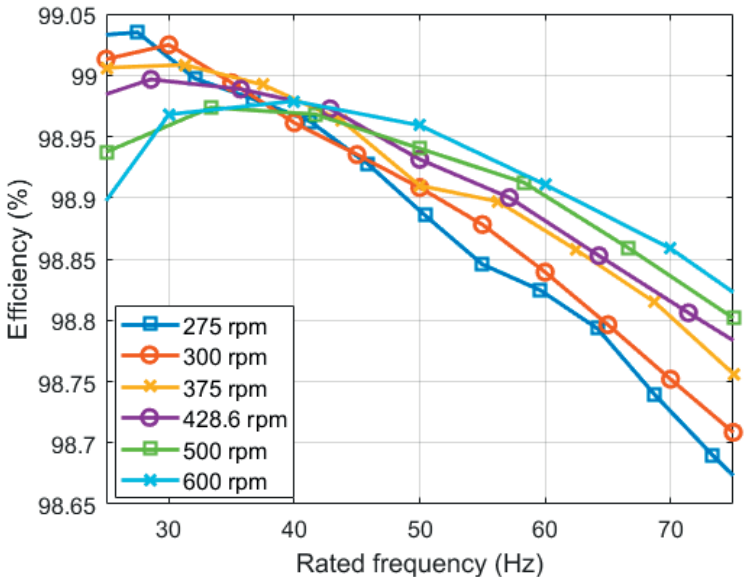

Figure 7.11: Efficiency at different speeds of rotation and rated frequency.

value, which reduces the ampere-turns needed per pole. As a product of this the field current is reduced when the rated frequency is increased.

It has been shown that the losses increase with an increase in the rated frequency. This leads to higher energy costs that increase the total cost of the generator. These results give us that the highest efficiency at a given speed of rotation appears to be achieved at low rated frequencies. Efficiency seems to increase for all rated frequencies above 50 Hz by increasing the speed of rotation. At the lowest rated frequencies it seems to be the case that lower rotational speeds give a higher efficiency. At frequencies above 50 Hz the fastest rotating generators tend to have a higher efficiency than the slower rotating ones.

It is possible to reduce the weight substantially by increasing the rated frequency. The cost is the increase in energy losses due the lower efficiency. In the end this would be a trade-off between the cost of materials and the net present value of future energy losses.

Temperature limits are set in the design specifications. Calculating the temperature distribution in the generator accurately requires detailed thermal models and accurate loss estimation [129]. It is important that the cooling capability of the cooling system is calculated accurately.

If one of these three is not calculated correctly in the design phase, the generator is likely to run with higher temperatures in normal operation than it is designed for. This may result in reduced lifetime, thermal damage to the generator, or forced operation at lower than rated loading.

Given that the temperature limits are chosen properly, and that the thermal models are correct, the main method for achieving an optimally designed generator, is to increase the capitalized value of the losses in the machine. This is done by increasing the cost of losses until the desired machine temperatures are achieved.

If the cost reduction for saving losses is larger than the cost of increasing the material usage, the optimization routine will opt for the colder generator design with a higher total weight [78].

The objective function could also be extended to include the cost of cooling systems. However, if the capitalized cost of losses has been set correctly, the resulting optimal design should be the same. For air cooled hydropower generators the cost of ventilation losses would be a major component in the modeling of the cost of the cooling system. The reason is that the main mechanism for controlling the temperature of the generator is by controlling the amount of cooling air that is sent through the generator [100].

The optimal frequency that gives the lowest total cost is reached between 40 Hz and 50 Hz. Generators with higher rotational speeds tend to have a higher optimal rated frequency.

7.3 Effects of relaxing the synchronous reactance requirement

In order to investigate how relaxing the requirement on the synchronous reactance affects the total cost of the generator, the total cost have been calculated for several upper limits. Initially, the value is set to 1.2 p.u. Then the limit is relaxed to 2.0 p.u., and finally it is removed altogether.

For the purpose of limiting the number of cases to investigate, a rotational speed of 375 rpm was chosen for the analysis of the effect of relaxing the requirement on the synchronous reactance. Three different rated frequencies, i.e. 25 Hz, 50 Hz and 75 Hz, were chosen to be studied. Some of the analysis presented in this section reinforce the findings presented in Section 7.2.

When the limit on the synchronous reactance is removed, the reactance is allowed to be optimized for each frequency. For the 25 Hz designs, the optimal value was found to be 3.3 p.u. The optimal values were found to be 2.9 p.u. for the 50 Hz designs and 2.5 for the 75 Hz designs.

The main results of of the investigation into the effect of relaxing the reactance requirement are presented in Fig. 7.12. They can be summarized the following way:

A: the total generator cost is reduced when the synchronous reactance is increased.

For the 75 Hz designs, which are the most expensive category, the cost is reduced by 4.49% when the synchronous reactance is increased from 1.2 p.u. to 2 p.u. When the reactance value is allowed to rise even higher, the cost reduction is 0.56%. For the 25 Hz designs the cost reductions are 5.62% and 2.12% respectively. For the least expensive designs, running at 50 Hz, the reductions are 5.02% and 1.49%.

Increasing the rated frequency from 25 to 50 Hz reduces the cost of the generator by 2.13%, 1.51% and 0.87% respectively for the different reactance values. Increasing the frequency from 50 to 75 Hz shows an increase in total cost of 6.68%, 7.95% and 9.66% respectively.

Fig. 7.12 presents the results from the optimization for different rated frequencies and different synchronous reactance values. The distribution of cost between losses and materials is presented. The reason for the 50 Hz designs being cheaper than the 25 Hz designs, which in turn are cheaper than the 75 Hz designs, is revealed:

1. The cost of losses is increases with rated frequency.
2. Material cost does not show the same trend.
   (a) Moving from 25 Hz to 50 Hz results in a substantial decrease in the cost of materials.
   (b) Moving from 50 Hz to 75 Hz yields only a smaller decrease in the cost of materials.

The same type of stator and rotor iron has been used for all rated frequencies. When the cost of materials becomes small relative to the total cost, it could become viable to choose more expensive, higher-grade materials. A stator iron type with lower specific losses could potentially reduce the cost of losses more than it would increase the cost of materials.

A more expensive rotor steel with higher yield strength would allow the maximum peripheral speed of the poles to increase. This would allow for a larger maximum

airgap diameter, which could have an impact on high pole designs that are limited by space for and cooling of the poles.

3. The 50 Hz designs are cheaper than the 25 Hz designs as the reduction in material costs are larger than the increase in cost of losses.
4. For the 75 Hz case the increase in cost of losses is larger than the reduction in cost of materials.
5. The 75 Hz designs are the most expensive options analyzed.

When the rated frequency increases, the cost of materials becomes smaller compared to the cost of losses. At higher frequencies the cost of losses starts to dominate the total cost of the generator. At 25 Hz the material cost is 59-62% of the cost of losses. This ratio drops to 31-32% at 50 Hz and 22-23% at 75 Hz.

Fig. 7.13 gives the relationship between required magnetization, field current and airgap length. It can be seen that the total ampere-turns per pole and the field current decreases when the airgap gets smaller. Using (3.38) it can be seen that the synchronous reactance is inversely proportional to the number of poles and the airgap length. Since the speed of rotation is constant, the number of poles must increase to increase the frequency. Increasing the number of poles or the value of the synchronous reactance necessitates a reduction in airgap length.

An increase in the synchronous reactance, reduces the required magnetization (ampere-turns), resulting in a reduction in field current. By lowering the field current, see Fig. 7.13, the rotor losses go down, as presented in Fig. 7.14. Less losses in the rotor gives less heating of the cooling air before it enters the stator. This allows the armature loading, see Fig. 7.15 to increase. The reason for this is the air that enters the stator is colder, which makes a higher temperature increase in the air that passes the stator winding possible.

Increasing the armature loading A reduces the magnetic loading B_δ, see Fig. 7.15. According to (3.7), when the product of A and B_δ goes up, the required airgap volume D^2L goes down, see Fig. 7.16. This leads to a shorter machine , see Fig. 7.16. As the diameter is primarily determined by the number of poles, and the length L is reduced, the weight of iron in the rotor and stator goes down. This is presented in Fig. 7.17.

The geometries of two optimized 50 Hz generators are presented in Fig. 7.18. Here, it can be seen that the 2.0 p.u. synchronous reactance generator has a shorter airgap, thinner stator and rotor yokes and higher number of stator slots. The generator with 2.0 p.u. synchronous reactance has a higher number of stator slots that

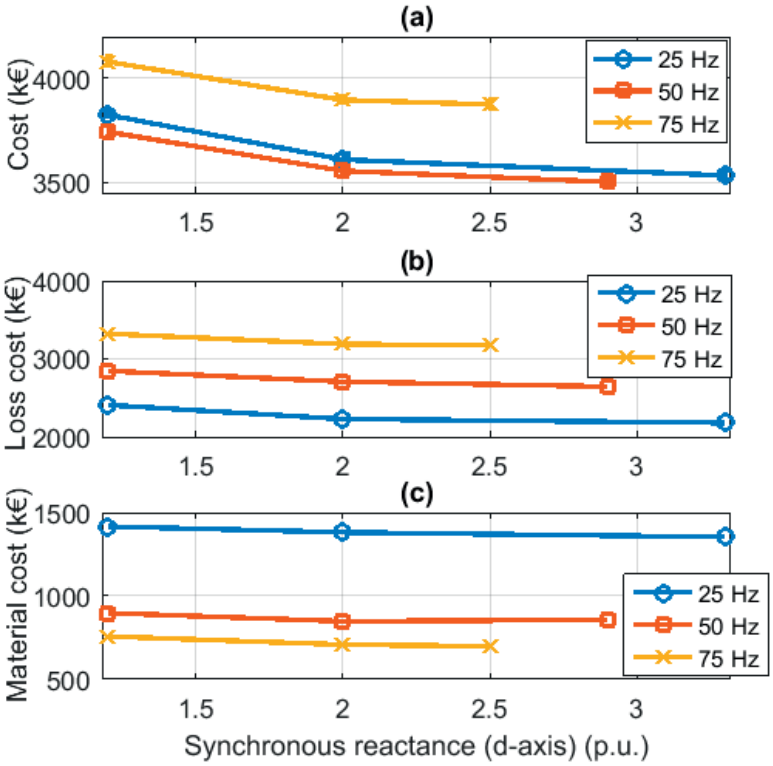

Figure 7.12: Comparison of material and loss cost for different frequencies, (a) total cost, (b) loss cost, (c) material cost.

increases the armature loading in the machine. The main parameters of the two generators are presented in Table 7.1. It can be observed that the armature loading is higher for the 2.0 p.u. generator, and that the weight of rotor and stator iron is reduced when the synchronous reactance is increased.

Losses in the generator are presented in Fig. 7.14. It can be seen that both iron losses and mechanical losses go down when the synchronous reactance is increased. This can be attributed to the reduction in axial length as a result of the increased armature loading. From (3.7) we have that when A is increased, the necessary length L goes down. Mechanical losses increase with increasing frequency as a consequence of a larger generator diameter. For the 50 Hz designs, the increased diameter has a larger effect on the mechanical losses than the shorter length has.

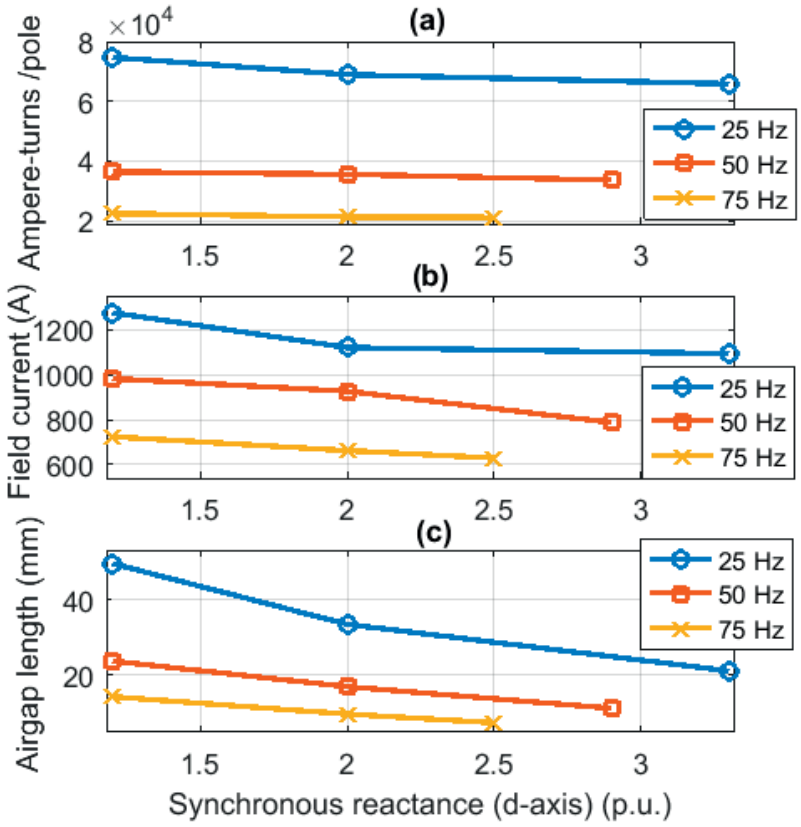

Figure 7.13: Magnetization of the generator, (a) ampere-turns per pole, (b) field current, (c) airgap length.

Rotor losses are reduced when the synchronous reactance or the frequency is increased. This is both due to the reduction in field current mentioned earlier and because of an increase in the copper cross section giving a reduced field winding resistance. Additional losses increase when the airgap length is reduced due to more losses in the pole surface.

Fig. 7.19 presents the relationship between pole surface losses and the ratio of airgap length to slot opening. This figure indicates that pole surface losses are kept small when the airgap length to stator slot opening ratio is kept below 1.0.

Airgap length to slot opening is reduced when the synchronous reactance or rated frequency is increased, see Fig. 7.19. The main reason for this is that the length of the airgap is reduced when the rated frequency or the synchronous reactance is

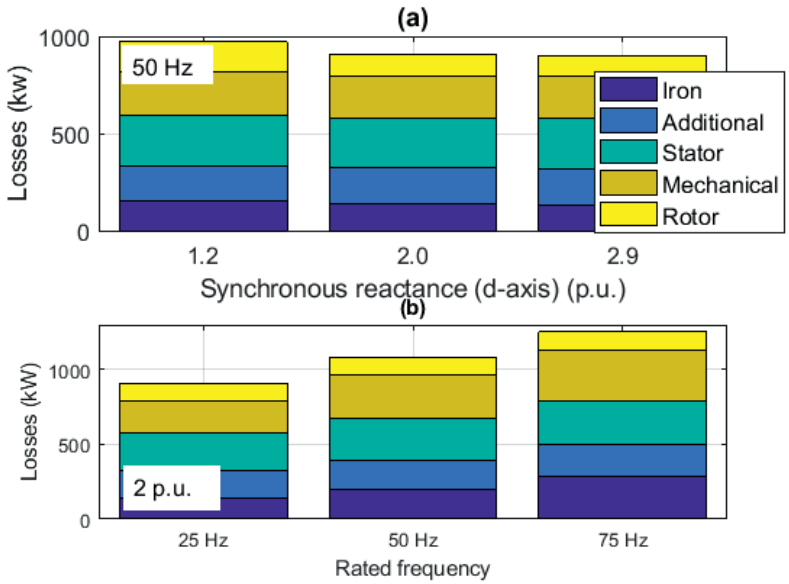

Figure 7.14: Losses in the generator, (a) at 50 Hz, (b) at 2.0 p.u. synchronous reactance.

increased.

Pole surface losses are increased to more than 2600 $\mathrm{W/m^2}$ at the smallest airgap length to slot opening ratio. When this ratio is reduced, the flux pulsations in the pole surface increase, leading to increased losses.

The airgap length is inversely proportional to the rated frequency. Pole surface losses are proportional to the value of the synchronous reactance (3.58), meaning that the pole surface losses are proportional to the rated frequency. When the frequency increases, the airgap length is reduced, resulting in a smaller airgap length to slot opening ratio. This leads to increased pole surface losses. In conclusion, the pole surface losses increase when the rated frequency or the synchronous reactance increase.

7.3.1 Main findings

When moving from one rated frequency to another, two counter-acting cost effects are observed. Increasing the frequency will increase the losses and with it the capitalized cost of losses. When working to reduce the total cost, an increase in nominal frequency reduces the amount of active materials needed, reducing the cost of materials. When the rated frequency was increased from 25 Hz to 50 Hz,

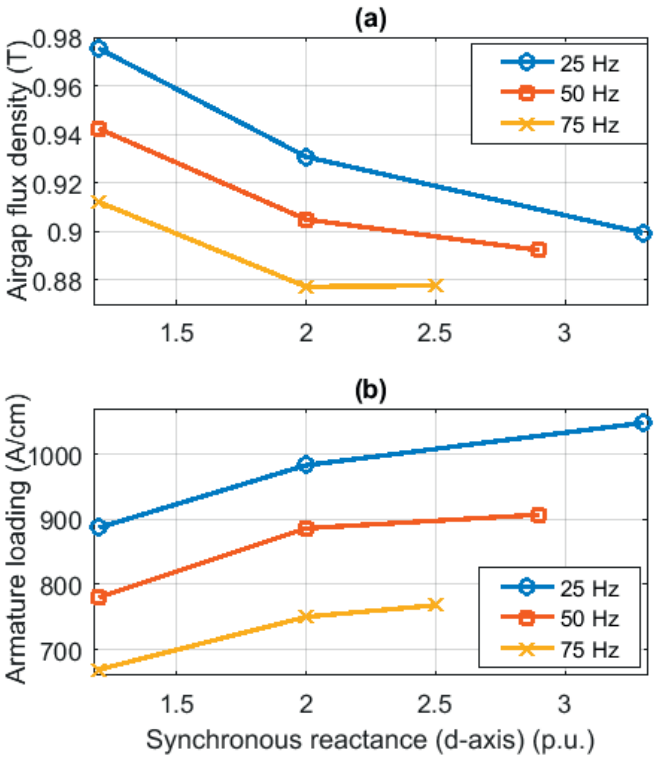

Figure 7.15: Loading of the generator, (a) magnetic loading, (b) electric loading.

Table 7.1:
Design results from optimization (50 Hz)

	Synchronous reactance	1.2 p.u.:	2.0 p.u.:
	Cost	3699.6 k€	3535.9 k€
	Total weight	162076 kg	144594 kg
	Independent variables:		
Q_s	Number of stator slots	144	192
D	Stator bore (m)	3.85	4.03
n_v	Number of cooling ducts	50	41
b_u	Width of stator slot (mm)	28.8	24.8
n_{str}	Number of strands per stator slot	63	67
b_{pc}	Pole core width (mm)	379	383
n_f	Number of turns per pole	36	36
b_{cuf}	Width of field winding (mm)	127	145.3
δ_0	Airgap length (mm)	23.6	17.8
h_{cus}	Height of Roebel bar strand (mm)	1.6	1.6
h_{cuf}	Height of field winding turn (mm)	4.0	4.0
	Machine parameters:		
L	Length	2.34 m	1.93 m
η	Efficiency	98.85 %	98.87 %
U_n	Stator line voltage	9.012 kV	10.048 kV
A	Armature loading	801 A/cm	916 A/cm
B_δ	Airgap flux density	0.93 T	0.88 T
$m_{cu,stator}$	Stator copper weight	9819 kg	10256 kg
$m_{cu,rotor}$	Rotor copper weight	15894 kg	15895 kg
$m_{iron,stator}$	Stator iron weight	60593 kg	51813 kg
$m_{iron,rotor}$	Rotor iron weight	75770 kg	66630 kg
X'_d	Transient reactance	0.24 p.u.	0.32 p.u.
X''_d	Subtransient reactance	0.18 p.u.	0.24 p.u.

the reduction in the cost of materials was greater than the increase in loss cost. This made the 50 Hz designs cheaper than the 25 Hz designs.

Moving from 50 Hz to 75 Hz reduced the cost of materials less than the increase in

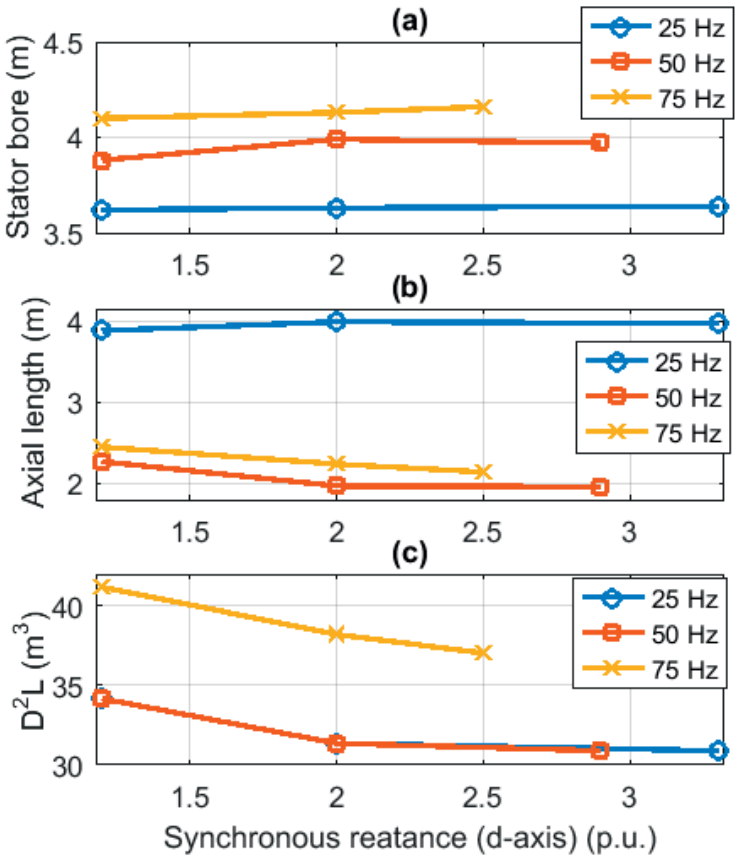

Figure 7.16: Main dimensions of the generator, (a) stator bore, (b) axial length, (c) rotor volume.

the cost of losses, giving an increase in the total generator cost. For the three rated frequencies tested in this section, the 50 Hz designs had a lower total cost than the 25 Hz and 75 Hz designs. These results correspond well with the results presented in Section 7.2.

For the 75 Hz designs, the cost of losses is large compared to the cost of materials. The same type of stator and rotor iron has been used for all rated frequencies. When the cost of materials becomes small compared to the total cost, it could become viable to choose higher-grade materials that are more expensive. A stronger, more expensive type of rotor steel could have allowed a higher periphery speed for the poles, which would have increased the maximum airgap diameter. A higher maximum airgap dameter could have made an impact on the optimal design for

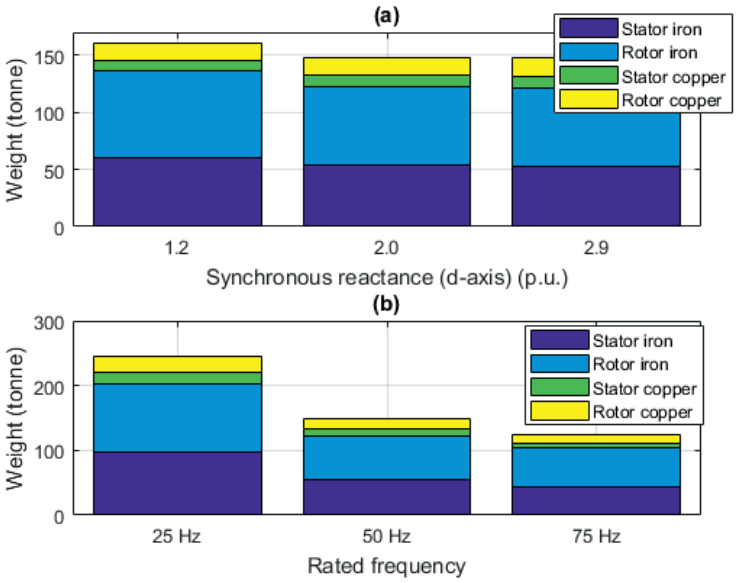

Figure 7.17: Weight of the generator, (a) at 50 Hz, (b) at 2.0 p.u. synchronous reactance.

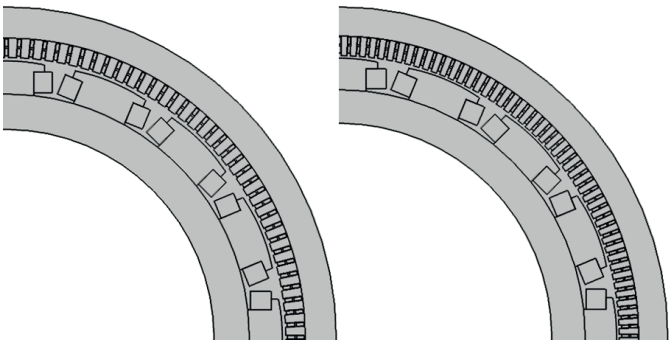

Figure 7.18: Geometries of two 50 Hz generators. Left: 1.2 p.u. synchronous reactance. Right: 2.0 p.u. synchronous reactance.

the high pole designs where space and cooling limit the optimal design.

If a rated frequency of 75 Hz would have been chosen, it is likely that a higher quality stator iron with lower specific losses should have been chosen. By choosing an iron type with lower specific losses, the cost of materials will increase, but the cost of losses would decrease. It is likely that the cost of losses would decrease more than the cost of materials would increase, leading to a lower total generator

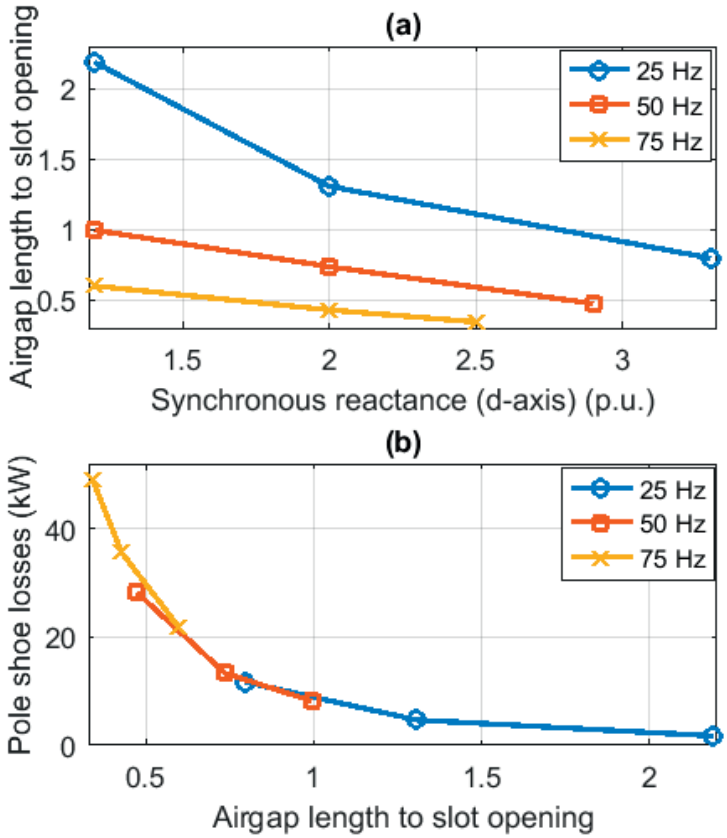

Figure 7.19: Pole surface losses, (a) airgap length to slot opening, (b) pole surface loss estimate.

cost. This, in turn, would reduce the gap in total cost between the 75 Hz designs and the 25 Hz and 50 Hz designs, making the 75 Hz designs more attractive and possibly pushing the optimal rated frequency above 50 Hz.

Increasing the value of the synchronous reactance from 1.2 p.u. to 2 p.u. reduces the total generator cost with 4.49-5.62%. The lower the rated frequency, the higher the cost reduction. This can be attributed to the length of the airgap, in that a larger reduction in airgap length gives a larger cost reduction.

Increasing the synchronous reactance 2 p.u. gives a smaller cost reduction and several possible design issues, including increasing losses and radial forces. When the upper limit on the synchronous reactance was removed, the cost was reduced 0.56-2.12%. The cost benefits of increasing the synchronous reactance must be

weighed against possible design issues.

Based on the results presented here, it seems to be most beneficial to increase the synchronous reactance to 2.0 p.u. If the generator is to be operated directly connected to the grid, a stability analysis should be performed in order to make sure that stable operation is maintained.

7.4 Conclusions

This chapter has investigated how the rated frequency affects total cost, total weight and generator efficiency using the converter-fed synchronous machine topology. The speed of rotation has been varied between 275 rpm and 600 rpm, while the rated frequency used was held between 25 and 75 Hz.

The main findings are:

1. The weight of the generator is reduced when the rated frequency is increased. A higher rated frequency gives a lighter generator with a lower cost for the active materials.
2. The losses in the machine increases when the rated frequency increases, increasing the cost of losses.
3. The optimal frequency that gives the lowest total cost is reached between 40 Hz and 50 Hz. Generators with higher rotational speeds tend to have a higher optimal rated frequency.

The results indicates that the highest efficiency at a given speed of rotation is achieved at low rated frequencies. Efficiency seems to increase for all rated frequencies above 50 Hz by increasing the speed of rotation. At the lowest rated frequencies it seems to be the case that lower rotational speeds give a higher efficiency. At frequencies above 50 Hz the fastest rotating generators tend to have a higher efficiency than the slower rotating ones.

A rotational speed of 375 rpm with 16 poles, which is the most common in Norway, was selected for the investigation of the effect of relaxing the requirement on the synchronous reactance. For the given generator specifications - 25 Hz, 50 Hz and 75 Hz were used as rated frequencies in the optimization. The main conclusions of the investigation are:

1. The total generator cost is reduced when the synchronous reactance is increased.
2. The same trend is observed for all the three rated frequencies that were used.

The designs using 50 Hz were found to be cheaper than all other designs. Moving from 25 Hz to 50 Hz reduces the cost of materials more than the cost of losses are increased. When moving from 50 Hz to 75 Hz, the reduction in materials' cost is smaller than the increase in the cost of losses.

Increasing the synchronous reactance from 1.2 p.u to 2.0 p.u. reduced the total cost of the generator. The largest cost reduction was achieved with the lowest rated frequency.

Increasing the synchronous reactance above 2.0 p.u. led to a smaller reduction in total cost than the reduction achieved by relaxing the upper reactance limit from 1.2 p.u. to 2.0 p.u. Several design issues might become apparent when the synchronous reactance is increased. The benefit of cost reduction must be weighed against the negative effects, like increased losses and reduced grid stability, when the final value of the synchronous reactance is chosen.

If the value of the synchronous reactance is increased it may cause some stability issues if the generator is going to be able to operate directly connected to the grid. In that case it would be necessary to perform a stability analysis to see how well the generator is able to perform as a regular, grid connected generator.

Increasing the value of the synchronous reactance from 1.2 p.u. to 2.0 p.u. has been shown to reduce the total cost of the generator. This reduction in cost can help offset parts of the cost of the converter that is associated with having a converter-fed synchronous hydrogenerator in pumped-storage plants. This, in turn, can make variable-speed pumped storage plants more cost-competitive versus traditional fixed-speed solutions.

Chapter 8

Conclusions

The power system is experiencing an increasing share of electric power production from intermittent power sources like wind and solar energy. Increased pressure is put on controllable production units like hydropower plants to deal with fluctuations in output of electric power production. The flexibility of the hydropower plants can be enhanced by introducing variable speed operation to large hydropower generators through the converter-fed synchronous machine topology.

The main benefits of enabling variable speed operation can be summarized as the ability to control active power in pumping mode, improved efficiency at part load and improved efficiency when there is a large variation in discharge or head during operation.

In cases where a converter-fed synchronous machine solution is used instead of the traditional fixed-speed, grid-connected, synchronous generator the rated frequency of the generator can be chosen independently of the grid frequency. The requirements on the synchronous reactance value can also be relaxed in converter-fed operation without losing stability. It is concluded that:

- The optimal rated frequency that gives the lowest total cost is reached between 40 Hz and 50 Hz.
- Increasing the value of the synchronous reactance from 1.2 p.u. to 2.0 p.u. reduces the total cost of the generator.

The reduction in cost can help offset parts of the cost of the converter that are associated with having a converter-fed synchronous hydrogenerator in pumped-

storage plants. This, in turn, can make variable-speed pumped storage plants more cost-competitive versus traditional fixed-speed solutions.

If the value of the synchronous reactance is increased it may cause some stability issues if the generator is going to be able to operate directly when connected to the grid. In that case it would be necessary to perform a stability analysis to see how well the generator is able to perform as a regular, grid connected generator.

The lowest mode of vibration of three hydropower generators has been studied. For all the generators investigated, the lowest mode of vibration is the second spatial harmonic. It is found that the lowest mode of vibration is primarily produced by the main flux density harmonic component and its adjacent harmonic components.

It is found that reducing the airgap leads to a less than proportional increase in the lowest order radial force component. The reason for this is that the reduction in airgap length is causing increased saturation in the generator.

Damperbars are able to reduce the lowest order radial force component by between 20-40% compared to the case without damperbars. The damperbars are able to reduce the lowest order force component more efficiently when the airgap length is reduced. Losses in the damperbars themselves are increased when the airgap length is reduced.

In cases where low order radial forces cause vibration problems, the problem can be significantly reduced by rearranging the winding configuration. It is demonstrated that lowest order radial force component can be reduced by more than 60% by rearranging the winding layout.

The modeling and analysis of losses in large hydropower generators has been a major focus in this work, both the additional losses produced by converter-operation and the modeling of the losses in the stator iron.

The effect of converter operation on AC copper loss in large hydrogenerators has been investigated. Current harmonics produced by switching in two- and three-level converters increase the AC copper losses in traditionally designed stator windings in large hydrogenerators. These additional losses could cause intolerable heating and probably destroy the windings.

If a generator is going to be built for converter operation using a two-level or a three-level topology like the ones that are available today, it is found that:

- The strand thickness would have to be reduced compared to traditional designs.
- If this is not possible, a filter between the converter and the generator must be used.

Including damperbars in a converter-fed synchronous hydropower generator increases the AC copper losses in the stator. In addition to this, the losses in the damperbars themselves increase substantially. As a consequence:

- It is advised against using damperbars, if possible, when two- or three-level converter topologies are used.

The results indicate that an increase in the iron core loss in the range of 10-30% can be expected using traditional two- and three-level converter topologies. More detailed analysis and modeling is needed in order to conclude on the effect of converter-operation on stator core losses.

Based on the investigation into the additional copper and iron losses in converter operation, the benefits of using a multi-level converter topology should be investigated further.

Experimental work has been presented for a generator test setup. Losses have been measured at different levels of magnetization and at different rotational speeds. Mechanical losses and core losses are estimated from measurements. Experimental results have been used to verify the loss calculations used in this thesis.

Stator core losses have been predicted using the Bertotti method and the Vector-Preisach model for two hydropower generators, in addition to the generator test setup. The Bertotti method gives a core loss prediction that is close to the reference value for both the large generators, and to the measured losses in the generator test setup. Good core loss estimates are achieved with the Bertotti method for different power ratings and design types.

Using the Vector-Preisach model is not found to improve the core loss prediction significantly. The model is found to be more sensitive to saturation than the Bertotti method.

Different correction factors for the stator core losses have been applied in order to discover which values should be used optimally. The Bertotti method is shown to give more consistent core loss predictions using correction factors than the Vector-Preisach model. It is not conclusive which correction factor gives the best loss prediction, it must be decided on a case-by-case basis.

8.1 Future work

The analysis on radial forces would have been strengthened if measurements of low order radial force could have been performed. For example, it would have been interesting to see if the same difference in the lowest order radial force component with and without damperbars that was found with simulations could have been observed in an experimental setup.

By measuring the currents and losses in the damperbars in both sinusoidal and converter-fed operation the analysis on damperbar losses and the effect of converter operation could have been further enhanced. The same applies to measurements of iron core losses during converter operation.

More studies should be performed and better core loss estimation methods should be investigated in order to conclude on the effect of converter operation on core losses in hydropower generators

In the analysis on the optimal design of hydropower generators for variable speed operation only the operation at rated output was studied. A study into the optimal operation at off-design conditions should have been conducted. Here, turbine data and the operational profile of a realistic case would be needed to shed more light on the benefits of variable speed operation.

Bibliography

[1] L. Lia, T. Stensby, K. E. Midttømme, G. Holm, and A. M. Ruud, "The current status of hydropower development and dam Construction in Norway," *International journal on hydropower and dams*, no. 3, pp. 37–43, 2015.

[2] R. Perers, U. Lundin, and M. Leijon, "Development of synchronous generators for Swedish hydropower: A review," *Renewable and Sustainable Energy Reviews*, vol. 11, no. 5, pp. 1008–1017, 2007.

[3] The Norwegian Water Resources and Energy Directorate (NVE), *Overview of Norway's Electricity History*. NVE, 2017.

[4] J. M. Merino and A. Lopez, "ABB Varspeed generator boosts efficiency and operating flexibility of hydropower plant," *ABB Review*, no. 3, pp. 33–38, 1996.

[5] D. Schafer and J. J. Simond, "Adjustable speed asynchronous machine in hydro power plants and its advantages for the electric grid stability," *CIGRÉ*, 1998.

[6] A. Bocquel and J. Janning, "Analysis of a 300 MW variable speed drive for pump-storage plant applications," in *2005 European Conference on Power Electronics and Applications (EPE)*, 2005, pp. P.1 – P.10.

[7] P. March, W. Moore, and M. Nesbitt, "Flexible Operation of Hydroelectric Turbines and Generators," *HydroVision International conference 2018*, 2018.

[8] R. J. Kerkman, T. A. Lipo, W. G. Newman, and J. E. Thirkell, "An Inquiry into Adjustable Speed Operation of a Pumped Hydro Plant Part 1 - Ma-

chine Design and Performance," *IEEE Transactions on Power Apparatus and Systems*, vol. PAS-99, no. 5, pp. 1828–1837, 1980.

[9] CIGRÉ, "Guide for preliminary design and specification of hydro stations with HVDC unit connected generators," Tech. Rep., 1997.

[10] G. Galasso, "Adjustable speed operation of pumped hydroplants," in *International Conference on AC and DC Power Transmission*, 1991, pp. 424–427.

[11] G. D. Ciocan, O. Teller, and F. Czerwinski, "Variable speed pump-turbines technology," *UPB Scientific Bulletin, Series D: Mechanical Engineering*, vol. 74, no. 1, pp. 33–42, 2012.

[12] MWH Americas Inc., "Technical analysis of pumped storage and integration with wind power in the pacific northwest," *Technical report, MWH-HDC-T12*, 2009.

[13] J. A. Baroudi, V. Dinavahi, and A. M. Knight, "A review of power converter topologies for wind generators," *Renewable Energy*, vol. 32, no. 14, pp. 2369–2385, 2007.

[14] R. Raja Singh, T. Raj Chelliah, and P. Agarwal, "Power electronics in hydro electric energy systems - A review," *Renewable and Sustainable Energy Reviews*, vol. 32, pp. 944–959, 2014.

[15] M. Tazil, V. Kumar, R. C. Bansal, S. Kong, Z. Y. Dong, W. Freitas, and H. D. Mathur, "Three-phase doubly fed induction generators: an overview," *IET Electric Power Applications*, vol. 4, no. 2, pp. 75–89, 2010.

[16] Energy Storage Association, "Variable Speed Pumped Hydroelectric Storage, Accessed May 26, 2019." [Online]. Available: energystorage.org/energy-storage/technologies/variable-speed-pumped-hydroelectric-storage

[17] International Hydropower Association, "Pumped Storage Tracking Tool, Accessed: May 26, 2019." [Online]. Available: https://www.hydropower.org/hydropower-pumped-storage-tool

[18] Ø. J. Linnebo, "Turtallstyring og lastkontroll av pumpeaggregater (In Norwegian)," in *Produksjonsteknisk konferanse (PTK)*, 2013.

[19] N. Mohan, T. M. Undeland, and W. P. Robbins, *Power electronics: converters, applications, and design*. John Wiley & Sons, 2003.

[20] G. J. Neidhofer and A. G. Troedson, "Large converter-fed synchronous motors for high speeds and adjustable speed operation: design features and experience," in *IEEE Transactions on Energy Conversion*, vol. 14, no. 3, 1997, pp. MA2/6.1–MA2/6.3.

[21] ABB, "Grimsel 2, Switzerland - The world's largest power converter for variable speed pumped hydropower," *ABB case note*, 2014.

[22] G. C. Stone and I. Culbert, "Review of stator insulation problems in medium voltage motors fed from voltage source PWM drives," in *International Symposium on Electrical Insulating Materials (ISEIM)*, 2014, pp. 50–53.

[23] HydroFlex, "Increasing the value of Hydropower through increased Flexibility, Joint European Research Program, Accessed: May 24, 2019." [Online]. Available: https://www.h2020hydroflex.eu

[24] P. K. Steimer, O. Senturk, S. Aubert, and S. Linder, "Converter-fed synchronous machine for pumped hydro storage plants," in *2014 IEEE Energy Conversion Congress and Exposition (ECCE)*, 2014, pp. 4561–4567.

[25] H. Schlunegger and A. Thöni, "100 MW full-size converter in the Grimsel 2 pumped-storage plant," in *Hydro 2013 conference*, Innsbruck, 2013.

[26] J. M. Henry, F. Maurer, J.-L. Drommi, and T. Sautereau, "Converting to Variable Speed at a Pumped-Storage Plant," *Hydro Review Worldwide*, vol. 21, no. 1, 2013.

[27] A. Schwery, E. Fass, J.-M. Henry, W. Bach, and A. Mirzaian, "Pump storage plants - ALSTOM's long experience and technological innovation," in *Hydro 2005 conference*, Villach, 2005.

[28] J. Janning and A. Schwery, "Next generation variable speed pump-storage power stations," in *13th European Conference on Power Electronics and Applications (EPE)*, 2009, pp. 1–10.

[29] T. Lugand, "Contribution to the Modeling and Optimization of the Double-Fed Induction Machine for Pumped-Storage Hydro Power Plant Applications," Ph.D. dissertation, Université de Grenoble, 2013.

[30] A. J. Korn, M. Winkelnkemper, and P. Steimer, "Low output frequency operation of the Modular Multi-Level Converter," in *2010 IEEE Energy Conversion Congress and Exposition (ECCE)*, 2010, pp. 3993–3997.

[31] R. M. Calfo, J. A. Fulmer, and J. E. Tessaro, "Generators for use in electric marine ship propulsion systems," in *2002 IEEE Power Engineering Society Summer Meeting*, 2002, pp. 254–259.

[32] I. Boldea, *Synchronous generators*, 2nd ed. CRC Press, 2015.

[33] O. W. Andersen, "Optimum design of electrical machines," *Dr. Ing. dissertation, Chalmers University of Technology*, 1969.

[34] ——, "Optimized Design of Salient Pole Synchronous Generators," in *International Conference on Electrical Machines 2000 (ICEM'00)*, 2000, pp. 987–989.

[35] E. L. Engevik, A. Røkke, and R. Nilssen, "Evaluating Hybrid Optimization Algorithms for Design of a Permanent Magnet Generator," in *Intl Conference on Optimization of Electrical & Electronic Equipment (OPTIM) & 2015 Intl Symposium on Advanced Electromechanical Motion Systems (ELECTROMOTION), 2015 Intl Aegean Conference on Electrical Machines & Power Electronics (ACEMP), 2015*, 2015, pp. 711–718.

[36] Y. Guan, Z. Q. Zhu, G. J. Li, Z. Azar, A. S. Thomas, F. Vedreno-Santos, and M. Odavic, "Influence of Pole Number and Stator Outer Diameter on Volume, Weight, and Cost of Superconducting Generators with Iron-Cored Rotor Topology for Wind Turbines," *IEEE Transactions on Applied Superconductivity*, vol. 27, no. 6, 2017.

[37] A. Røkke, "Permanent Magnet Generators for Marine Current Tidal Turbines," Ph.D. dissertation, Norwegian University of Science and Technology, 2017.

[38] A. B. M. Aguiar, A. Merkhouf, C. Hudon, and K. Al-Haddad, "Influence of the Variation of the Input Parameters on the Simulation Results of a Large Hydrogenerator," *IEEE Transactions on Industry Applications*, vol. 50, no. 1, pp. 261–268, 2014.

[39] C. E. Stephan and Z. Baba, "Specifying a turbogenerator's electrical parameters guided by standards and grid codes," in *2001 IEEE International Electric Machines and Drives Conference (IEMDC)*, 2001, pp. 63–68.

[40] J. M. Fogarty, "Connections between generator specifications and fundamental design principles," in *2001 IEEE International Electric Machines and Drives Conference (IEMDC)*, 2001, pp. 51–56.

[41] N. Stranges and J. H. Dymond, "How design influences the temperature rise of motors on inverter drives," *IEEE Transactions on Industry Applications*, vol. 39, no. 6, pp. 1584–1591, 2003.

[42] M. Valavi, E. Devillers, J. Le Besnerais, A. Nysveen, and R. Nilsen, "Influence of Converter Topology and Carrier Frequency on Airgap Field Harmonics, Magnetic Forces, and Vibrations in Converter-Fed Hydropower Generator," *IEEE Transactions on Industry Applications*, vol. 54, no. 3, pp. 2202–2214, 2018.

[43] S. Iwasaki, R. P. Deodhar, Y. Liu, A. Pride, Z. Q. Zhu, and J. J. Bremner, "Influence of PWM on the proximity loss in permanent-magnet brushless AC machines," *IEEE Transactions on Industry Applications*, vol. 45, no. 4, pp. 1359–1367, 2009.

[44] M. J. Islam, H. V. Khang, A. K. Repo, and A. Arkkio, "Eddy-current loss and temperature rise in the form-wound stator winding of an inverter-fed cage induction motor," *IEEE Transactions on Magnetics*, vol. 46, no. 8, pp. 3413–3416, 2010.

[45] M. J. Islam and A. Arkkio, "Effects of pulse-width-modulated supply voltage on eddy currents in the form-wound stator winding of a cage induction motor," *IET Electric Power Applications*, vol. 3, no. 1, pp. 50 – 58, 2009.

[46] O. Drubel, *Converter applications and their influence on large electrical machines*. Springer-Verlag, 2013.

[47] T. Pham, S. Salon, W. Akaishi, and M. Debortoli, "Damper bar heating in hydro generators with fractional slot windings," *2017 IEEE International Electric Machines and Drives Conference (IEMDC)*, pp. 1–8, 2017.

[48] Y. Lu, J. Liu, L. Zhou, and H. Kang, "Analytical calculation of damper winding losses in large hydrogenerators," in *2014 17th International Conference on Electrical Machines and Systems (ICEMS)*, 2014, pp. 373–377.

[49] M. Ranlöf and U. Lundin, "The rotating field method applied to damper loss calculation in large hydrogenerators," in *2010 XIX International Conference on Electrical Machines (ICEM)*, 2010, pp. 1–6.

[50] G. Traxler-Samek, T. Lugand, and A. Schwery, "Additional Losses in the Damper Winding of Large Hydrogenerators at Open-Circuit and Load Conditions," *IEEE Transactions on Industrial Electronics*, vol. 57, no. 1, pp. 154–160, 2010.

[51] *IEC 60034-2-1 Rotating electrical machines - Part 2-1: Standard methods for determining losses and efficiency from tests (excluding machines for traction vehicles)*.

[52] A. B. M. Aguiar, A. Merkhouf, K. Al-Haddad, and C. Hudon, "Electromagnetic modelling of existing large hydro generator," in *2011 IEEE International Electric Machines & Drives Conference (IEMDC)*, 2011, pp. 389–393.

[53] A. B. M. Aguiar, "Electromagnetic modeling of large hydro generators using 2D finite element method," Ph.D. dissertation, École de Technologie Supérieure, Université Du Québec, 2014.

[54] M. Bergeron, J. Cros, J. Niehenke, J. R. Figueroa, and C. Messier, "Hydro generator damper bar current measurement at Wanapum Dam," *IEEE Transactions on Energy Conversion*, vol. 31, no. 4, pp. 1510–1520, 2016.

[55] A. Z. Gbégbé, B. Rouached, J. Cros, M. Bergeron, and P. Viarouge, "Damper Currents Simulation of Large Hydro-Generator Using the Combination of FEM and Coupled Circuits Models," *IEEE Transactions on Energy Conversion*, vol. 32, no. 4, pp. 1273–1283, 2017.

[56] P. Rasilo, A. Belahcen, and A. Arkkio, "Effect of Rotor Pole-Shoe Construction on Losses of Inverter-Fed Synchronous Motors," *IEEE Transactions on Industry Applications*, vol. 50, no. 1, pp. 208–217, 2014.

[57] P. Rasilo, A. Salem, A. Abdallh, F. De Belie, L. Dupré, and J. A. Melkebeek, "Effect of Multilevel Inverter Supply on Core Losses in Magnetic Materials and Electrical Machines," *IEEE Transactions on Energy Conversion*, vol. 30, no. 2, pp. 736–744, 2015.

[58] G. Bertotti, "General Properties of Power Losses in Soft Ferromagnetic Materials." *IEEE Transactions on Magnetics*, vol. 24, no. 1, pp. 621–630, 1987.

[59] G. Bramerdorfer and D. Andessner, "Accurate and Easy to Obtain Iron Loss Model for Electric Machine Design," *IEEE Transactions on Industrial Electronics*, vol. 64, no. 3, pp. 2530–2537, 2017.

[60] A. Krings, "Iron losses in electrical machines - Influence of material properties , manufacturing processes , and inverter operation," Ph.D. dissertation, KTH Royal Institute of Technology, 2014.

[61] L. Chang, T. M. Jahns, and R. Blissenbach, "Generalized Dynamic Hysteresis Model for Improved Iron Loss Estimation of Complex Flux Waveforms," *IEEE Transactions on Magnetics, (Early Access)*, pp. 1–13, 2019.

[62] M. Fratila, A. Benabou, and M. Dessoude, "Iron Loss Calculation in a Synchronous Generator," *IEEE Transactions on Energy Conversion*, vol. 32, no. 2, pp. 640–648, 2017.

[63] A. B. M. Aguiar, A. Merkhouf, and K. Al-haddad, "Open-Circuit and Short-Circuit Core Losses Computation in a Large Hydro Generator," in *39th Annual Conference of the IEEE Industrial Electronics Society (IECON)*, 2013, pp. 1–5.

[64] A. B. M. Aguiar, A. Merkhouf, and K. Al-Haddad, "A new approach for computation of magnetic core losses in large hydro electrical generator," in *39th Annual Conference of the IEEE Industrial Electronics Society (IECON)*, 2013, pp. 2506–2511.

[65] J. H. Walker, *Large synchronous machines: design, manufacture, and operation*. Oxford: Clarendon Press, 1981.

[66] P. A. Hargreaves, B. C. Mecrow, and R. Hall, "Calculation of iron loss in electrical generators using finite-element analysis," *IEEE Transactions on Industry Applications*, vol. 48, no. 5, pp. 1460–1466, 2012.

[67] J. C. Akiror, "Rotational Core Losses in Hydro Generators," Ph.D. dissertation, Concordia University, 2016.

[68] T. A. Lipo, *Introduction to AC Machine Design*. John Wiley & Sons, 2017.

[69] L. Vandenbossche, S. Jacobs, T. Lugand, and A. Schwery, "Improved Calculation of Iron Losses in Large Salient- Pole Synchronous Hydro-Generators," in *2016 6th International Electric Drives Production Conference (EDPC)*, 2016.

[70] M. Ranlöf, A. Wolfbrandt, J. Lidenholm, and U. Lundin, "Core Loss Prediction in Large Hydropower Generators: Influence of Rotational Fields," *IEEE Transactions on Magnetics*, vol. 45, no. 8, pp. 3200–3206, 2009.

[71] J. C. Akiror, A. Merkhouf, C. Hudon, and P. Pillay, "Consideration of Design and Operation on Rotational Flux Density Distributions in Hydrogenerator Stators," *IEEE Transactions on Energy Conversion*, vol. 30, no. 4, pp. 1585–1594, 2015.

[72] J. C. Akiror, P. Pillay, and A. Merkhouf, "Effect of Saturation on Rotational Flux Distribution in Hydro Generators," *IEEE Transactions on Energy Conversion*, vol. 31, no. 4, pp. 1657 – 1664, 2016.

[73] J. Saitz, "Computation of the core loss in an induction motor using the vector preisach hysteresis model incorporated in finite element analysis," *IEEE Transactions on Magnetics*, vol. 36, no. 4, pp. 769–773, 2000.

[74] E. Dlala, A. Belahcen, K. A. Fonteyn, and M. Belkasim, "Improving loss properties of the Mayergoyz vector hysteresis model," *IEEE Transactions on Magnetics*, vol. 46, no. 3, pp. 918–924, 2010.

[75] E. Dlala, "Efficient algorithms for the inclusion of the Preisach hysteresis model in nonlinear finite-element methods," *IEEE Transactions on Magnetics*, vol. 47, pp. 395–408, 2011.

[76] P. Rasilo, A. Belahcen, and A. Arkkio, "Importance of Iron-Loss Modeling in Simulation of Wound-Field Synchronous Machines," *IEEE Transactions on Magnetics*, vol. 48, no. 9, pp. 2495–2504, 2012.

[77] B. Marcusson and U. Lundin, "Axial Magnetic Fields, Axial Force, and Losses in the Stator Core and Clamping Structure of a Synchronous Generator with Axially Displaced Stator," *Electric Power Components and Systems*, vol. 45, no. 4, pp. 410–419, 2017.

[78] J. Pyrhönen, T. Jokinen, and V. Hrabovcová, *Design of Rotating Electrical Machines*, 2nd ed. John Wiley & Sons, 2014.

[79] G. Traxler-Samek, T. Lugand, and M. Uemori, "Vibrational Forces in Salient Pole Synchronous Machines Considering Tooth Ripple Effects," *IEEE Transactions on Industrial Electronics*, vol. 59, no. 5, pp. 2258–2266, 2012.

[80] M. Valavi, J. Pascal, and A. Nysveen, "Analysis of radial magnetic forces in hydrogenerators with fractional-slot windings," in *2016 XXII International Conference on Electrical Machines (ICEM)*, 2016, pp. 1318–1324.

[81] M. Valavi, A. Nysveen, R. Nilssen, R. D. Lorenz, and T. Rølvåg, "Influence of pole and slot combinations on magnetic forces and vibration in low-speed PM wind generators," *IEEE Transactions on Magnetics*, vol. 50, no. 5, pp. 1–11, 2014.

[82] M. Valavi, "Magnetic Forces and Vibration in Wind Power Generators," Ph.D. dissertation, Norwegian University of Science and Technology, 2015.

[83] H. C. Dirani, S. Cupillard, A. Merkhouf, S. Belanger, A. Tounzi, A. M. Giroux, and K. Al-Haddad, "Free vibration analysis of a large hydroelectric generator and computation of radial electromagnetic exciting forces," in *2015 IEEE International Electric Machines and Drives Conference (IEMDC)*, 2015, pp. 328–334.

[84] H. Karmaker and A. M. Knight, "Investigation and simulation of fields in large salient-pole synchronous machines with skewed stator slots," *IEEE Transactions on Energy Conversion*, vol. 20, no. 3, pp. 604–610, 2005.

[85] K. Sedraoui, K. Al-Haddad, A. Chandra, and C. Millet, "A strategy to reduce the vibrations generated by the harmonics of armature reaction in hydro generators," in *1995 Canadian Conference on Electrical and Computer Engineering*, 1995, pp. 272–276.

[86] O. Kokoko, A. Tounzi, A. Merkhouf, E. Guillot, and K. A. Haddad, "Characterization and validation of a large hydrogenerator under dynamic conditions," *Proceedings - 2016 22nd International Conference on Electrical Machines, ICEM 2016*, pp. 186–192, 2016.

[87] T. Lugand and A. Schwery, "Comparison between the salient-pole synchronous machine and the double-fed induction machine with regards to electromagnetic parasitic forces and stator vibrations," *IEEE Transactions on Industry Applications*, vol. 53, no. 6, pp. 2191–2197, 2017.

[88] J. K. Nøland, "A New Paradigm for Large Brushless Hydrogenerators - Advantages Beyond the Static System," Ph.D. dissertation, Uppsala University, 2017.

[89] J. H. Walker, "Parasitic losses in synchronous-machine damper windings," *Electrical Engineers - Part II: Power Engineering, Journal of the Institution of*, vol. 94, no. 37, pp. 13–25, 1947.

[90] A. Lundseng and I. Vikan, "Generator design for hydropower station upgrade (In Norwegian)," *Master's thesis, Norwegian University of Science and Technology (NTNU)*, 2010.

[91] R. Perers, U. Lundin, and M. Leijon, "Saturation Effects on Unbalanced Magnetic Pull in a Hydroelectric Generator With an Eccentric Rotor," *IEEE Transactions on Magnetics*, vol. 43, no. 10, pp. 3884–3890, 2007.

[92] M. Ranlöf, R. Perers, and U. Lundin, "On Permeance Modeling of Large Hydrogenerators With Application to Voltage Harmonics Prediction," *Energy Conversion, IEEE Transactions on*, vol. 25, no. 4, pp. 1179–1186, 2010.

[93] E. Schmidt, C. Grabner, and G. Traxler-Samek, "Finite element analysis of the 500 MVA hydro-generators at the Bieudron Power Plant," in *2001 5th International Conference on Electrical Machines and Systems (ICEMS)*, 2001, pp. 1072–1076.

[94] B. Taraldsen, "Statorschwingungen in synchronmaschinen mit bruchlochwicklungen (In German)," *Dr. Ing. dissertation, Norwegian Institute of Technology (NTH)*, 1985.

[95] A. Merkhouf and L. Benchaita, "Large hydrogenerator design using advanced tools," in *Second International Conference on Power Electronics, Machines and Drives (PEMD 2004).*, 2004, pp. 398–401.

[96] M. M. Liwschitz, "Distribution Factors and Pitch Factors of the Harmonics of a Fractional-Slot Winding," *Transactions of the American Institute of Electrical Engineers*, vol. 62, no. 10, pp. 664–666, 1943.

[97] J. C. Akiror, A. Merkhouf, P. Pillay, C. Hudon, and C. Millet, "Evaluation of the change in winding pattern of a large hydro generator," in *2016 XXII International Conference on Electrical Machines (ICEM)*, 2016, pp. 325–330.

[98] T. E. Hestengen, "Design Optimization of Hydropower Generators," *Master's thesis, Norwegian University of Science and Technology (NTNU)*, 2016.

[99] GE Renewable Energy, "Medium and Large Hydro Generators, Hydropower Solutions, Date Accessed: September 24, 2018." [Online]. Available: https://www.genewsroom.com/sites/default/files/media/201703/ge-hydro-generator.jpg

[100] E. Westgaard, A. K. Enger, H. J. Mellbye, J. Sonstad, Ø. Torkildsen, and S. Vikanes, *Electrical Equipment : Hydropower Development vol. 13*. Norwegian Institute of Technology (NTH), 1994.

[101] G. Müller, K. Vogt, and B. Ponick, *Berechnung elektrischer Maschinen (In German)*, 6th ed. Wiley-VCH Verlag, 2008.

[102] H. D. Piriz, A. R. Cannatella, E. Guerra, and D. A. Porcari, "Inertia of Hydro Generators . Influence on the Dimensioning , Cost , Efficiency and Performance of the Units," *CIGRÉ, A1-102*, pp. 1–9, 2012.

[103] British Electricity International, *Modern power station practice. Volume C, Turbines, generators and associated plant : incorporating modern power system practice*, 3rd ed. Pergamon Press, 1991.

[104] A. E. Fitzgerald, C. Kingsley, and S. D. Umans, *Electric Machinery (accompanying lecture notes)*, 6th ed. McGraw-Hill, 2003.

[105] E. Westgaard and O. W. Andersen, *Dimensjoneringseksempel for synkronmaskin (In Norwegian)*. Norwegian Institute of Technology (NTH), 1965.

[106] N. Bianchi, S. Bolognani, M. D. Pre, and G. Grezzani, "Design considerations for fractional-slot winding configurations of synchronous machines," *IEEE Transactions on Industry Applications*, vol. 42, no. 4, pp. 997–1006, 2006.

[107] M. Liwschitz-Garik, *Winding alternating-current machines*. Van Nostrand, 1950.

[108] H. Sequenz, *Die Wicklungen elektrischer Maschinen I (In German)*. Springer-Verlag, 1950.

[109] E. Westgaard, *Forelesninger i elektromaskinbygg: Grunnkurs, del I (In Norwegian)*. Norwegian Institute of Technology (NTH), 1955.

[110] F. J. Garcia, M. K. I. Uemori, J. J. R. Echeverria, and E. d. C. Bortoni, "Design Requirements of Generators Applied to Low-Head Hydro Power Plants," *IEEE Transactions on Energy Conversion*, vol. 30, no. 4, pp. 1630–1638, 2015.

[111] R. Richter, *Elektrische Maschinen, Band I (In German)*, 3rd ed. Birkhäuser Verlag Basel, 1967.

[112] J. Juergens, B. Ponick, O. Winter, and A. Fricasse, "Influences of iron loss coefficients estimation on the prediction of iron losses for variable speed motors," in *2015 IEEE International Electric Machines and Drives Conference (IEMDC)*, 2015, pp. 1254–1259.

[113] D. Lin, P. Zhou, W. N. Fu, Z. Badics, and Z. J. Cendes, "A dynamic core loss model for soft ferromagnetic and power ferrite materials in transient finite element analysis," *IEEE Transactions on Magnetics*, vol. 40, no. 2, pp. 1318–1321, 2004.

[114] M. Rosu, J. Saitz, and A. Arkkio, "Hysteresis model for finite-element analysis of permanent-magnet demagnetization in a large synchronous motor under a fault condition," *IEEE Transactions on Magnetics*, vol. 41, no. 6, pp. 2118–2123, 2005.

[115] E. Dlala, J. Saitz, and A. Arkkio, "Hysteresis Modeling Based on Symmetric Minor Loops," *IEEE Transactions on Magnetics*, vol. 41, no. 8, pp. 2343–2348, 2005.

[116] O. Bottauscio, D. Chiarabaglio, M. Chiampi, and M. Repetto, "A Hysteretic Periodic Magnetic Field Solution using Preisach Model and Fixed Point Technique," *IEEE Transactions on Magnetics*, vol. 31, no. 6, pp. 3548–3550, 1995.

[117] J. Saitz, "Magnetic Field Analysis of Electric Machines Taking Ferromagnetic Hysteresis into Account," Ph.D. dissertation, Helsinki University of Technology, 2001.

[118] S. Bi, "Characterization and Modeling of Hysteresis in Ferromagnetic Material," Ph.D. dissertation, Friedrich-Alexander-Universität Erlangen-Nurnberg, 2014.

[119] A. Linker, *Elektromaschinenbau (In German)*, 1st ed. Springer-Verlag, 1925.

[120] W. Li, D. Li, J. Li, and X. Zhang, "Influence of rotor radial ventilation ducts number on temperature distribution of rotor excitation winding and fluid flow state between two poles of a fully air-cooled hydro-generator," *IEEE Transactions on Industrial Electronics*, vol. 64, no. 5, pp. 3767–3775, 2017.

[121] D. Liu, H. Polinder, X. Wang, and J. A. Ferreira, "Evaluating the cost of energy of a 10 MW direct-drive wind turbine with superconducting generators," in *2016 XXII International Conference on Electrical Machines (ICEM)*, 2016, pp. 318–324.

[122] P. Kundur, *Power System Stability and Control*. McGraw-Hill, 1994.

[123] Statnett SF, "Veileder - Funksjonskrav i kraftsystemet 2012 (In Norwegian)," *Norwegian grid codes for transmission system*, 2012.

[124] M. Wallin, M. Ranlöf, and U. Lundin, "Design and construction of a synchronous generator test setup," in *2010 XIX International Conference on Electrical Machines (ICEM)*, 2010, pp. 1–5.

[125] J. Akiror, P. Pillay, and A. Merkhouf, "Challenges in Modeling of Large Synchronous Machines," *IEEE Transactions on Industry Applications*, vol. 54, no. 2, pp. 1652–1662, 2017.

[126] J. Bladh, M. Wallin, L. Saarinen, and U. Lundin, "Standstill Frequency Response Test on a Synchronous Machine Extended With Damper Bar Measurements," *IEEE Transactions on Energy Conversion*, vol. 31, no. 1, pp. 46–56, 2016.

[127] Essex Europe, "Continuously Transposed Cable, Product Information, Date Accessed: April 8, 2019." [Online]. Available: http://www.essexeurope.com/uploadedFiles/EssexEurope/Products/Energy$_{W}ires/CTC$

[128] E. L. Engevik, T. E. Hestengen, M. Valavi, and A. Nysveen, "Effects of lifting reactance requirements on the optimal design of converter-fed synchronous hydrogenerators," in *2017 IEEE International Electric Machines and Drives Conference (IEMDC)*, 2017.

[129] G. Traxler-Samek, R. Zickermann, and A. Schwery, "Cooling Airflow, Losses, and Temperatures in Large Air-Cooled Synchronous Machines," *IEEE Transactions on Industrial Electronics*, vol. 57, no. 1, pp. 172–180, 2010.